JOURNAL OF ADVANCED

APPLIED SCIENCES

E-ISSN: 2979-9759

2024
VOLUME 3
ISSUE 2

WWW.JAASCI.COM

PRENSIP

JOURNAL OF ADVANCED APPLIED SCIENCES

2024 • VOLUME 3 • ISSUE 2

jaasci.com — jadvappsci@gmail.com
prensip.gen.tr — info@prensip.gen.tr

Journal of Advanced Applied Sciences is a peer-reviewed scientific journal published by ***Prensip Publishing*** twice a year.

JOURNAL OF ADVANCED APPLIED SCIENCES

2024 ● VOLUME 3 ● ISSUE 2

TABLE OF CONTENTS

http://jaasci.com
JOURNAL OF ADVANCED APPLIED SCIENCES
e-ISSN: 2979-9759
https://prensip.gen.tr

RESEARCH ARTICLE

Characterization of 3-Chloro-4-Fluoronitrobenzene Molecule with New Calculation Methods and Discussions for Advanced Applied Sciences

Muhammed Oz[1]✉ • Ali Serol Erturk[2] • Umit Erdem[3]

[1]Bolu Abant Izzet Baysal University, Gerede Vocational School, Department of Chemistry and Chemical Processing Technology, Bolu/Türkiye
[2]Adıyaman University, Faculty of Pharmacy, Department of Basic Pharmacy Sciences, Adıyaman/Türkiye
[3]Kırıkkale University, Kırıkkale Vocational School, Department of Electronics and Automation, Kırıkkale/Türkiye

ARTICLE INFO

Article History
Received: 15.11.2024
Accepted: 06.12.2024
First Published: 30.12.2024

Keywords
Comparison
DFT
HF
ICT Regions
Simulations

ABSTRACT

This current research characterizes 2-chloro-1-fluoro-4-nitrobenzene molecule via the Hartree Fock (HF) and density functional theory (DFT) quantum mechanical computational techniques using B3LYP/6-311++G(d,p) levels of computation. The molecular geometries, thermodynamic quantities at 300 K, NMR chemical shifts, corresponding vibrational spectra, UV-vis spectra, vibrational frequencies, and atomic point charge distributions are extensively investigated. The ^{1}H and ^{13}C NMR chemical shifts, and theoretical vibrational frequencies are compared to the experimental results. It is obtained that all calculations are in agreement with the available experimental data which has the ^{1}H isotropic chemical shifts range from 8.306 ppm to 7.235 ppm, while the computed values range from 9.0368 ppm to 6.8397 ppm, 8.3213 ppm to 6.1242 ppm at DFT and HF GIAO levels, respectively. Besides, calculated ^{13}C chemical shifts vary from 141.83 ppm to 186.394 ppm and from 129.743 ppm to 174.373 ppm by using DFT and HF in CH_4, while these values are in the range of 117.00 ppm to 164.59 ppm, experimentally. This points out that the chosen computation sets are highly effective methods for identifying and characterizing the compound. In addition, simulations are performed to examine frontier molecular orbitals, electrostatic potential, and molecular electrostatic potential regions. Key properties such as dipole moment, chemical hardness, transition states, electronegativity, molecular softness, nucleophilic aromatic regions, electrophilicity index, and energy band gap are also analyzed to explore potential future applications such as advanced applied sciences, industry, chemistry, medical, physics, biology, pharmaceuticals, dyes, and agrochemicals of the compound. Additionally, it is noted that the compound contains significant intramolecular charge transfer (ICT) regions, lone electron pairs, electron-donating groups, π-bond conjugation, and particularly reactive electrophilic and nucleophilic aromatic sites. Accordingly, it is pointed out that the molecule has a strong potential for metallic bonding as well as various intermolecular interactions. In summary, this study provides valuable information that will benefit both basic research and technological or industrial applications by increasing the understanding of physical, chemical, structural, and reactive features of the 3-chloro-4-fluoronitrobenzene molecule.

Please cite this paper as follows:

Oz, M., Erturk, A. S., & Erdem, U. (2024). Characterization of 3-chloro-4-fluoronitrobenzene molecule with new calculation methods and discussions for advanced applied sciences. *Journal of Advanced Applied Sciences*, *3*(2), 40-54. https://doi.org/10.61326/jaasci.v3i2.311

1. Introduction

The compound with the molecular formula of $C_6H_3ClFNO_2$, 3-chloro-4-fluoronitrobenzene (sometimes called as 2-chloro-1-fluoro-4-nitrobenzene) possesses a molecular weight of 175.54 g/mol. Especially, with the functional groups including chloro (Cl), nitro (NO_2), the fluoro (F) groups, the title

✉ Correspondence
E-mail address: moz@ibu.edu.tr

compound can find several application fields as a result of the usage of an intermediate in organic synthesis, especially in the production of pharmaceuticals, dyes, and agrochemicals. Besides, the organic compound with distinct functional groups including the valuable combination of a nitro group and two halogens (nitro, fluorine, and chlorine groups) makes the organic material studied reactive in electrophilic and nucleophilic aromatic substitution reactions and thus useful for further functionalization. This compound with a halogenated benzene ring is often used in pharmaceutical research in the case of the requirement of electron-withdrawing effects. The attractive crystal structure (high reactivity) allows selective modification in medicinal chemistry, particularly antimicrobial, anti-inflammatory, and anticancer drugs. Also, chlorine and fluorine contribute to the reactivity of molecules for designing molecules with specific binding affinity and metabolic stability. The presence of halogens (for better bonding to fibers and substrates) and a nitro group (for color stability) gives vibrant colors and improved adhesion. In polymer chemistry, the structure of 2-chloro-1-fluoro-4-nitrobenzene makes it ideal for creating polymers with enhanced thermal stability and resistance to degradation. As a polymer additive, it improves combustion resistance and flame-retardant properties. In agrochemicals, 3-chloro-4-fluoronitrobenzene aids in developing plant protection products due to its strong electron-withdrawing properties and biological activity, making it useful for insecticides, herbicides, and fungicides.

Additionally, due to its reactivity, the 3-chloro-4-fluoronitrobenzene compound has widely been used in organic research environments as a starting material, substrate, or functional group-bearing molecule to explore nucleophilic aromatic substitutions or further functionalization studies. The 3-chloro-4-fluoronitrobenzene molecule is also used to study unique substitutions, reaction mechanisms, or synthetic routes. However, although the 3-chloro-4-fluoronitrobenzene is a very valuable chemical substance in many application fields, it has not found a place in many studies. It is seen that six valuable articles are directly related to the 3-chloro-4-fluoronitrobenzene in the literature. Namely, in a study performed in 2008, the reduction of heterocycles and fluorine-containing nitroaromatics using microwave irradiation power of $Mo(CO)_6$ and DBU in EtOH, the 2-chloro-1-fluoro-4-nitrobenzene, which could play a crucial role in the other compound synthesis of biological molecules, was used as one of the starting materials to get various anilines (Spencer et al., 2008). In a 2024 study, researchers modified oxidized hydrogen-substituted graphyne and combined it with carbon nanotubes (CNTs) using seven ionic liquids through covalent and non-covalent bonding to investigate how ionic liquid structure and CNT incorporation mode impacted material properties, finding that longer alkyl chain ionic liquids had higher adsorption capacities and that CNT incorporation affected the dispersion and interaction with the genotoxic impurity 3-chloro-4-fluoronitrobenzene in gefitinib, demonstrating an economical and simple method for impurity analysis (Zhang et al., 2024). Moreover, Chen and Wang (2021) performed detailed experimental investigations on the density, viscosity, and saturated vapor pressure features for the characterization of the 3-chloro-4-fluoronitrobenzene molecule. In 1997, Ravi et al. conducted experimental studies on the organic synthesis of the 3-chloro-4-fluoronitrobenzene molecule (Ravi et al., 1997). Besides, the molecule was used as a starting material for the production of phenylated diamine, bis(4-amino-2-biphenyl) ether (Morikawa et al., 2005). Moreover, a scientific study has been conducted to investigate changes in the toxicity of chemicals in water as a result of the use of solvents or dispersants as carriers in 2016 (Kikuchi et al., 2016). The research group was used to investigate the bioavailable concentration of the test chemical and whether the compound had a significant or minimal effect on the acute toxicity of the chemical. At the same time, quantum chemistry modeling approaches are powerful tools for predicting the fundamental features of organic molecules and offering deeper insights into experimental phenomena.

In the current study, we perform full identification of the 2-chloro-1-fluoro-4-nitrobenzene molecule with the aid of quantum chemistry models such as HF and DFT within B3LYP and 6-311++G(d,p) computation technique. The theoretical predictions extracted from the modern calculation methods are compared to the experimental observations in the SDBS (10089) database (Ertem & Altunpak, 2019), assessing a strong correlation between theoretical and experimental data for vibrational frequencies deduced from FTIR spectra and NMR spectra. A detailed analysis is conducted on the UV-visible (UV–vis) spectra and a range of thermodynamic properties including heat capacity, total/zero-point vibrational/thermal energy, rotational constants, total dipole moments, and entropy belonging to the 3-chloro-4-fluoronitrobenzene compound. Furthermore, atomic charge distributions are examined to assess dipole moments and regions of intramolecular charge transfer (ICT). The study reveals that the title molecule with the electrophilic and nucleophilic aromatic regions shows potential for metallic bonding and strong intermolecular interactions. It should be referred here that the presence of intramolecular charge transfers enables the compound to be used in the electrode materials (Altunpak et al., 2019; SDBS, 2024). At the same time, this research includes visualization of key electronic properties, such as MEP, LUMO, ESP, and HOMO images providing detail information about electrophilicity, transition states, nucleophilic aromatic regions, chemical hardness, energy band gaps, molecular softness, and electronegativity so that we can understand the high reactivity of the sample studied for the future application fields as regards advanced applied sciences, physics, industry, chemistry, biology, medical, pharmaceuticals, dyes, and agrochemicals of the compound.

2. Materials and Methods

This study provides comprehensive computational analyses including optimized molecular geometry, atomic charges, dipole moment, vibrational frequencies, ICT regions, Raman activities, thermodynamic properties at 300 K, UV-vis spectra, functional group identifications, charge transfer characteristics, NMR chemical shifts utilizing from Gaussian 09 package (Dennington et al., 2007) and molecular visualization program (Becke, 1992; Stephens et al., 1994; Wu & Yang, 2002) at B3LYP method by 6-311++G(d,p) set (Saiardi et al., 1999; Schell et al., 1999) embedded in HF and DFT quantum computational technique of 3-chloro-4-fluoronitrobenzene compound, as shown in Figure 1, for the first time. Electronic properties are analyzed through MEP, LUMO, HOMO, and ESP mappings, while energy band gaps and transition states are evaluated to understand the stability, reactivity, and potential applications of the 2-chloro-1-fluoro-4-nitrobenzene molecule.

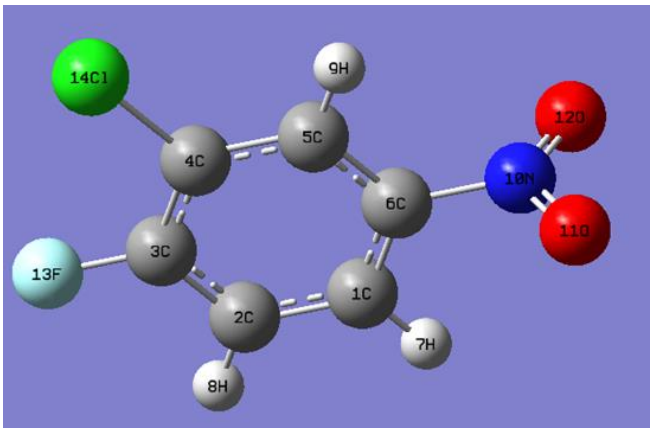

Figure 1. Molecular geometries of 3-chloro-4-fluoronitrobenzene molecule.

This work provides a quality reference on the physical, chemical, structural, and electronic characteristics of the 3-chloro-4-fluoronitrobenzene compound for future studies. Additionally, theoretical NMR shifts are calculated using the B3LYP/6-311++G(d,p) basis level set with the Gauge-Including Atomic Orbital (GIAO) method. Visible electronic absorption maxima are determined using the quantum mechanical methods of TDF/DFT, CIS, and TDF/HF (Furche & Ahlrichs, 2002). Theoretical force constants in Cartesian coordinates are determined under the Cs point group for the optimized geometry. The force field (Pulay et al., 1983; Rauhut & Pulay, 1995) is adjusted through selective scaling within the internal coordinates (Fogarasi & Pulay, 1986; Fogarasi et al., 1992; Keresztury et al., 1993; Polavarapu, 1990).

The electronic features are further analyzed based on total energy calculations and Koopmans' theorem principles. The ionization potential (IP) is calculated by comparing the energy of the radical cation formed by electron loss with that of the neutral molecule and also gives valuable information about the ionization tendency and electronic behavior of the molecule (Buyukuslu et al., 2010). One can see the following relations:

$$IP_{TE} = E_{cation} - E_n \quad (1)$$

$$IP_{KE} = - E_{HOMO} \quad (2)$$

Additionally, EA indicates the electron affinity with the aid of energy differentiation between the anion and neutral molecules:

$$EA_{TE} = E_n - E_{anion} \quad (3)$$

$$EA_{KE} = - E_{LUMO} \quad (4)$$

The IP and EA (electron affinity) are utilized to determine key thermodynamic and physical properties, including electronegativity (χ), softness (ζ), electrophilicity index (ψ), and hardness (η) coefficients (Kohn et al., 1996; Politzer & Abu-Awwad, 1998). Chemical hardness and electronegativity are then found by the corresponding formulas of 5 and 6.

$$\mu \approx - \chi = - (IP+EA)/2 \quad (5)$$

$$\eta \approx (IP-EA)/2 \quad (6)$$

Moreover, the softness and electrophilicity indices are determined by using 7 and 8. Namely,

$$\zeta = 1/(2\eta) \quad (7)$$

$$\psi = (\mu 2/2\eta) \quad (8)$$

3. Results

In this work, we are interested in the vibrational frequencies, related assignments of vibrations, optimized molecular structures, atomic charge distributions, dipole moments, ICT regions, thermodynamic properties (rotational constants, entropy, heat capacity, and scaled zero-point vibrational/thermal/total energies) at 300 K, UV-vis absorption maxima, functional group identifications, electrophilic/nucleophilic aromatic regions, charge transfer characteristics, lone (non-bonding) pairs, chemical hardness, energy band gap, molecular softness, and electronegativity NMR chemical shifts, conjugation of π bonds, electron engagement, 2D total charge contours, MEP, LUMO, ESP, and HOMO images of 3-chloro-4-fluoronitrobenzene compound for the first time.

The illustration of 3-chloro-4-fluoronitrobenzene molecule is depicted in Figure 1. The related geometric parameters including bond length sizes and bond angles of 3-chloro-4-fluoronitrobenzene molecule performed by both DFT and HF computation levels of theory are given in Table 1. Prior to the crucial discussions, Table 1 strongly indicates that all the bond lengths and both angles are found to be in perfect agreement with each other. That is exactly why the modern calculation methods preferred in the current work are reliable. In detail, two models show that there are no distortions and deviations in the bond length sizes and bond angles on the benzene ring. The

carbon and carbon bond lengths are calculated as 1.4014 Å and the lengths for C-H bonds are calculated to be 1.07 Å at both calculation methods. Similarly, the C-F bond length sizes are calculated to be 1.35 Å when the length between the nitrogen and carbon atoms is obtained to be 1.47 Å. Besides, the bond length size between nitrogen and oxygen atoms is computed to be 1.35 Å. Likewise, the bond angles are not distorted. On this basis, the bond angles between carbons is computed as 1200. Moreover, the bond angle between carbon-carbon-fluorine, or chlorine atoms and carbon-carbon-hydrogen atoms is calculated to be 1200. Also, the bong angle between carbons and nitrogen atoms is found to be 109.39690. Further, the angle for carbon-nitrogen-oxygen atoms is determined to be 109.39690. Additionally, the bond angle between oxygen-nitrogen-oxygen atoms is obtained as 106.54840 (Table 1). The perfect harmony between the calculated structural geometry parameters shows us that the DFT and HF quantum mechanical methods can be used to determine all other features. Shortly, the title 3-chloro-4-fluoronitrobenzene molecule with distinct functional groups has an ideal geometry for electrophilic and nucleophilic interactions.

The studied molecule (C_s point group) possesses 14 atoms, hence, there appears an identity and a reflection plane symmetry element. There are 3N internal vibrational modes (Wilson et al., 1980) resulting from the three Cartesian displacements. Among them, six modes account for translational and rotational movements. Therefore, the remaining 36 (3N-6) modes are characterized as 22 A' and 14 A" modes. In the Raman spectra, the A' modes, representing symmetric (in-plane) vibrations, are polarized, while the A" modes, which correspond to anti-symmetric (out-of-plane) vibrations, are depolarized (Krishnakumar et al., 2008). The spectroscopic features of the 3-chloro-4-fluoronitrobenzene molecule are extensively examined through frequency calculation analysis. Detailed vibrational assignments for the fundamental modes are provided in Table 2, offering insights into their structural and spectroscopic behaviors.

The presence of aromatic rings can be readily identified through the characteristic vibrations related to the C–C and C–H rings. The stretching vibrations of C–H bonds occur above 3000 cm^{-1} and typically appear as a series of weak to moderate bands, in contrast to the aliphatic C–H stretching modes (Coates, 2006). In the current work, the stretching frequencies are calculated between 3195 cm^{-1} and 3220 cm^{-1} and 3217 cm^{-1} and 3251 cm^{-1} at DFT and HF calculation basis sets, respectively. The experimental findings are determined to vary between 3427 cm^{-1} and 2925 cm^{-1} under different solvents. As for the benzene ring vibrations, the C=C stretching modes are calculated to be about 1504 cm^{-1} and 1586 cm^{-1} using the quantum mechanical calculation methods.

Table 1. Theoretical geometric (bond lengths and angles) parameters of the 3-chloro-4-fluoronitrobenzene molecule.

Bond Length (Å)			Bond Angles (°)		
Elements	**DFT/B3LYP//6-311++G(d,p)**	**HF/6-311++G(d,p)**	**Elements**	**DFT/B3LYP//6-311++G(d,p)**	**HF/6-311++G(d,p)**
C1-C2	1.40	1.40	C2-C1-C6	120.0	120.0
C1-C6	1.40	1.40	C2-C1-H7	120.0	120.0
C1-H7	1.07	1.07	C6-C1-H7	120.0	120.0
C2-C3	1.40	1.40	C1-C2-C3	120.0	120.0
C2-H8	1.07	1.07	C1-C2-H8	120.0	120.0
C3-C4	1.40	1.40	C3-C2-H8	120.0	120.0
C3-F13	1.35	1.35	C2-C3-C4	120.0	120.0
C4-C5	1.40	1.40	C2-C3-F13	120.0	120.0
C4-Cl14	1.76	1.76	C4-C3-F13	120.0	120.0
C5-C6	1.40	1.40	C3-C4-Cl14	120.0	120.0
C5-H9	1.07	1.07	C5-C4-Cl14	120.0	120.0
C6-N10	1.47	1.47	C1-C6-N10	109.4	109.4
N10-O11	1.36	1.36	C6-N10-O12	109.4	109.4
N10-O12	1.36	1.36	O11-N10-O12	106.55	106.55

The stretching vibrational modes of N=O bonds are experimentally measured to be about 1674-1669 cm^{-1}. Similarly, these modes appear at 1642-1366 cm^{-1} and 1752-1476 cm^{-1} at DFT and HF levels of calculation, respectively. Moreover, the stretching modes for the fluorine and chlorine atoms are calculated as 1248-722 cm^{-1} at the calculation levels. Experimentally, the stretching mode of F-C bonding is measured to be about 1171 and 722 cm^{-1}. The other skeleton modes are found to be in a range of 46-1617 cm^{-1} at DFT/B3LYP//6-311++G(d,p) basis set and 45-1699 cm^{-1} HF/6-311++G(d,p) calculation levels. One can see similar results in the scientific studies (Baraistka et al., 1987; Rintoul et al., 2008; Wojtkowiak & Chabanel, 1977).

Table 2. Experimental and theoretical vibrational frequencies (cm^{-1}) for the 2-chloro-1-fluoro-4-nitrobenzene molecule.

Assignments	**Scaled Freq. (cm^{-1}) *DFT***	**Scaled Freq. (cm^{-1}) *HF***	**IR Intent *DFT***	**IR Intent *HF***	**Exp. Freq. (Liquid Film)**	**Exp. Freq. (KBr Disc)**	**Exp. Freq. (nujol mull)**
$\upsilon_{sym(C-H)}$	3220.10	3251.59	11.35	10.93	3427	3411	2976
$\upsilon_{sym(C-H)}$	3219.96	3248.80	6.59	5.49	2983		2951
$\upsilon_{asym(C-H)}$	3195.11	3217.75	0.03	0.12	2946	2949	2925
$\upsilon_{a+}\ \upsilon_{(O=N)}$	1642.26	1751.54	29.36	390.29	1894	1757	1674
$\upsilon_{a+}\ \gamma_{(C-H)+}\ \upsilon_{(O=N)}$	1617.32	1699.31	50.90	90.43	1835	1655	1669
$\upsilon_{(O=N)+}\ \upsilon_{a+}\ \gamma_{(C-H)}$	1580.87	1682.23	253.37	194.21	1655		
$\gamma_{(C-H)}+\upsilon_{(C=C)+}\ \upsilon_{(C3-F13)+}\ \upsilon_{(C6-N10)}$	1504.40	1586.08	125.38	37.34	1649		
$\upsilon_{a+}\ \gamma_{(C-H)}$	1423.22	1547.02	3.03	463.68	1468	1468	1464
$\upsilon_{(O=N)+}\ \gamma_{(C-H)+}\ \upsilon_{(C6-\ N10)}$	1365.50	1476.02	313.04	8.01	1379	1380	
$\upsilon_{asym}\ a_{+}\ \gamma_{(C-H)}$	1339.56	1340.12	22.67	99.64	1370	1370	1373
$B_{a+}\ \gamma_{(C-H)+}\ \upsilon_{(\ F-C)}$	1274.69	1307.72	123.35	4.15			
$B_{a+}\ \gamma_{(C-H)}$	1251.40	1226.84	17.21	18.32			1249
$\gamma_{(C-H)+}\ \upsilon_{(\ F-C)+}\ \upsilon_{(C6-N10)}$	1141.67	1192.73	37.37	16.96	1167	1168	1171
$B_{a+}\ \gamma_{(C-H)+}\ \upsilon_{(C6-N10)+}\ \upsilon_{(\ F-C)}$	1126.18	1150.14	46.08	5.17	1150	1140	1126
$\upsilon_{a+}\ \gamma_{(C-H)}$	1063.36	1108.71	27.16	3.15	1112	1111	1112
$\phi_{(C-H)}$	971.87	1043.68	0.02	0.45	1004	1006	1009
$o_{(C-H)}$	914.76	989.19	24.63	20.65	950	950	978
$B_{a+}\ \upsilon_{(C6-N10)+}\ \gamma_{(C-H)}+\ \upsilon_{(\ F-C)}$	907.91	960.17	37.65	33.25			
$\upsilon_{(C-H)}$	842.77	900.89	25.98	34.00	864	885	847
$\phi_{molecule}$	822.76	865.88	4.70	8.05	830	831	832
$\gamma_{(C-C-C)+}\ \upsilon_{(\ F-C)+}\ \gamma_{(O-N-O)}$	722.38	777.501	55.70	33.78			722
$\phi_{molecule}$	720.85	751.29	19.25	70.77			
$o_{molecule}$	695.56	742.33	0.40	0.14	671	672	
$\gamma_{(C-C-C)+}\ \gamma_{(C-C-N)}$	641.75	666.64	13.30	20.18		611	640
$\gamma_{(C-C-N)+}\ \gamma_{(C-C-F)+}\ \gamma_{(C-C-Cl)}$	557.32	579.31	1.19	1.44	556	558	
$o_{molecule}$	531.63	549.66	0.72	1.58			
$\gamma_{(C-C-F)+}\ \gamma_{(C-C-O)+}\ \gamma_{(C-C-Cl)}$	500.75	521.16	6.6	8.38	505		518
$o_{ring+}\ \gamma_{(C-C-Cl)}+\ \gamma_{(C-C-F)}$	450.13	475.36	3.57	4.47	441		
$\gamma_{(C-C-C)+}\ \gamma_{(C-C-N)+}\ \gamma_{(C-C-F)}$	367.42	380.39	0.11	0.01			
$\gamma_{(C-C-C)+}\ \gamma_{(C-C-H)+}\ \upsilon_{(C-NO2)}$	349.42	365.98	0.29	0.40			
$o_{molecule}$	327.80	347.75	0.24	0.29			
$\gamma_{(C-C-Cl)+}\ \gamma_{(C-C-F)+}\ \gamma_{(C-C-N)}$	250.82	263.05	2.11	3.25			
$\gamma_{(C-C-F)+}\ \gamma_{(C-C-N)+}\ \gamma_{(C-C-C)}$	175.54	183.43	1.66	2.32			
$\upsilon_{molecule}$	169.16	178.94	0.02	0.07			
$\upsilon_{molecule}$	114.31	122.97	4.75	5.92			
$\Psi_{NO2}+w_{ring}$	45.91	44.62	0.06	0.08			

Abbreviations used: **γ**. bending; **w**. wagging; **υ.** stretching; **sym**. symmetric; **B**. breathing; **υ**. rocking; **Ψ**. torsion; **asy**. asymmetric; **Φ**. Twisting, **o**: out of bending, and **a** – Ring.

4. Discussion

In this study, atomic point charge distributions across the title 2-chloro-1-fluoro-4-nitrobenzene molecule are analyzed using the Mulliken population analysis method (Foresman & Frish, 1996; Helgaker et al., 1986; Olsen & Jørgensen, 1985) based on the quantum mechanical calculation method. For the level of calculations, both DFT and HF levels are used, and one can see atomic charges for each atom in Table 3. It is observed that the results obtained from both quantum computational methods are found to be in good agreement with each other. As for Mulliken carbon atomic charges, it is seen that the parameters are found to be both positive and negative. In this respect, the C4 atom possesses the maximum Mulliken value of 0.818936 a.u. at the DFT and 1.094944 a.u. at HF calculation levels due to its place closer to the ICT regions and lone pairs whereas the minimum value of -1.283815 a.u. and -1.246466 a.u. is computed at the B3LYP and HF levels of theory, respectively, for the C6 atom on the molecule. The Mulliken atomic point charge distributions for the nitrogen atom for the molecule are noted to be negative. That is -0.140476 a.u. and -0.067920 a.u. at the B3LYP and HF levels of theory, respectively. It can be attributed to a result of the intrinsic high electronegativity of the nitrogen atom. As for the distinct functional groups including halogens, the atomic charge of fluorine atoms is computed to be about -1.283815 a.u. and -1.246466 a.u.

The negatively charged lone pair verifies that charge is transferred from the carbon atom to the fluorine one. Thus, the fluorine atom behaves as the electron-withdrawing part of the molecule. In other words, this atom augments the functionalization and reactivity of the studied molecule so that the compound can be used for designing molecules with specific binding affinity and metabolic stability. Conversely, chlorine atoms lose electrons due to the position and charge transfer from carbon to chlorine atoms. Accordingly, the computationl methods calculate the high positive Mulliken values. Namely, the atomic charge for the chlorine on the molecule is calculated to be about 0.383411 and 0.286061 a.u. at the B3LYP and HF levels of theory. At the same time, both the oxygen atoms are calculated in negative values due to the acceptance of electrons (electron-withdrawing) along the molecule. Numerically, the DFT method calculates the values of -0.009972 a.u. for the O11 atom and -0.007071 a.u. for the O12 atom while the atoms are determined as -0.059361 a.u. and -0.062761 a.u. at HF modern computation method. As expected, all the hydrogen atoms lose the electron on the molecule. The highest Mulliken hydrogen atomic charge is determined to be about 0.282926 a.u. and 0.335952 a.u. for the H9 atom due to high negative charges around the atom and high electron engagement. All in all, the charge migrations are related to molecular interactions across the title compound. The presence of ICT regions, lone pairs, electron-donating groups, π-bond conjugation, and especially electrophilic/nucleophilic aromatic regions based on the functional groups leads to the different distributions of atomic point charges across the compound studied. That is exactly why the material can be used in many advanced applied sciences. The variations between HF and B3LYP results can be attributed to factors such as π-conjugation within the carbon ring, the presence of non-bonding lone pairs, electron engagement, and ICT effects; nonetheless, the results remain largely consistent.

Table 3. Atomic point charge distributions across the 2-chloro-1-fluoro-4-nitrobenzene molecule.

Label	DFT/B3LYP//6-311++G(d,p)	HF/6-311++G(d,p)
C1	0.556907	0.433912
C2	-0.211351	-0.139069
C3	-0.889484	-1.059805
C4	0.818936	1.094944
C5	0.136082	0.070027
C6	-1.283815	-1.246466
H7	0.272392	0.317739
H8	0.223312	0.268211
H9	0.282926	0.335952
N10	-0.140476	-0.067920
O11	-0.009972	-0.059361
O12	-0.007071	-0.062761
F13	-0.131795	-0.171466
Cl14	0.383411	0.286061

Electronic transitions in the 2-chloro-1-fluoro-4-nitrobenzene molecule are classified by the orbitals involved and specific regions within the molecule. The two primary transitions observed are $\pi \rightarrow \pi^*$ (donor to acceptor), generally stronger, on the other hand, the transition of $n \rightarrow \pi^*$ is relatively weaker. To characterize the transitions, electronic absorption spectra are calculated using CIS, TD-DFT/B3LYP//6-3116+G(d,p), and TD-HF/6-311++G(d,p) levels of calculation in vacuum. In the computational approaches provided, there are some values for absorption maxima (λ), excitation energies, CI-expansion coefficients, oscillator strengths (f), singlet states, and main transition details, summarized in Table 4. It appears that all the calculation methods exhibit similar results for all the values. In the table, the λ parameter corresponds to electron availability, and key electronic transitions take places between frontier molecular orbitals. For excited state 1, transitions stem from HOMO-2 to LUMO, or HOMO-1→LUMO+14 or HOMO-2→LUMO+3 are identified, while additional transitions are detailed in Table 4.

Numerically, the calculated maximum absorption wavelengths (λ_{max}) are approximately 867.97 nm, 1665.41 nm, and 1226.17 nm for excited state 1 at the standard CIS, TD-DFT/B3LYP//6-311++G(d,p), and TD-HF/6-311++G(d,p) levels of calculation, respectively. For excited state 2, λ_{max}

parameters are found to be 482.25 nm, 756.14 nm, and 555.33 nm within the same calculation methods. Besides, for excited state 3, the λ_{max} values are calculated to be about 374.32 nm, 607.34 nm, and 497.25 nm at the calculation levels of CIS, TD-DFT/B3LYP//6-3116+G(d,p), and TD-HF/6-311++G(d,p), respectively. 867.97 nm (1665.41 nm and 1226.17 nm) transition correspond to a $\pi \rightarrow \pi^*$ transition associated with C=C bonds, while 482.25 nm (756.14 nm and 555.33 nm) peak involves overlapping $\pi \rightarrow \pi^*$ transitions within the benzene ring, influenced by oscillation effects (Table 5).

Table 4. Theoretical electronic absorption spectra parameters inferred from CIS basis set.

CI-Expansion Coefficient					
Excitations	**Energy (eV)**	**Singlet-A**	**Wavelength (nm)**	**Oscillator strength (f)**	**Translations**
Excited State 1					
39→45		-0.41940			HOMO-2→LUMO
40→45		0.47988			HOMO-2→LUMO+1
42→45	1.4284	-0.18942	867.97	0.0004	HOMO-2→LUMO+14
43→45		0.12941			HOMO-1→LUMO
44→45		-0.12089			HOMO-1→LUMO+14
Excited State 2					
37→45		0.10163	482.25		HOMO-2→LUMO
38→45	2.5710	0.12234		0.0018	HOMO-2→LUMO+1
41→45		-0.13039			HOMO-2→LUMO+3
Excited State 3					
30→45		-0.13024			HOMO-2→LUMO
36→45		-0.19514			HOMO-2→LUMO+1
42→45	3.0417	-0.18573	374.32	0.0491	HOMO-2→LUMO+3
43→45		-0.10329			HOMO-2→LUMO+14
44→45		0.21455			HOMO-1→LUMO

Table 5. Theoretical electronic absorption spectra parameters deduced from TD-DFT/B3LYP//6-3116+G(d,p), and TD-HF/6-311++G(d,p) calculation levels.

TD-DFT/B3LYP//6-3116+G(d,p)					
Excitations	**Energy (eV)**	**Singlet-A**	**Wavelength (nm)**	**Oscillator strength (f)**	**Translations**
Excited State 1					
41→45		0.11875			HOMO-3-LUMO
42→45	0.7445	-0.28750	1665.41	0.0000	HOMO-2→LUMO
43→45		-0.39962			HOMO-1→LUMO
44→45		0.50663			HOMO→LUMO
Excited State 2					
41→45		-0.11746	756.14		HOMO-3→LUMO
42→45	1.6397	0.22109		0.0006	HOMO-2→LUMO
43→45		0.43544			HOMO-1→LUMO
44→45		0.49338			HOMO→LUMO
Excited State 3					
41→45		-0.14123			HOMO-3→LUMO
42→45	2.0414	0.56931	607.34	0.0005	HOMO-2→LUMO
43→45		-0.38833			HOMO-1→LUMO
TD-HF/6-311++G(d,p)					

Table 5. (continued).

Excitations	Energy (eV)	Singlet-A	Wavelength (nm)	Oscillator strength (f)	Translations
Excited State 1					
39→45	1.0111	-0.43665	1226.17	0.0003	HOMO-5→LUMO
40→45		0.48435			HOMO-4→LUMO
42→45		-0.24334			HOMO-2→LUMO
43→45		0.10265			HOMO-1→LUMO
Excited State 2					
37→45	2.2326	0.15665	555.33	0.0015	HOMO-7→LUMO
38→45		0.66205			HOMO-6→LUMO
41→45		-0.11241			HOMO-3→LUMO
Excited State 3					
42→45	2.4934	0.50585	497.25	0.0403	HOMO-2→LUMO
43→45		0.22326			HOMO-3→LUMO
44→45		-0.36931			HOMO→LUMO

A weak absorption peak of 374.32 nm (607.34 nm and 497.25 nm) corresponds to an n → π* transition involving NO_2 and related halogen groups. In the CIS calculation method, oscillator strengths of 0.0004, 0.0018, and 0.0491 for these transitions are also shown in Table 4. The higher oscillator strength is observed for the weak absorption peak.

In the current work, we make NMR analyses for ^{13}C and ^{1}H NMR spectra to identify the sample using the experimental and theoretical data using HF and B3LYP modern calculation techniques as a result of the perfect agreement between all the data discussed above. It is received that the latter calculation methods show much closer results due to electron correlation effects along the calculations. Even, B3LYP calculations for the vibrational spectra in the optimized molecular structure of the molecule have already displayed a strong correlation with experimental data. In this study, the GIAO method for two quantum mechanical calculations is employed to calculate the ^{13}C and ^{1}H NMR chemical shifts for the 3-chloro-4-fluoronitrobenzene molecule. One can see every calculation in Table 6. Experimentally, ^{1}H isotropic chemical shifts range from 8.306 ppm to 7.235 ppm, while the computed values range from 9.0368 ppm to 6.8397 ppm, 8.3213 ppm to 6.1242 ppm at DFT (B3LYP/6-311++(d,p))//TMS+HF/6-31G(d) GIAO and B3LYP/6-311++(d,p))//TMS+B3LYP/6-311+G(2d,p) GIAO levels of theory. The highest/smallest ^{1}H chemical shift is observed for the H9/H7 atom. It is normal to possess the maximum NMR chemical shift of the H_9 atom because of the highly electronegative atoms around the atom (the presence of ICT regions, lone pairs, and electron-donating groups).

Table 6. ^{13}C and ^{1}H isotropic chemical shifts (concerning TMS, all values in ppm).

	DFT(B3LYP/6-311++(d,p))//			HF(6-311++(d,p))//			Experimental
Label	**TMS HF/6-31G(d) GIAO**	**TMS B3LYP/6-311+G(2d,p) GIAO**	**CH4 HF/6-31G(d) GIAO**	**TMS HF/6-31G(d) GIAO**	**TMS B3LYP/6-311+G(2d,p) GIAO**	**CH4 HF/6-31G(d) GIAO**	**$CDCl_3$**
C_3	187.28	169.76	186.394	175.259	157.739	174.373	164.59
C_1	184.585	167.066	183.700	161.730	144.21	160.844	159.40
C_4	158.218	140.699	157.333	141.082	123.563	140.197	144.42
C_6	157.138	140.218	156.852	178.288	160.769	177.403	126.78
C_5	146.042	128.522	145.157	142.526	125.006	141.641	124.18-122.46
C_2	142.715	125.195	141.83	130.628	113.108	129.743	117.47-117.00
H_9	9.0368	8.3213		9.4301	8.7146		8.306
H_8	7.5097	6.7942		7.626	6.9105		7.424
H_7	6.8397	6.1242		5.898	5.1825		7.235

As for the HF quantum mechanical method results, ^{1}H chemical shifts are found to be in a range of 9.4301 ppm to 5.898 ppm, 8.7146 ppm to 5.1825 ppm at HF (6-311++(d,p))/TMS+HF/6-31G(d) GIAO) and 6-311++(d,p))//TMS+B3LYP/6-311+G(2d,p) GIAO) calculation levels. In this respect, theoretical predictions (especially DFT

ones) observed from all the used methods demonstrate close agreement between experimental findings. For ^{13}C NMR shifts relative to TMS, computed values span 142.715 ppm (C2) to 187.28 ppm (C3) at DFT (B3LYP/6-311++(d,p))//TMS+HF/6-31G(d) GIAO), 125.195 ppm to 169.760 ppm using B3LYP/6-311++(d,p))//TMS+B3LYP/6-311+G(2d,p) GIAO) levels of theory, compared to experimental shifts of 117.00 ppm to 164.59 ppm. Additionally, the chemical shifts for the carbon atoms are found to change from 130.628 ppm (C2) to 175.259 ppm (C3), 157.739 ppm to 113.108 ppm at HF (6-311++(d,p))/TMS+HF/6-31G(d) GIAO) and 6-311++(d,p))/TMS+B3LYP/6-311+G(2d,p) GIAO) calculation levels, respectively. Besides, ^{13}C chemical shifts are calculated to vary from 141.83 ppm until 186.394 ppm and from 129.743 ppm to 174.373 ppm by using DFT (B3LYP/6-311++(d,p))//CH4 HF/6-31G(d) GIAO) and HF (6-311++(d,p))//CH4 HF/6-31G(d) GIAO) modern calculation methods. According to the theoretical calculations, it is observed that the DFT method calculates higher values than those of HF calculation level. In general, similar to other sections, it is stated that the DFT theoretical calculation method (especially DFT (B3LYP/6-311++(d,p))//TMS+HF/6-31G(d) GIAO)) offers the closest chemical shifts among the methods.

In the present study, thermodynamic properties including thermal energies, total, zero-point vibrational energy, heat capacities, rotational constants, entropies, and dipole moments (μ, μ_x, μ_y, μ_z, and μ) are computed using B3LYP and HF computational techniques. The calculated results are summarized in Table 7. It is seen that the zero-point vibrational energy (scaled by a valuable factor based on overestimation of harmonic vibrational frequencies (Avci & Atalay, 2009) is calculated to be about 52.078759764 a.u./Particle and 51.2612766 a.u./Particle at the DFT and the HF levels of theory. As for the total energy parameter, it is calculated as approximately -995.75777428 a.u. by the DFT quantum mechanical method, while the total energy is determined as -992.07996302 a.u. by the HF modern calculation method. At the same time, total entropy values are approximately 95.275 $cal.mol^{-1}K^{-1}$ and 93.003 $cal.mol^{-1}K^{-1}$ at the B3LYP and HF levels, respectively. The thermal energy values are found to be 58.709 $kcal.mol^{-1}$ (B3LYP) and 62.827 $kcal.mol^{-1}$ (HF). Similarly, the total heat capacity values are determined to be approximately 32.620 $cal.mol^{-1}K^{-1}$ and 30.311 $cal.mol^{-1}K^{-1}$ at the B3LYP and HF calculation levels. The rotational constant values are calculated as 1.84572 GHz, 0.60797 GHz, and 0.45733 GHz at the DFT/B3LYP//6-311++G(d,p) level of theory, while the values are defined to be about 1.88353 GHz, 0.62104 GHz, and 0.46705 GHz at the HF/B3LYP//6-311++G(d,p) basis set.

The dipole moment, reflecting the uneven charge distribution across a molecule, plays a crucial role in analyzing intermolecular interactions, such as van der Waals forces, where higher dipole moments often correspond to stronger interactions. This parameter also provides insights into the formation of herbicides and insecticides and related biological properties of the molecule, particularly regarding interactions with enzyme active sites, and its behavior in a magnetic field. The computed dipole moment values for the 2-chloro-1-fluoro-4-nitrobenzene molecule are approximately 2.8412 Debye at DFT/B3LYP//6-311++G(d,p) basis set and 2.9382 Debye at HF/6-311++G(d,p) (HF), indicating a polar structure with non-uniform atomic charge distributions, consistent with simulation analyses.

Besides, the compound with the combination of great stability/bioactivity and high dipole moment seems to be useful for the functionalization of the newly synthesized molecules to develop fungicides. Extensive studies have examined how external magnetic fields influence properties such as in vitro regeneration, phenolic content, growth, antioxidant activity, and defense enzyme responses in organic compounds (Ulgen et al., 2020, 2021).

Table 7. Total energies (a.u.), Zero-point correction (a.u./Particle), zero-point vibrational energies (kcal mol^{-1}), entropies (cal $mol^{-1}K^{-1}$), thermal energies (kcal mol^{-1}), rotational constants (GHz), heat capacities (cal $mol^{-1}K^{-1}$), and dipole moment (Debye), and Zero-point corrections (a.u./Particle).

Parameters	DFT/B3LYP//6-311++(d,p)	HF/6-311++(d,p)
Zero-point vibrational energy	52.078759764	51.2612766
Zero-point correction	0.084652	0.091787
Thermal correction to Energy	0.093559	0.100121
Thermal correction to Enthalpy	0.094503	0.101066
Thermal correction to Gibbs Free Energy	0.049235	0.056877
Sum of electronic and zero-point Energies	-995.673122	-991.988176
Sum of electronic and thermal Energies	-995.664215	-991.979842
Sum of electronic and thermal Enthalpies	-995.663271	-991.978897
Sum of electronic and thermal Free Energies	-995.708539	-992.023086
Total energy	-995.75777428	-992.07996302

Table 7. (continued).

Parameters	DFT/B3LYP//6-311++(d,p)	HF/6-311++(d,p)
Rotational constant	1.84572	1.88353
	0.60797	0.62104
	0.45733	0.46705
Entropy		
Total	95.275	93.003
Translational	41.386	41.386
Rotational	30.816	30.754
Vibrational	23.072	20.863
Heat capacity		
Total	32.620	30.311
Translational	2.981	2.981
Rotational	2.981	2.981
Vibrational	26.659	24.350
Thermal energy		
Total	58.709	62.827
Translational	0.889	0.889
Rotational	0.889	0.889
Vibrational	56.932	61.050
Dipole moment		
μ_x	-2.0792	-2.0014
μ_y	1.9363	2.1511
μ_z	0.0000	0.0000
μ	2.8412	2.9382

This section examines the basic properties of frontier molecular orbitals, namely HOMO and LUMO. The HOMO is considered the outermost orbital that contains electrons and acts as an electron donor, while the LUMO is the innermost orbital that has vacancies that can accept electrons (Gece, 2008). Orbitals are crucial to understanding the chemical reactivity and electronic properties of organic molecules. According to molecular orbital theory, interactions between HOMO and LUMO involve electronic transitions such as π-π^* transitions, which directly affect the optical and electronic behavior of a molecule (Fukui, 1982).

The HOMO level is related to the ionization potential, which reflects the tendency of the molecule to donate electrons, whereas the LUMO energy level corresponds to the electron affinity, which represents the capacity of the molecule to accept electrons. The energy gap (ΔE) between HOMO and LUMO, also known as the band gap, is a critical measure of molecular stability, where a smaller gap indicates greater chemical reactivity and a larger gap indicates greater stability (Lewis et al., 1994). Our calculated values for the frontier orbitals and band gap are presented in Table 8, and 3D visualizations of HOMO and LUMO are shown in Figure 2.

The calculated band gap at B3LYP/6-311++G(d,p) modern calculation level is approximately 0.17286 a.u. while at HF/6-311++G(d,p) basis level it is approximately 0.41342 a.u. The larger HF band gap calculated is due to the nonexistence of electron correlation across the HF quantum mechanical method. In the simulations, HOMO is mainly localized in various regions of the molecule, excluding hydrogen (positively charged), nitrogen, (rarely) oxygen, and an amino group, such as H_7, H_8, and amino group, whereas LUMO extends to larger areas of the molecule, excluding atoms such as chlorine and hydrogen atoms.

Table 8. Energy gaps, total electronic energies, and molecular quantities determined from DFT/B3LYP//6-311++G(d,p) and the HF/6-311++G(d,p) levels of theory.

Molecular orbital features	**DFT/B3LYP//6-311++G(d,p)**	**HF/6-311++G(d,p)**
E_{HOMO} (a.u.)	-0.29148	-0.38077
E_{LUMO} (a.u.)	-0.11862	0.03265
$E_{HIGHEST}$ (a.u.)	215.75794	219.34911
E_{LOWEST} (a.u.)	-101.58774	-104.86940
Energy bandgap, ΔE (E_{HOMO}-E_{LUMO}) (a.u.) bandgAD, AE EHOMO-ELUMO (8.u.)	0.17286	0.41342
Ionization potential (IP=-E_{HOMO})	0.29148	0.38077
Electron affinity (EA=-E_{LUMO})	0.11862	-0.03265
Chemical hardness (η)	0.08643	0.20671
Chemical softness (ζ)	5.1790586	2.418847
Electronegativity (χ)	0.20505	0.174706
Chemical potential (μ)	-0.20505	-0.174706
Electrophilicity index (ψ)	0.243234	0.0738285
Maximum charge transfer index ($\Delta N_{max.}$=- μ/ η)	2.37244	0.84517439

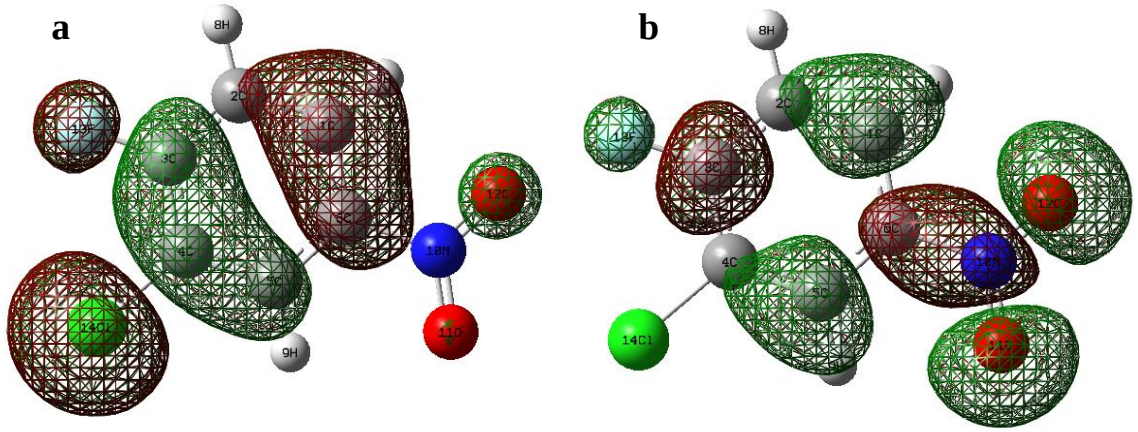

Figure 2. a-) HOMO simulation and b-) LUMO map of the title compound. (Red/green regions reveal the positive/negative phases.

The lowest molecular orbital (MO) eigenvalue for the compound is determined to be -101.58774 a.u. at the B3LYP modern calculation level and -104.86940 a.u at the HF calculation level, while the highest MO eigenvalues are computed as 215.75794 a.u. and 219.34911 a.u. for B3LYPand HF, respectively. These results offer a comprehensive defining of the electronic structure of the 2-chloro-1-fluoro-4-nitrobenzene molecule, demonstrating how stability and reactivity vary with the computational method employed. Furthermore, essential electronic properties such as EA, IP, dipole moment (μ), softness (ζ), electronegativity (χ), electrophilicity (ψ), hardness (η), and ΔN_{max} are evaluated through advanced computational chemistry techniques.

This section focuses on the ESP surface map of the title 2-chloro-1-fluoro-4-nitrobenzene compound, providing a detailed view of its molecular size, shape, and charge distribution in its chemical environment. ESP mapping serves as a critical tool for analyzing molecular interactions as it reveals potential reactivity sites and highlights suitable sites for intermolecular and intramolecular interactions such as hydrogen bonding; ESP mapping is consistent with the previously discussed findings on electron density, non-bonding lone pairs, electron engagement, and conjugative effects (Wang et al., 2008).

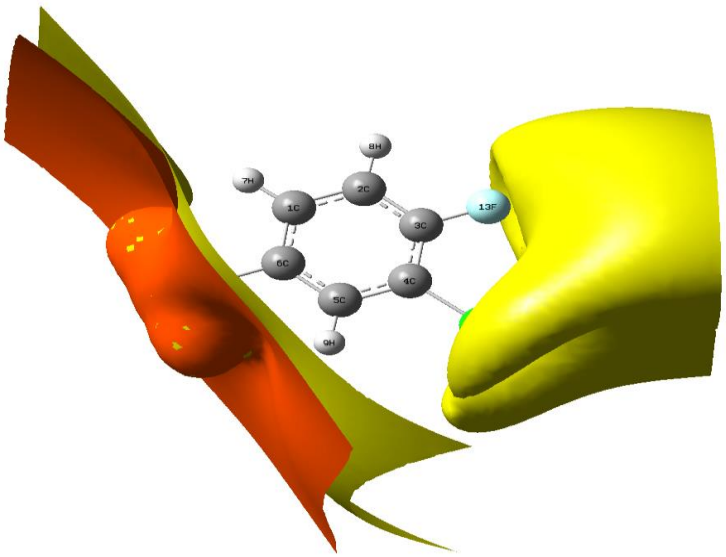

Figure 3. 3D plots of ESP picture of the 2-chloro-1-fluoro-4-nitrobenzene compound.

The map reveals the most negatively charged regions are concentrated round the nitrogen oxide and halogen atoms, indicating that the sites are prone to electrophilic interactions due to the delocalization of their π-electrons. In contrast, other compounds exhibit nucleophilic reactivity sites, highlighting their role as electron-rich sites within the molecule.

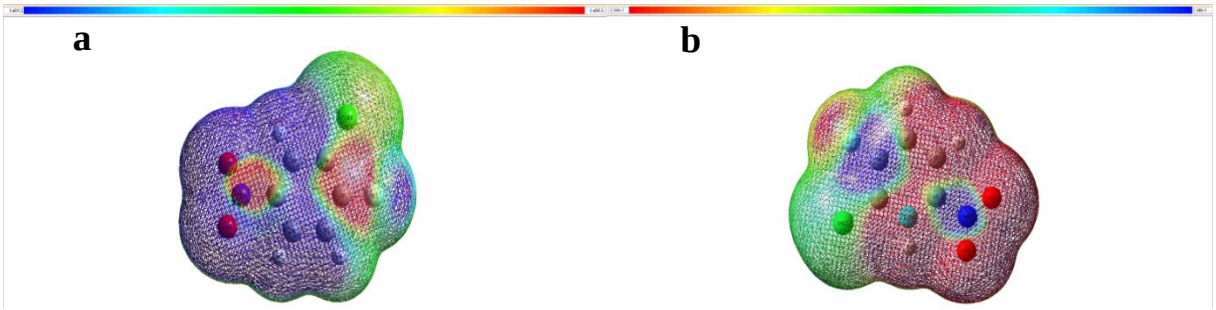

Figure 4. 3D plots of MEP image belonging to 2-chloro-1-fluoro-4-nitrobenzene molecule.

Additionally, the MEP image, which maps the interaction energy between the electron and nuclear charges with a hypothetical positive test charge, is simulated (from both sides) for the molecule and depicted in Figure 4a-b. The MEP image serves as an essential indicator of chemical reactivity by reflecting electron density distribution and revealing areas prone to electrophilic and nucleophilic attacks, as well as potential hydrogen-bonding sites (Politzer & Murray, 2002). The image of MEP extends to understanding how external magnetic fields influence biological and chemical properties, such as in vitro regeneration, phenolic composition, growth, antioxidant activity, and enzymatic defense responses of organic and herbal compounds (Ulgen et al., 2017). The MEP map reveals regions of reactivity, where red areas indicate sites favorable for electrophilic attack and blue areas indicate sites favorable for nucleophilic reactivity. The highest negative potentials, indicating electrophilic reactivity, are concentrated around certain carbon and nitrogen atoms, while positive potentials, indicating nucleophilic behavior, are seen around bromine and hydrogen atoms. In this respect, the MEP findings demonstrate the complex reactivity profile of the 3-chloro-4-fluoronitrobenzene molecule, capable of engaging in both electrophilic and nucleophilic interactions. The distinct charge distribution further suggests potential for metallic bonding and other intermolecular interactions, underscoring its potential for an extensive range of chemical application fields. In conclusion, the simulations obtained for the 2-chloro-1-fluoro-4-nitrobenzene molecule indicate clearly that the compound with high reactive parts is ideal for the advanced applied sciences.

5. Conclusion

In the current work, we try to define the reactivity and stability of the 3-chloro-4-fluoronitrobenzene molecule for the future application fields as regards advanced applied sciences, physics, industry, chemistry, biology, medicine, pharmaceuticals, dyes, and agrochemicals of the compound, we

make some calculations including vibrational frequencies, dipole moments, related assignments of vibrations, optimized molecular structures, atomic charge distributions, ICT regions, thermodynamic properties at 300 K, UV-vis absorption maxima, functional group identifications, electrophilic/nucleophilic aromatic regions, charge transfer characteristics, lone (non-bonding) pairs, chemical hardness, energy band gap, molecular softness, and electronegativity NMR chemical shifts, conjugation of π bonds, and electron engagement regions. Besides, we simulate, for the first time, 2D total charge contours, MEP, LUMO, ESP, and HOMO images of the 3-chloro-4-fluoronitrobenzene compound. We also compare the NMR and FTIR spectra with the theoretical computations. According to the comparisons, the calculations are closely aligned with experimental ones. The findings also reveal that the compound possesses high ICT regions, lone pairs, electron-donating groups, π-bond conjugation, and especially electrophilic/nucleophilic aromatic regions. This points out that the material has a potential for metallic bonding and intermolecular interactions. Overall, this study not only aids in the identification of the molecule analyzed but also provides valuable insights for researchers, supporting both foundational research and practical applications in technology and industry.

Conflict of Interest

The authors declare that they have no conflict of interest.

References

Altunpak, Y., Yaşar, M., & Önal, M., (2019). Electrical sliding wear behaviour of an aged high conductivity cu-be alloy. *IOSR Journal of Engineering*, *09*(11), 53-60.

Avci, D., & Atalay, Y. (2009). Theoretical analysis of vibrational spectra and scaling-factor of 2-aryl-1, 3, 4-oxadiazole derivatives. *International Journal of Quantum Chemistry*, *109*(2), 328-341. https://doi.org/10.1002/qua.21789

Baraistka, H., Labudzinska, A., & Terpinski, J. (1987). *Laser Raman spectroscopy: Analytical applications (Series: Ellis Horwood series in analytical chemistry)*. Ellis Harwood Publishers.

Becke, A. D. (1992). Density-functional thermochemistry. I. The effect of the exchange-only gradient correction. *The Journal of Chemical Physics*, *96*(3), 2155-2160. https://doi.org/10.1063/1.462066

Buyukuslu, H., Akdogan, M., Yildirim, G., & Parlak, C. (2010). Ab initio Hartree-Fock and density functional theory study on characterization of 3-(5-methylthiazol-2-yldiazenyl)-2-phenyl-1H-indole. *Spectrochimica Acta Part A: Molecular and Biomolecular Spectroscopy*, *75*(4), 1362-1369. https://doi.org/10.1016/j.saa.2010.01.003

Chen, J., & Wang, H. (2021). Density, viscosity, and saturated vapour pressure of 3-chloro-4-fluoronitrobenzene and 3-chloro-2-fluoronitrobenzene. *The Journal of Chemical Thermodynamics*, *154*, 106337. https://doi.org/10.1016/j.jct.2020.106337

Coates, J. (2006). Interpretation of infrared spectra, a practical approach. *Encyclopedia of Analytical Chemistry: Applications, Theory and Instrumentation*, *12*, 10815-10837. https://doi.org/10.1002/9780470027318.a5606

Dennington, R., Keith, T., & Millam, J. (2007). *GaussView, Version 4.1.2*. Semichem Inc., Shawnee Mission.

Ertem, A. G., & Altunpak, Y. (2019). Effect of electrode materials type on resistance spot welding of AISI 304 austenitic stainless steel (ASS) sheets. *International Journal for Research in Applied Science and Engineering Technology*, *7*(11), 280-284. https://doi.org/10.22214/ijraset.2019.11045

Fogarasi, G., & Pulay, P. (1986). Quantum chemical calculation of force constants and vibrational spectra. *Journal of Molecular Structure*, *141*, 145-152. https://doi.org/10.1016/0022-2860(86)80318-0

Fogarasi, G., Zhou, X., Taylor, P. W., & Pulay, P. (1992). The calculation of ab initio molecular geometries: Efficient optimization by natural internal coordinates and empirical correction by offset forces. *Journal of the American Chemical Society*, *114*(21), 8191-8201. https://doi.org/10.1021/ja00047a032

Foresman, J., & Frish, E. (1996). *Exploring chemistry with electronic structure methods*. Gaussian Inc.

Fukui, K. (1982). Role of frontier orbitals in chemical reactions. *Science*, *218*, 747-754. https://doi.org/10.1126/science.218.4574.747

Furche, F., & Ahlrichs, R. (2002). Adiabatic time-dependent density functional methods for excited state properties. *The Journal of Chemical Physics*, *117*(16), 7433-7447. https://doi.org/10.1063/1.1508368

Gece, G. (2008). The use of quantum chemical methods in corrosion inhibitor studies. *Corrosion Science*, *50*(11), 2981-2992. https://doi.org/10.1016/j.corsci.2008.08.043

Helgaker, T. U., Jensen, H. J. R. A., & Jørgensen, P. (1986). Analytical calculation of MCSCF dipole-moment derivatives. *The Journal of Chemical Physics*, *84*(11), 6280-6284. https://doi.org/10.1063/1.450772

Keresztury, G., Holly, S., Besenyei, G., Varga, J., Wang, A., & Durig, J. R. (1993). Vibrational spectra of monothiocarbamates-II. IR and Raman spectra, vibrational assignment, conformational analysis and ab initio calculations of S-methyl-N, N-dimethylthiocarbamate. *Spectrochimica Acta Part A: Molecular Spectroscopy*, *49*(13-14), 2007-2026. https://doi.org/10.1016/S0584-8539(09)91012-1

Kikuchi, M., Nakagawa, M., Tone, S., Saito, H., Niino, T., Nagasawa, N., & Sawai, J. (2016). Predicting changes in aquatic toxicity of chemicals resulting from solvent or dispersant use as vehicle. *Chemosphere*, *154*, 34-39. https://doi.org/10.1016/j.chemosphere.2016.03.030

Kohn, W., Becke, A. D., & Parr, R. G. (1996). Density functional theory of electronic structure. *The Journal of Physical Chemistry*, *100*(31), 12974-12980. https://doi.org/10.1021/jp960669l

Krishnakumar, V., Prabavathi, N., & Muthunatesan, S. (2008). Density functional theory calculations and vibrational spectra of 6-methyl 1, 2, 3, 4-tetrahyroquinoline. *Spectrochimica Acta Part A: Molecular and Biomolecular Spectroscopy*, *69*(3), 853-859. https://doi.org/10.1016/j.saa.2007.05.034

Lewis, D. F. V., Ioannides, C., & Parke, D. V. (1994). Interaction of a series of nitriles with the alcohol-inducible isoform of P450: Computer analysis of structure—activity relationships. *Xenobiotica*, *24*(5), 401-408. https://doi.org/10.3109/00498259409043243

Morikawa, A., Furukawa, T. A., & Moriyama, Y. (2005). Synthesis and characterization of novel aromatic polyimides from bis (4-amino-2-biphenyl) ether and aromatic tetracarboxylic dianhydrides. *Polymer Journal*, *37*(10), 759-766. https://doi.org/10.1295/polymj.37.759

Olsen, J., & Jørgensen, P. (1985). Linear and nonlinear response functions for an exact state and for an MCSCF state. *The Journal of Chemical Physics*, *82*(7), 3235-3264. https://doi.org/10.1063/1.448223

Polavarapu, P. L. (1990). Ab initio vibrational Raman and Raman optical activity spectra. *Journal of Physical Chemistry*, *94*(21), 8106-8112. https://doi.org/10.1021/j100384a024

Politzer, P., & Abu-Awwad, F. (1998). A comparative analysis of Hartree-Fock and Kohn-Sham orbital energies. *Theoretical Chemistry Accounts*, *99*, 83-87. https://doi.org/10.1007/s002140050307

Politzer, P., & Murray, J. S. (2002). The fundamental nature and role of the electrostatic potential in atoms and molecules. *Theoretical Chemistry Accounts*, *108*, 134-142. https://doi.org/10.1007/s00214-002-0363-9

Pulay, P., Fogarasi, G., Pongor, G., Boggs, J. E., & Vargha, A. (1983). Combination of theoretical ab initio and experimental information to obtain reliable harmonic force constants. Scaled quantum mechanical (QM) force fields for glyoxal, acrolein, butadiene, formaldehyde, and ethylene. *Journal of the American Chemical Society*, *105*(24), 7037-7047. https://doi.org/10.1021/ja00362a005

Rauhut, G., & Pulay, P. (1995). Transferable scaling factors for density functional derived vibrational force fields. *The Journal of Physical Chemistry*, *99*(10), 3093-3100. https://doi.org/10.1021/j100010a019

Ravi, R., Sivaramakrishnan, H., & Nagarajan, K. (1997). Nucleophilic substitutions on 3-chroro-4-fluoronitrobenzene. *Indian Journal of Chemistry Section B-Organic Chemistry Including Medicinal Chemistry*, *36*(4), 347-348.

Rintoul, L., Micallef, A. S., & Bottle, S. E. (2008). The vibrational group frequency of the N–O stretching band of nitroxide stable free radicals. *Spectrochimica Acta Part A: Molecular and Biomolecular Spectroscopy*, *70*(4), 713-717. https://doi.org/10.1016/j.saa.2007.08.017

Saiardi, A., Erdjument-Bromage, H., Snowman, A. M., Tempst, P., & Snyder, S. H. (1999). Synthesis of diphosphoinositol pentakisphosphate by a newly identified family of higher inositol polyphosphate kinases. *Current Biology*, *9*(22), 1323-1326. https://doi.org/10.1016/S0960-9822(00)80055-X

Schell, M. J., Letcher, A. J., Brearley, C. A., Biber, J., Murer, H., & Irvine, R. F. (1999). PiUS (Pi uptake stimulator) is an inositol hexakisphosphate kinase. *FEBS Letters*, *461*(3), 169-172. https://doi.org/10.1016/S0014-5793(99)01462-3

SDBS. (2024). *Spectral database for organic compounds, SDBS*. https://sdbs.db.aist.go.jp/

Spencer, J., Rathnam, R. P., Patel, H., & Anjum, N. (2008). Microwave mediated reduction of heterocycle and fluorine containing nitroaromatics with Mo (CO) 6 and DBU. *Tetrahedron*, *64*(44), 10195-10200. https://doi.org/10.1016/j.tet.2008.08.036

Stephens, P. J., Devlin, F. J., Chabalowski, C. F., & Frisch, M. J. (1994). Ab initio calculation of vibrational absorption and circular dichroism spectra using density functional force fields. *The Journal of Physical Chemistry*, *98*(45), 11623-11627. https://doi.org/10.1021/j100096a001

Ulgen, C., Yıldırım, A. B., & Turker, A. U. (2017). Effect of magnetic field treatments on seed germination of melissa officinalis L. *International Journal of Secondary Metabolite*, *4*(3, Special Issue 1), 43-49. https://doi.org/10.21448/ijsm.356283

Ulgen, C., Yıldırım, A., & Turker, A. (2020). Enhancement of plant regeneration in lemon balm (*Melissa officinalis* L.) with different magnetic field applications. *International Journal of Secondary Metabolite*, *7*(2), 99-108. https://doi.org/10.21448/ijsm.677102

Ulgen, C., Yildirim, A. B., Sahin, G., & Turker, A. U. (2021). Do magnetic field applications affect in vitro regeneration, growth, phenolic profiles, antioxidant potential and defense enzyme activities (SOD, CAT and PAL) in lemon balm (*Melissa officinalis* L.). *Industrial Crops and Products*, *169*, 113624 https://doi.org/10.1016/j.indcrop.2021.113624

Wang, D. L., Sun, X. P., Shen, H. T., Hou, D. Y., & Zhai, Y. C. (2008). A comparative study of the electrostatic potential of fullerene-like structures of Au_{32} and Au_{42}.

Chemical Physics Letters, *457*(4-6), 366-370. https://doi.org/10.1016/j.cplett.2008.04.038

Wilson, E. B., Decius, J. C., & Cross, P. C. (1980). *Molecular vibrations: The theory of infrared and Raman vibrational spectra*. Courier Corporation.

Wojtkowiak, B., & Chabanel, M. (1977). *Spectrochimie moléculaire*. Paris: Technique et documentation. (In French)

Wu, Q., & Yang, W. (2002). Empirical correction to density functional theory for van der Waals interactions. *The Journal of Chemical Physics*, *116*(2), 515-524. https://doi.org/10.1063/1.1424928

Zhang, Y., Ma, Z., Yang, M., Chen, Y., Tang, B., & Zhu, T. (2024). Preparation of modified graphyne to detect genotoxic impurities in gefitinib: Effects of ionic liquid structures and carbon nanotube composite modes. *Microchemical Journal*, *201*, 110651. https://doi.org/10.1016/j.microc.2024.110651

http://jaasci.com
JOURNAL OF ADVANCED APPLIED SCIENCES
e-ISSN: 2979-9759
https://prensip.gen.tr

RESEARCH ARTICLE

Investigation of the Effect of Electrode Type on Microstructure and Mechanical Properties in the Welding Process of Miilux 500 Protection Armour Steels with Shielded Metal Arc Welding Method

Hakan Ada[1,2]✉ • Muhammed Ahmet Çobanoğlu[3] • Nihat Kaya[4]

[1]Gazi University, Faculty of Technology, Department of Metallurgical and Materials Engineering, Ankara/Türkiye
[2]Kastamonu University, Faculty of Engineering and Architecture, Department of Mechanical Engineering, Kastamonu/Türkiye
[3]Kastamonu University, Institute of Science, Department of Mechanical Engineering, Kastamonu/Türkiye
[4]Osmaniye Korkut Ata University, Kadirli Vocational School, Department of Mechanical Program, Osmaniye/Türkiye

ARTICLE INFO

Article History
Received: 22.10.2024
Accepted: 10.12.2024
First Published: 30.12.2024

Keywords
Armour steel
Citochromax
Miilux Protection 500
Shielded metal arc welding
Tenacito 80

ABSTRACT

This study highlights the critical importance of electrode selection in ensuring the mechanical integrity and metallurgical reliability of welded armour steel, contributing valuable insights for future applications in the defence industry. In this study, plates produced from Miilux Protection 500 armour steel were joined by the electric arc welding method with Citochromax and Tenacito 80 shielded electrodes produced by Magmaweld. To characterise the mechanical and metallurgical performances of the joints, tensile, hardness and bending tests were performed on the samples taken from the joints and optical microscope and SEM examinations were performed. When all the results were evaluated in the shielded electrode electric arc welding applications of Protection 500 armour sheets of steel, the most suitable metallurgical and mechanical performance electrode was Tenacito 80.

Please cite this paper as follows:

Ada, H., Çobanoğlu, M. A., & Kaya, N. (2024). Investigation of the effect of electrode type on microstructure and mechanical properties in the welding process of Miilux 500 Protection armour steels with shielded metal arc welding method. *Journal of Advanced Applied Sciences*, *3*(2), 55-65. https://doi.org/10.61326/jaasci.v3i2.300

1. Introduction

Throughout history, humanity has instinctively wanted to survive and sustain its life. With this instinctive effect, it has developed itself against various threats from nature. In the early periods, these developments appear as shelters, caves and dwellings for shelter. With the impact of harsh living conditions and harsh conditions, the need for protection has evolved from structural protection to personal protection. Within the scope of personal protection, people have tried to take precautions against complex natural conditions and threats such as attacks, wild animal attacks, bumps, impacts and various injuries by developing protective clothing, covers, headgear and footwear (Baykara et al., 2020).

✉ Correspondence
E-mail address: hakanada@gazi.edu.tr

The materials used for personal protection became unable to fulfil their primary task with the development of threat elements, and this situation forced the development of materials used in personal protection, which are defence materials. The use of threat elements such as spears and axes made with complex and sharp-edged rocks revealed the weakness of defence materials, and with the development of metal production and processing skills, the era of metallic materials as personal protection began. With the discovery of alloying, people saw that bronze was effective in personal protection and attack materials and applied alloying to threat and defence materials. In response to various threats, various personal protective materials have been produced, leading to the concept of armour (Baykara et al., 2020).

While in the past, sharp axes, spears and arrows constituted threat members, today, advanced modern weapons, kinematic and explosive projectiles, grenades, and mines constitute threat members. Subsequently, the development of armour materials has become a necessity. Modern armour materials include metal, polymer, ceramic and composite-based armour. When the developments are examined, it is seen that threat elements and armour materials that will eliminate threat elements have developed in parallel over time (Kara, 2012).

Armour materials must maintain their structural integrity and resist cracking, fragmentation, and breakage against various kinematic projectiles that will apply impact loads to fulfil and continue their mission against the threat element (Laible, 1980). In this respect, armour materials should be selected by considering the characteristics of threat elements and armour materials. Table 1 below shows the armour materials used against 7.62 and 14.5 mm armour-piercing ammunition.

Table 1. Armour materials used against 7.62 and 14.5 mm armour-piercing bullets (Karagöz & Atapek, 2007).

Armour Materials	
Steel	Glass Reinforced E-cam
- RHA (380 HB)	- S glass
- High Hardness (550 HB)	
- Dual Hardness Armour (440-600 HB)	
Aluminum	Ceramic
- 5083 alloy	- Aluminum oxide
- 7039 alloy	- Aluminum oxide + Al
- 2519 alloy	- Boron carbide
	- Titanium dicarbide
Composite (Multilayer with ceramic surface)	
Al + RHA	
Steel + RHA	
E glass + RHA	

Metallic armour has become one of the prominent materials in modern armour technologies thanks to its wide range of mechanical properties and high production speeds, compared to other armour materials that offer different advantages in various application areas. Metallic armours are produced by alloying and heat treatment processes and are armour materials that effectively prevent various threat elements (Laible, 1980). Metallic armours are preferred to achieve desired mechanical properties such as hardness, toughness and strength. Thanks to their excellent formability, ductility and weldability, these armours can be formed to the desired size and shape and provide high production speeds. Metallic armours are generally divided into four main groups: aluminium, magnesium, steel and titanium (Hazell, 2022). Today, aluminium and steel metallic armours are prominent in machinability, cost and weldability to the desired geometry (Hazell, 2022).

Armour steels are one of the most essential materials that form the basis of widely used armour steels. It is constantly being improved metallurgically and mechanically. It is among the most preferred materials due to its superior ballistic performance and high weldability during manufacturing (Baykara et al., 2020). Reinforced steel sheets should be used in armoured vehicles where protection is required. Mechanical properties such as high tensile strength, yield strength and hardness are among the main reasons these steel sheets are preferred. However, the plastic deformation process is complicated in armour steels with high mechanical properties and strength. Cracks along the bend line may occur in the armour steel during deformation.

Since armour steels have high mechanical properties and strength, high forces must be applied during forming. Due to its poor plastic deformation capability, welding is one of the most suitable methods for bringing armour steels to the desired size and geometry. The methods used in welding armour steels include electric arc welding with covered electrodes, gas arc welding (TIG, MIG, MAG) and submerged arc welding. One of the most widely used methods is electric arc welding with a shielded electrode. Although this method is convenient, if the electrode contains moisture, there is a risk of hydrogen penetrating the weld zone and causing cracks during cooling. It is, therefore, important that the electrodes are thoroughly dried and free of moisture. In gas metal arc welding, the risk of

hydrogen is lower as there is no shroud to protect the welding bath. However, electrodes with low hydrogen content should be preferred for gas metal arc wire electrodes. Submerged arc welding can be used for long and linear welding processes. This method enables faster welding of armour steels with significant wall thickness. However, attention should be paid to the powder's hydrogen and moisture content (Yakut, 2015).

In welded joining processes, it is essential to determine the welding method and the filler material that best suits the chemical and mechanical properties of the base material. In a basic welded jointing process, the aim is for the weld seam to have higher mechanical properties than the base material. However, this is not yet possible for armour steels. In welding armour steels subjected to dynamic stress, pressure and impact, and cracking sensitivity, filler materials that exhibit higher mechanical properties than the base material have not yet been developed. For this reason, filler materials with good wetting properties, suitable for filling and forming a stress-relieving buffer layer, are generally preferred. These materials are used in welded joints, even though they are far from providing the mechanical properties of the base material (Gürol et al., 2022).

Miilux Protection 500 armour steel plates were joined in this study using the shielded electrode electric arc welding (SMAW) method. In this process, two different commercially available electrode wires (Citochromax and Tenacito 80), which were determined to be of suitable composition for the study, were preferred. The study aims to evaluate the effects of these filler materials used in industrial applications and the applied current intensity values on the mechanical and metallurgical properties of Miilux Protection 500 sheets of steel by comparative analysis. These analyses aim to reveal the effects of different electrodes and current intensities on the performance of Miilux Protection 500 steels.

2. Materials and Methods

In this study, armour steels of MIL-A 46100 class, which have high hardness and strength, were welded by arc welding with a shielded electrode. The welding speeds were kept constant, and the effects of changes in current strength on the microstructure and mechanical properties of the welded joints were investigated.

2.1. Material

Miilux Protection 500 armour steel with a section thickness of 4.2 mm and a hardness value of approximately 500 HBW was used in this study. The chemical composition and mechanical properties of Miilux Protection 500 armour steel are presented in Table 2.

Table 2. Chemical composition and mechanical properties of the armour steel used.

Steel Quality	Thickness (mm)	Element (%)								
		C	**Si**	**Mn**	**P**	**S**	**Cr**	**Ni**	**Mo**	**B**
Miilux Protection 500	4.00-40.00	0.30	0.70	1.70	0.015	0.005	0.75	0.80	0.50	0.004
	Hardness HBW	**Yield Strength Rp 0.2 (MPa)**		**Tensile Strength Rm (MPa)**		**Elongation (%)**		**Charpy Impact Resistance (-40°C) Joule**		**Carbon Equivalence (Ceq)**
	480-560	1300		1600		8		17		0.70

In this study, two different electrodes were selected for the welded joining of Miilux Protection 500 armour steels. The 3.25 mm diameter electrodes were produced by Magmaweld and named as Citochromax and Tenacito 80. The detailed list of these materials according to standards and company is presented in Table 3, and their chemical composition and mechanical properties are presented in Table 4.

Table 3. Nomenclature of the materials used in the study according to standards and company.

Filler Metal Diameter (mm)	Magmaweld Code	Standard and Nomenclature	AWS Code and Nomenclature
3.25	Citochromax	TS EN ISO 3581 - A E 18 8 Mn B 22	AWS/ASME SFA - 5.4 E307-15
	Tenacito 80	TS EN ISO 18275 - A E 69 6 Mn2NiCrMo B 42 H5	AWS/ASME SFA - 5.5 E11018-G H4

Table 4. Chemical composition and mechanical properties of the filler wires used in the study.

Filler Metal Type	Element (%)							
	C	Si	Mn	Cr	Ni	Mo	S	P
Citochromax	0.12	0.40	6.00	19.00	9.00	-	≤0.020	≤0.025
Tenacito 80	0.06	0.50	1.80	0.35	2.20	0.40	≤0.012	≤0.020

Mechanical Properties				
Filler Metal Type	Yield Strength (MPa)	Tensile Strength (MPa)	Elongation (%)	Impact Resistance (Joule) and Test Temperature
Citochromax	480	660	40	70 (20 °C)
Tenacito 80	775	890	18	50 (-60 °C)

2.2. Method

Birikim Engineering and Industrial Contracting Inc. carried out the welded joints of Miilux Protection 500 armour steels in Ankara by the standards. The plates prepared for welded joints were cut in 380x200x4.2 mm dimensions by TS EN ISO 15614-1 standard, considering the sample sizes required for test examinations. The beveling process of the supplied plates was carried out according to TS EN ISO 9692-1 standard and taking into account the filler material diameter. Y-type weld bead geometry was used in the study. The schematic representation of the weld bead geometry is given in Figure 1, and the weld bead dimensions determined according to the diameter of the filler metal are given in Table 5.

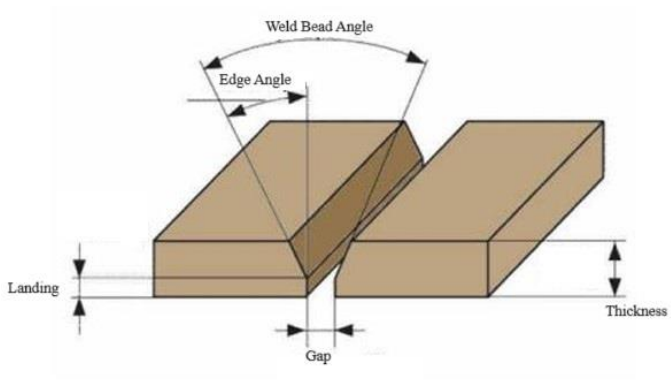

Figure 1. Demonstration of weld bead geometry.

Table 5. Measurements of weld bead geometries.

Thickness (mm)	Gap (mm)	Landing (mm)	Weld Bead Angle (°)	Edge Angle (°)
4.2	3.5	2.00	50	25

The welding parameters used in the welded joints of Miilux Protection 500 armour steel are presented in Table 6. According to Table 6, the current intensity values used in the experiments were determined based on the catalogue data of the electrode manufacturers and were selected as 100, 110 and 120 Amperes, respectively. Arc voltage and welding speed were kept constant in the experiments.

This study performed mechanical tests and microstructural investigations for each experiment. Mechanical tests include tensile, bending and hardness tests, which evaluate the mechanical performance of welded joints. Since armour steels are considered to be heat sensitive, the specimens were cut using a water jet. Sanding and polishing the samples for microstructure and macrostructure examinations were performed on a Siemens brand device. By the metallographic examination standards, 80, 120, 240, 240, 400, 800, 1200 and 2500 grit abrasives were used, and the samples were polished with 3 and 1 μm diamond solutions, respectively, using polishing felts. In order to determine the resistance of the polished specimens to plastic deformation, hardness tests were performed on the specimens after microstructure examination. Hardness measurements were carried out with 50 measurements from 25 points at equal distances to the weld centre's left (-) and right (+) until the base material's hardness was determined per TS EN ISO 9015-2 standard (Figure 2). The distance between hardness measurements was set as 0.5 mm, and the centre of the weld metal (point 0) was taken as the reference point. Since it was observed that the hardness values of the base material could not be reached due to the HAZ (Heat-Affected Zone) width caused by the heat input effect, additional hardness measurements were made at 1 mm intervals from point 26 to point 37, where the base material hardness values were obtained. Hardness tests were performed using the Shimadzu brand and HMV-G21 model device under 1 kg load and the Vickers hardness measurement method.

Table 6. Welding parameters.

Experiment No.	Electrode	Diameter (mm)	Current Intensity (Ampere)	Voltage (V)	Welding Speed (cm/min)
N1	Citochromax	Ø3.25	100	22.5	9.5
N2			110		
N3			120		
N4	Tenacito 80		100		
N5			110		
N6			120		

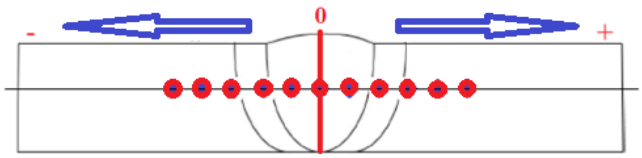

Figure 2. Schematic representation of hardness tests.

For tensile tests, specimens taken from welded joint plates were prepared by the TS EN ISO 4136 standard and specimens taken from the base material were prepared by the TS EN ISO 6892-1 standard. Tensile specimens prepared by the standards were tested at room temperature with an Instron brand 8503 model device with 500 kN capacity. In order to measure the elongation of the specimens during the tensile process, the first measurement length was marked on the specimens before the test, and the elongation amounts were determined by measurements made after the test.

In order to evaluate the elastic and plastic deformations of the materials joined by the welding process and to check the suitability of the weld, test specimens were prepared by TS EN ISO 5173 standard and bending tests were performed. Bending tests were performed with a 500 kN capacity Hidroliksan brand device. The tests were performed at room temperature, 180° bending angle and using a 20 mm diameter chuck, and the distance between the bearings was set to 28.4 mm.

3. Results

Macrostructure, microstructure, hardness, tensile and bending tests were performed on the samples taken from the welded joints and the findings are presented below.

3.1. Macrostructure Review

From the macrostructure images, it is clear that the penetrations are complete, and, as expected, the melting line and HAZ in the weld zone are observed. When the macrostructure images in Figure 3 and Figure 4 are evaluated, the melting line and HAZ are more clearly observed in the macrostructures of the welds made with Citochromax-coded weld metal showing austenitic stainless steel properties and in the images of the joints made with Tenacito 80 welding materials showing ferritic properties. It is observed that the grains are directed towards the weld centre in the direction of heat escape.

Figure 3. Macrostructure images of the welded joint made with the Citochromax coded electrode (Ø3.25 mm) a) N1, b) N2 and c) N3.

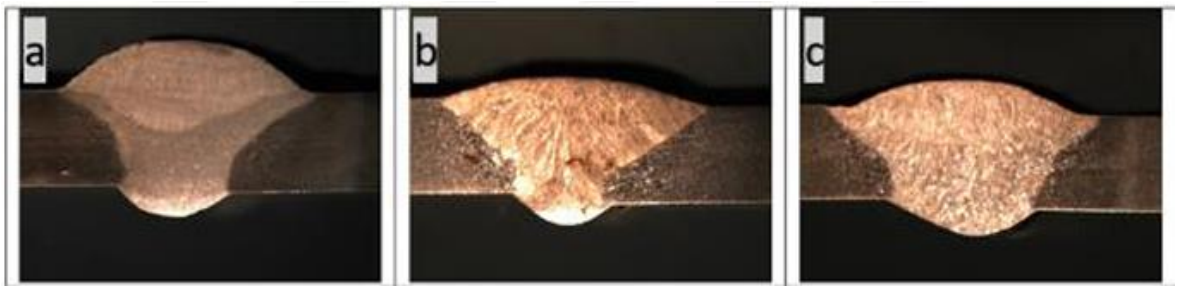

Figure 4. Macrostructure images of the welded joint made with Tenacito 80 electrode (Ø3.25 mm) a) N4, b) N5 and c) N6.

3.2. Microstructure Review

In order to evaluate the microstructural effects of Protection 500 welds made at various current values using the shielded electrode arc welding method, optical microscope examinations were performed on the samples. Microstructure images were obtained at 200 and 500 times magnification. The microstructure image of the base material is shown in Figure 5.

The optical microscope images in the figure show that the base material exhibits a fine-grained microstructure. The images show that martensitic and ferritic regions are dominant in the microstructure. While the martensitic structure gives armour steels high hardness and strength, it occurs in needle-like and slat-type forms. In addition, needle-shaped and tapered acicular ferrites exhibit similar hardness effects (Jena et al., 2010).

Figure 5. Microstructure images of Miilux Protection 500 base material.

Microstructure images of welded joints are given in Figure 6. Citochromax electrode belongs to the austenitic stainless steel electrode class. This electrode contains approximately 8% Nickel (Ni) by weight, directly affecting the formation of the austenite phase. While the austenitic structure is formed with this electrode, a limited amount of delta ferrite is formed within the austenitic matrix during the joining processes. This creates ferritic structures in the weld metal, especially at the grain boundaries. The Tenacito 80 electrode, with its low carbon content, provides an excellent combination of strength and toughness in welded joints. This electrode forms an acicular ferrite microstructure of ferrite plates nested within austenite grains. Acicular ferrite is the most desirable structure in low-carbon steels and produces fine-grain structures. This allows high mechanical properties to be achieved in welded joints.

4. Discussion

4.1. Tensile Test Results

Tensile tests were performed on three specimens of the base material and welded joints. The test results are given in Table 7 and Figure 7. As seen from Table 7, the maximum tensile strengths, the averages of these strengths, % elongation values and % cross-sectional shrinkage of the base material and welded joint specimens were determined as a result of the tensile test. In order to avoid measurement uncertainties, the initial length and cross-sectional area of all specimens were marked before the test, and the post-test elongation and cross-sectional shrinkage were calculated separately.

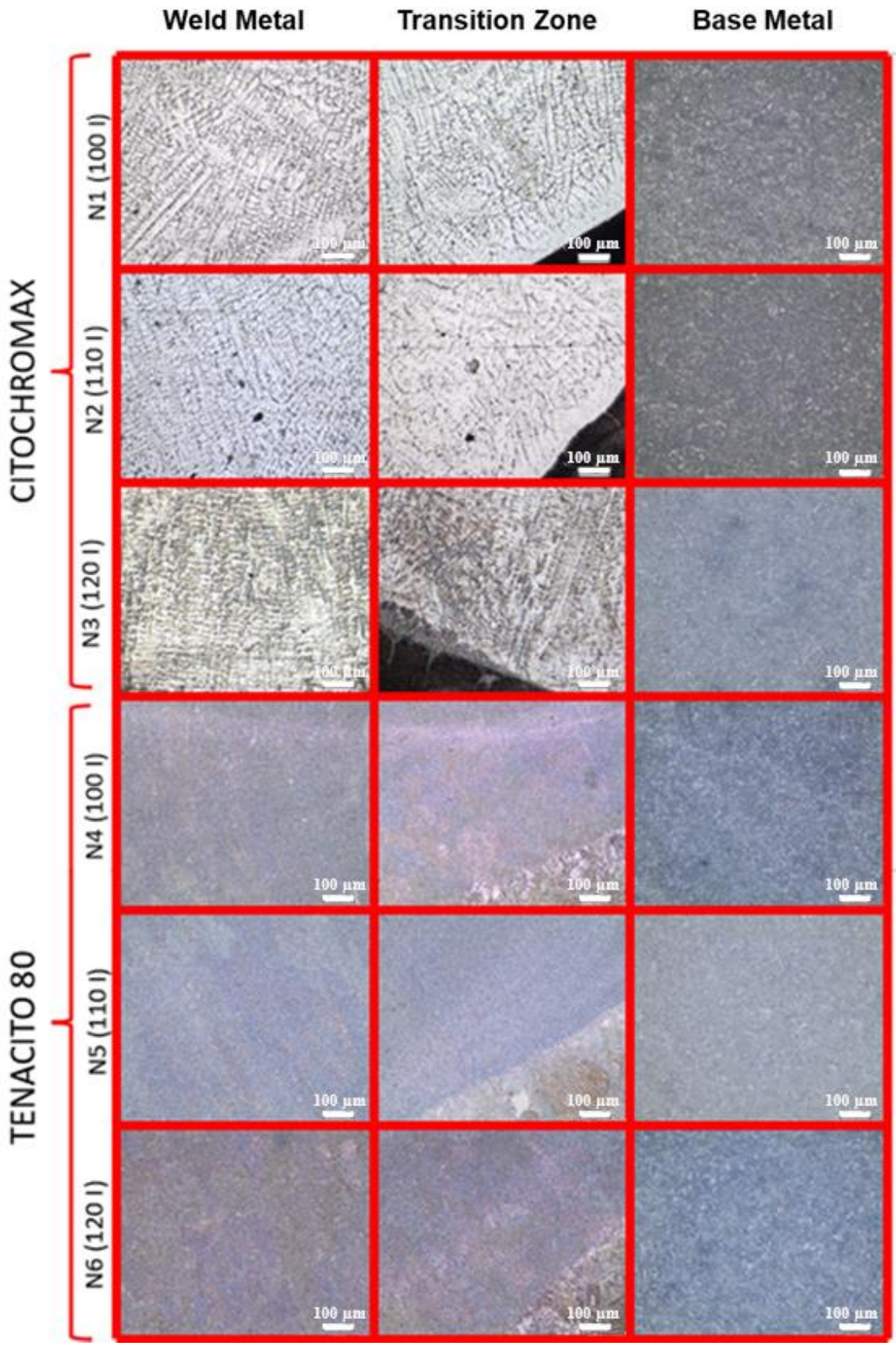

Figure 6. Microstructure images of welded joints.

Table 7. Tensile test results.

Filler Material	Experiment No.	Elongation (%)	Average Tensile Strength (MPa)
Base Material		6.69	1,768.19
Citochromax	N1	1.96	852.20
	N2	1.85	796.77
	N3	2.44	867.85
Tenacito 80	N4	4.30	951.24
	N5	5.15	957.31
	N6	5.12	940.98

When the tensile test result graph presented in Figure 7 is examined, it is seen that Protection 500 base material has a very high strength value. This material is used as an armour material due to its superior mechanical properties. However, during the welding process, there are significant differences between the strength values of the welded joints and the strength values of the base material due to the lack of a suitable electrode type for the base material and the heat applied negatively affects these superior properties of the armour steel. This is an expected result. Despite these expectations, in this study, suitable filler materials that can be used in welded joint processes for Protection 500 material were determined, and the metallurgical and mechanical performances of these materials were examined. In this way, it aims to create a guiding study for users regarding industrial use.

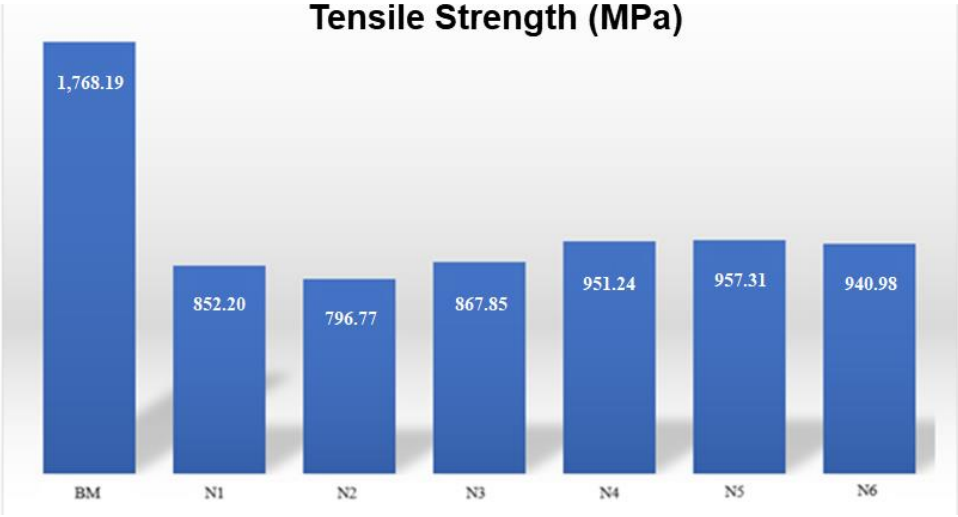

Figure 7. Tensile test results.

The maximum tensile strength of the welded joints was compared with the maximum tensile strength of the base material. The tensile test applied to the samples taken from the base material resulted in an average tensile strength of 1,768.19 MPa. The highest maximum tensile strength was obtained in experiment N5 with an average of 957.31 MPa with a Tenacito 80 coded electrode, and the lowest maximum tensile strength was obtained in experiment N2 with an average of 796.77 MPa with a Citochromax coded electrode. In all welded joints, ruptures occurred from the centre of the weld metal.

4.2. Hardness Investigations

Hardness tests were conducted on welded plates to measure the resistance of welded joints against plastic deformation. In this study, 75 measurements were taken from each welded sample. The hardness results of the welded joints made using shielded electrodes are shown in Figure 8. To minimise measurement uncertainties, all results are presented within a tolerance range of ±5 HV.

When examining the hardness test result graphs, it was observed that similar hardness curves were formed in all joints. The hardness graphs obtained from the welded joints with different parameters on Protection 500 material generally resemble each other. However, the hardness values vary depending on the current intensity and electrode type. In all experiments' hardness graphs, the region with the highest hardness is the HAZ, while the region with the lowest hardness is the weld metal zone. This situation is similar to other studies on weldability (Aksöz et al., 2017a; Çetinkaya et al., 2023).

It has been observed that the heat applied during the welding processes creates a heat treatment effect on the material, affecting specific areas. The experiments revealed that the highest hardness values were obtained in the HAZ. In experiments with high current intensity, the amount of heat entering the material increased, resulting in coarser grains and a wider spread of the HAZ. According to the data obtained from tensile tests, it was observed that the HAZ expanded in experiments with higher heat application and larger grains

formed. This situation led to a decrease in the strength values of the joints while causing an increase in the percentage elongation values. In experiments where coarse-grained structures were formed, lower hardness values were measured compared to other experiments that resulted in finer-grained structures due to the effects of applied current intensity and cooling rate. The values obtained from the tensile tests confirmed the directly proportional relationship between hardness and strength. This situation is similar to other studies on weldability (Aksöz et al., 2017b; Çoban et al., 2023; Harman et al., 2022).

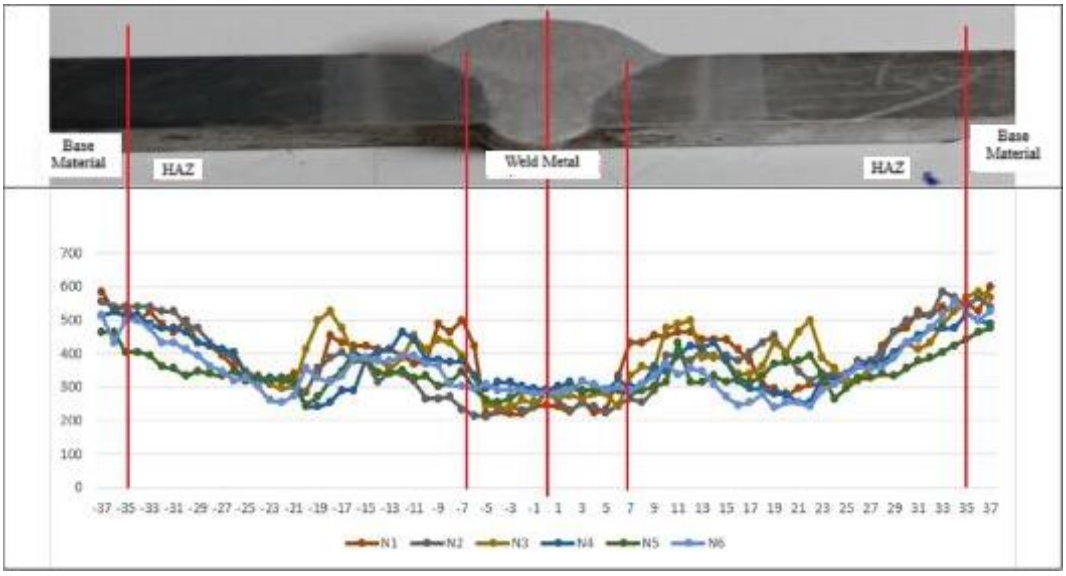

Figure 8. Hardness test results.

4.3. Bending Test Results

Bending tests were conducted on samples with the weld region centred by the TS EN ISO 5173 standard. The welded joints were tested in two directions: cap and root bending. 12 bending test samples were prepared, with two samples for each test. These tests aimed to determine whether the welded joints exhibited a performance close to the ductility of the base material. Additionally, this method revealed potential defects in the welded joints, confirming their suitability. The acceptable welded joints reached a bending angle of 180°, while the unsuitable ones are presented in Table 8 with their fracture angles within a tolerance range of ±2°.

Table 8. Bending test results.

Filler Metal	Experiment No.	Current Intensity	Filler Metal Diameter (mm)	Mandrel Diameter (mm)	Support Span (mm)	Bending Angle (°)	Face Bend Angle (°)	Root Bend Angle (°)
Citochromax	N1	100	3.25	20	28.4	180	180°	175°
	N2	110					72°	65°
	N3	120					54°	175°
Tenacito 80	N4	100					180°	74°
	N5	110					180°	180°
	N6	120					180°	55°

As a result of the bending tests, the samples that underwent plastic deformation are shown in Figures 9 and 10. In order to avoid repetition in the visualisation, images of the bent specimens obtained from experiments carried out with an average current intensity of 110 A for each type of electrode are shown. During the bending test, the samples were subjected to compressive stresses on the inner surfaces and tensile stresses on the outer surfaces. As a result, expansion occurred on the

inner surface, while cross-sectional reductions occurred on the outer surface.

Figure 9. Bended specimens.

Figure 10. Bended specimens.

5. Conclusion

In this study, Miilux Protection 500 armour steels were welded using shielded metal arc welding with Citochromax and Tenacito 80 electrodes, and the microstructure and mechanical properties of the welded joints were examined. The results obtained from the study are summarised below.

- From the macrostructure images, it can be seen that the penetrations have formed completely and as expected; the fusion line and HAZ in the weld region are observed.
- Microstructural investigations revealed the formation of austenitic and ferritic microstructures, while it was determined that martensitic and acicular ferrite structures predominated in the weld metal.
- The tensile tests showed that the Protection 500 base material has a significantly high strength value. The highest maximum tensile strength in the welded joints was obtained in the N5 experiment using the TENACITO 80 electrode, averaging 957.31 MPa. In contrast, the lowest maximum tensile strength was recorded in the N2 experiment welded with the CITOCHROMAX electrode, averaging 796.77 MPa.
- In the tensile tests, the fractures in the welded joints occurred as expected from the weld metal.
- In the hardness graphs obtained from welded joints made with different parameters on Protection 500 material, the hardness values varied according to the applied current intensity and electrode type.
- In the hardness graphs of all experiments, the region with the highest hardness was measured as the HAZ, while the region with the lowest hardness was the weld metal zone.

Acknowledgment

This manuscript study was presented as an abstract at the 5th International Congress on Engineering and Life Science held in Romania on September 10-12, 2024. In addition, the authors would like to thank Kastamonu University Scientific Research Projects Coordinatorship for supporting the study with the project number KÜ-BAP01/2019-34, Birikim Engineering Company where the welded joints were made, Magmaweld where filler materials were supplied, Kastamonu University Faculty of Engineering and Architecture, Department of Mechanical Engineering where microstructure and hardness examinations were performed, Gazi University Faculty of Technology, Department of Metallurgical and Materials Engineering where tensile tests were performed, Karabük University Faculty of Technology, and Department of Manufacturing Engineering where macro images were taken and bending tests were performed.

Conflict of Interest

The authors declare that they have no conflict of interest.

References

Aksöz, S., Ada, H., & Özer, A. (2017a). Toz altı kaynak yöntemiyle üretilen API 5l x70 kalite çelik boruların mikroyapı ve mekanik özellikleri. *Gazi Üniversitesi Fen Bilimleri Dergisi Part C: Tasarım ve Teknoloji*, *5*(1), 55-64. (In Turkish)

Aksöz, S., Ada, H., Fındık, T., Çetinkaya, C., Bostan, B., & Candan, İ. (2017b). API 5L X65 çeliklerinin elektrik ark kaynak yöntemi ile birleştirilmesinde, kaynak işleminin mikroyapı ve mekanik özelliklere etkisinin incelenmesi. *El-Cezerî*, *4*(1), 72-81. https://doi.org/10.31202/ecjse.289639 (In Turkish)

Baykara, T., Günay, V., & Demirural, V. (2020). *Zırh teknolojileri*. Yeditepe Ünivesitesi Yayınevi. (In Turkish)

Çetinkaya, C., Taşçı, S., & Ada, H. (2023). 3Cr12 ferritik paslanmaz çeliklerin gaz metal ark kaynağıyla birleştirilmesinde ilave tel türünün mikroyapı ve mekanik özelliklere etkisinin araştırılması. *Politeknik Dergisi*, *26*(4), 1651-1660. https://doi.org/10.2339/politeknik.1392366 (In Turkish)

Çoban, M., Ada, H., & Çetinkaya, C. (2023). AISI 304l östenitik paslanmaz çeliklerin lazer kaynağıyla birleştirilmesinde nitrasyon işleminin mikroyapı ve

mekanik özelliklere etkisinin araştırılması. *Gazi Üniversitesi Fen Bilimleri Dergisi Part C: Tasarım ve Teknoloji*, *11*(4), 1171-1182. https://doi.org/10.29109/gujsc.1388280 (In Turkish)

Gürol, U., Karahan, T., Erdöl, S., Çoban, O., Baykal, H., & Koçak, M. (2022). Characterization of armour steel welds using austenitic and ferritic filler metals. *Transactions of the Indian Institute of Metals*, *75*, 757-770. https://doi.org/10.1007/s12666-021-02464-7

Harman, M., Ada, H., & Çetinkaya, C. (2022). QStE420TM çelik malzemelerin farklı bazik elektrodlar kullanılarak örtülü elektrodla ark kaynak yöntemiyle kaynaklanabilirliğinin araştırılması. *Gazi Üniversitesi Mühendislik Mimarlık Fakültesi Dergisi*, *37*(4), 2041-2056. https://doi.org/10.17341/gazimmfd.893705 (In Turkish)

Hazell, P. J. (2022). *Armour: Materials, theory, and design*. CRC Press. https://doi.org/10.1201/9781003322719

Jena, P. K., Mishra, B., RameshBabu, M., Babu, A., Singh, A. K., SivaKumar, K., & Bhat, T. B. (2010). Effect of heat treatment on mechanical and ballistic properties of a high strength armour steel. *International Journal of Impact Engineering*, *37*(3), 242-249. https://doi.org/10.1016/j.ijimpeng.2009.09.003

Kara, S. (2012). *Çelik esaslı zırh malzemesinin 307si elektrodu ile kaynak edilebilirliğinin ve mikroyapı üzerindeki etkisinin deneysel araştırılması* (Master's thesis, Fırat University). (In Turkish)

Karagöz, Ş., & Atapek, H. (2007). *Bor katkılı zırh çeliklerinin kırılma davranışı*. 8. Uluslar Arası Kırılma Konferansı. İstanbul. (In Turkish)

Laible, R. C. (1980). *Ballistic materials and penetration mechanics*. Elsevier Scientific Publishing.

Yakut, V. (2015). *Zırh çeliklerinin ferritik ve östenitik dolgu malzemeleriyle kaynağının incelenmesi* (Master's thesis, Sakarya University). (In Turkish)

JAASCI
http://jaasci.com
JOURNAL OF ADVANCED APPLIED SCIENCES
e-ISSN: 2979-9759
PRENSİP
https://prensip.gen.tr

RESEARCH ARTICLE

The Production of Rice Husk Ash and Blast Furnace Slag-Based Alkali-Activated Composites under High-Temperature Effects

Ahmet Filazi ✉ • Nesrin Kurtoğlu • Fatih Kural

Kırıkkale University, Kırıkkale Vocational School, Department of Construction Technology, Kırıkkale/Türkiye

ARTICLE INFO

Article History
Received: 01.12.2024
Accepted: 17.12.2024
First Published: 30.12.2024

Keywords
Alkali-activated slag concrete
Blast furnace slag
Fire resistance
Rice husk ash

ABSTRACT

Alkali-activated concretes offer several advantages over conventional Portland cement-based concretes, including environmental sustainability, cost-effectiveness, and improved permeability. The use of alkali-activated concretes, as a replacement for Portland cement, provides significant environmental benefits, such as reducing carbon dioxide emissions by up to 80%, and facilitates the recycling and reuse of industrial and agricultural by-products. This study focuses on the development of alkali-activated concrete by incorporating industrial by-products like blast furnace slag and rice husk ash. A mixture of alkali-activated concrete based on blast furnace slag will be prepared, with partial substitution of Portland cement by these by-products by weight. The study will investigate the effects of these substitutions on the flexural and compressive strengths of the concrete over periods of 7, 28, and 90 days, as well as its fire resistance at temperatures of 200, 400, 600, and 800°C. The aim of this research is to contribute to the advancement of alkali-activated concrete technology, promoting the use of industrial by-products in the creation of more sustainable and environmentally-friendly construction materials.

Please cite this paper as follows:

Filazi, A., Kurtoğlu, N., & Kural, F. (2024). The production of rice husk ash and blast furnace slag-based alkali-activated composites under high-temperature effects. *Journal of Advanced Applied Sciences*, *3*(2), 66-78. https://doi.org/10.61326/jaasci.v3i2.318

1. Introduction

The growing demand for cement, coupled with its significant greenhouse gas emissions and the high expenses associated with Portland cement (PC), has driven efforts to explore alternative, sustainable materials. Cement manufacturing accounts for approximately 5-7% of worldwide carbon dioxide emissions, highlighting the environmental impact of traditional production processes (Colangelo et al., 2021; Mathew & Joseph, 2018). Pozzolanic materials like fly ash, blast furnace slag, and silica fume are increasingly used to minimize Portland cement consumption, driving significant research interest in cement-free alternatives (Mehta & Siddique, 2018).

Alkali-activated composites (AAS), derived from industrial by-products like slag, fly ash, and rice husk ash, form sustainable geopolymer concretes. These materials react with alkaline activators to create a strong alumina-silicate network, with high-temperature curing enhancing strength. Their use reduces energy consumption and greenhouse gas emissions (Zhan et al., 2018). Alkali-activated concrete (AAS) offers a sustainable alternative to traditional cement by reducing carbon emissions and utilizing low-cost industrial by-products, addressing disposal issues. Heat-cured geopolymer concrete

✉ Correspondence
E-mail address: ahmetfilazi@kku.edu.tr

performs similarly or better than conventional concrete (Hardjito & Rangan, 2005; Sarker et al., 2013), but ambient curing needs further research. Heat-cured AAS can reduce CO_2 emissions by up to 80% (Singh & Middendorf, 2020). Geopolymers are innovative and sustainable building materials that serve as an eco-friendly alternative to traditional concrete binders. They are synthesized through the reaction of silicon- and aluminum-rich materials with alkaline activators, resulting in a durable, high-performance matrix. Commonly utilized raw materials for geopolymers include industrial by-products such as fly ash, metakaolin, and blast furnace slag, which not only reduce environmental waste but also minimize the carbon footprint of construction. A particularly noteworthy combination involves blast furnace slag and rice husk ash, which together form a robust geopolymer concrete. This mixture leverages the high reactivity of slag and the silica content of rice husk ash, producing a material with superior mechanical properties and resistance to chemical attack. By incorporating these readily available and often discarded materials, geopolymer technology aligns with principles of resource efficiency and circular economy, paving the way for more sustainable infrastructure development (Amran et al., 2021; Arularasi et al., 2021; Habert et al., 2011).

Hossain et al. (2021) found that incorporating 10-20% rice husk ash (RHA) by weight enhanced both short-term and long-term geopolymer properties. Similarly, Hwang and Huynh (2015) observed a 97% increase in tensile strength after 56 days of curing at 10 M NaOH, when 35% RHA was added to fly ash-based geopolymers. One-part geopolymers synthesized from rice husk ash (RHA) and sodium aluminate achieved a compressive strength of approximately 30 MPa, significantly higher than comparable materials, due to the almost complete reaction of RHA and the absence of crystalline byproducts (Sturm et al., 2016). Kim et al. (2014) used 10 M NaOH and sodium silicate to activate RHA in geopolymer mortar, achieving a compressive strength of 45 MPa after 28 days, demonstrating good resistance to sulfate and acid. The strength increased with higher alkali concentration and RHA content.

Manzoor et al. (2024) emphasize the potential of geopolymer concrete as a sustainable and fire-resistant alternative to traditional concrete, capable of enduring temperatures up to 1200°C while mitigating environmental impacts through the use of alumina- and silica-rich waste materials. study focuses on the use of blast furnace slag and rice husk ash, industrial by-products, to create alkali-activated concrete. The impact of replacing blast furnace slag with RHA (at 0%, 5%, 10%, 15%, 20%, and 25% by weight) on fire resistance and strength properties at various temperatures (200°C, 400°C, 600°C, 800°C) is explored.

2. Materials and Methods

2.1. Materials

The materials used in this study include Blast Furnace Slag (BFS), Rice Husk Ash (PK), and various activators. BFS, an industrial by-product, will serve as one of the primary components in the production of alkali-activated composite mortar. It is obtained by grinding the slag formed during the iron metallurgy processes in blast furnaces. The chemical composition of BFS shows low amounts of Al_2O_3, Fe_2O_3, and SO_3, but high levels of CaO, indicating a dominant calcium content compared to other compounds. Rice Husk Ash (PK) will be used as a partial replacement for BFS by weight. PK is primarily composed of SiO_2, indicating that it is silica-based, with higher potassium oxide (K_2O) content compared to sodium oxide (Na_2O), suggesting a higher presence of potassium ions (Table 1).

The activators used in this study include Sodium Hydroxide (NaOH), which will initiate and accelerate the alkali-activation process, and Sodium Silicate (Na_2SiO_3), which will be used to influence the reaction rate and improve the mechanical properties of the mortar. The sodium silicate solution used has a chemical composition of SiO_2 (26.5%), Na_2O (8.3%), and dH_2O (6.2%). Additionally, CEN Standard Sand, sourced from the Limak Batı Çimento San. ve Tic. A.Ş. Trakya Cement Factory, will be used to determine the mechanical properties of the mortar. The grain size distribution of the reference sand complies with the standards set by the European Standards Committee (CEN). These materials will be utilized to produce alkali-activated composite mortars, and their mechanical properties will be analyzed, contributing to the development of sustainable construction materials and the effective use of industrial by-products.

Table 1. Composition and characteristics of blast furnace slag and rice husk ash.

Oxides (%)	BFS	RHA
SiO_2	35.22	89.95
Al_2O_3	17.53	2.86
Fe_2O_3	0.67	1.92
CaO	37.62	0.83
MgO	5.52	0.62
SO_3	0.68	0.46
Na_2O	0.42	0.18
K_2O	1.73	3.09
Density (g/cm^3)	2.89	1.97
Blaine fineness (cm^2/g)	3955	5750
Loss on Ignition (%)	1.84	7.3

2.2. Composite Mortar Production

The details of the experiments conducted to optimize the production process and strength properties of alkali-activated slag (AAS) are provided below (Table 1). For the silica source in AAS, BFS and PK were ground to cement fineness and used as binders. Standard sand was chosen as the aggregate. Sodium hydroxide (NaOH) was used in varying amounts as the activator. The alkali-activated composite samples were cast into molds of 50x50x50 mm dimensions, according to ASTM C109 standards (ASTM International, 2002), and poured using NaOH alkali solution. Sodium hydroxide was dissolved in tap water in the laboratory to prepare the caustic solution, and the activation solution was allowed to cool to room temperature before casting the samples. The samples were cured in an oven at different temperatures and durations, for example, in the range of 70, 90, and 110ºC for 24 hours. Additionally, some samples were prepared and directly subjected to thermal curing. Strength tests were conducted to determine the optimal curing time, solution molarity ratio, water-to-binder ratio, and curing temperature. Detailed information, including material quantities and sample naming, is provided in the tables. This study primarily focuses on determining the optimal curing time and optimal curing temperature.

Table 2. Mixing ratios for AAS mortars.

Mixture Name	RHA (%)	BFS (%)	Molarity (NaOH)	Curing Temperature	Curing Time	Fiber Ratio	Fire resistance (ºC)
P0Y100	0	100	10M 12M 14M	70ºC 90ºC 110ºC	24 hours	Non-Fibrous Fibrous	200 400 600 800
P10Y90	5	95					
P20Y80	10	90					
P30Y70	15	85					
P40Y60	20	80					
P50Y50	25	75					
Total Parameters	**6**		**3**	**3**	**1**	**2**	**4**

2.3. Test Procedures

2.3.1. Compression and flexural testing

The AAS (alkali-activated slag) mortar mixtures were subjected to rigorous testing to evaluate their compressive and flexural strengths in accordance with TS EN 196-1 standards. For the compressive strength assessment, six 40×40×40 mm cement mortar specimens were prepared and tested using a hydraulic compression machine. The load was applied at a rate of (2400±200) N/s to ensure consistency and precision in the testing process. After the flexural strength determination, the fractured mortar prisms were carefully positioned between the compression testing plates, ensuring proper alignment to avoid any misalignment or skewing during the testing procedure. The compression test continued until the specimens fractured under the applied load.

To calculate the compressive strength of the mortar mixtures, the average result from the six specimens was taken, excluding any data points that deviated more than ±10% from the overall average. This exclusion criterion was employed to maintain the reliability and accuracy of the results. By following this procedure, a comprehensive evaluation of the compressive and flexural strength properties of the AAS mortar mixtures was achieved, providing valuable insight into the performance of the material under different loading conditions.

Figure 1. Compressive strength test.

2.3.2. Water absorption of AAS composite mortars

The water absorption characteristics of AAS composite mortar samples, with dimensions of 50×50×50 mm, were assessed for 28-day specimens following ASTM C642 standards (ASTM International, 2006) (Figure 2). The mortar samples were cured in a water tank with potable water for a specified period. After curing, the specimens were removed, dried using a towel, and weighed in a saturated surface-dry condition (B). Subsequently, the samples were placed in an oven at 110±5°C for 24 hours. After cooling to room temperature (20°C to 25°C), the samples were re-weighed (A). The water absorption rate was calculated using the formula [(B - A) / A] × 100.

Figure 2. Archimedes balance.

2.3.3. Chloride permeability of AAS composite mortars

AAS (alkali-activated slag) composite mortar specimens, which had been cured for 7 and 28 days, were tested for chloride ion permeability using the Rapid Chloride Permeability Test (RCPT) as per ASTM C1202 standards (ASTM International, 2012). These specimens were prepared by casting the mortar into Ø100×50 mm cylindrical molds (Figure 3), allowing for consistent and uniform specimen dimensions throughout the testing process. The chloride permeability test is designed to evaluate the ability of the mortar to resist the penetration of chloride ions, which is a key indicator of the material's durability, especially in environments exposed to de-icing salts or marine conditions. In this test, a voltage is applied across the specimen, and the rate at which chloride ions penetrate the material is measured. For the test, after the curing period, the specimens were subjected to the specified conditioning procedures as outlined in the ASTM C1202 standard. This typically involves placing the specimens in a testing apparatus where a voltage is applied across the specimen, with one side exposed to a chloride solution and the other side exposed to distilled water. The electrical current passed through the specimen is then measured, and the total charge passed during the test is calculated. The chloride ion permeability is evaluated based on the total charge passed through the specimen, expressed in coulombs. This value provides a direct assessment of the material's resistance to chloride penetration, where lower values indicate better resistance to chloride ion ingress, suggesting higher durability and suitability for use in environments prone to chloride exposure. By conducting this test on the AAS composite mortar specimens after 7 and 28 days of curing, the study aimed to assess the development of chloride permeability over time and the potential of the AAS mortars to perform well in terms of long-term durability.

Figure 3. Chlorine permeability of AAS composite mortars.

2.3.4. Ultrasonic transit time test

AAS composite mortar samples, with dimensions of 40×40×160 mm, were tested using an ultrasonic transit time method to assess their internal properties. Sound waves at a frequency of 55 kHz were transmitted through the samples using an ultrasonic device with a sensitivity of 0.1 μs. The transit times of the sound waves were measured according to ASTM C597 standards (ASTM International, 2003). These measurements were used to calculate the sound transit velocity, providing insights into the material's density and internal

structure. Based on the measured transit times (t, µs), the sound transit velocity (Vs, km/s) was calculated (Table 3).

Table 3. Practical evaluation of ultrasound transmission speeds.

Speed (km/s)	**≥4.5**	**3.5-4.5**	**3.0-3.5**	**2.0-3.0**	**≤2.0**
Concrete quality	Very Good	Good	Medium	Poor	Very Poor

2.3.5. High temperature experiment

The geopolymer mortar specimens, which had been cured for 28 days, were prepared for high-temperature testing to evaluate their thermal stability and performance under extreme conditions. For consistency, three replicate samples were taken from each batch of specimens. The high-temperature experiments were conducted using a high-temperature furnace, ensuring precise control over the heating process. The furnace was programmed to increase the temperature at a controlled rate of 5°C per minute, allowing for uniform heating and minimizing thermal shock to the specimens (Figure 4). During the test, each geopolymer mortar specimen was exposed to a series of target temperatures: 200°C, 400°C, 600°C, and 800°C. These temperatures were maintained for a period of one hour to simulate prolonged exposure to elevated temperatures. The specimens were carefully monitored to ensure that the desired temperature was consistently maintained throughout the exposure period. This step was crucial in assessing how the mortar would behave when subjected to varying degrees of heat, which could affect its mechanical properties, such as strength and stability. After the one-hour exposure to each target temperature, the furnace was turned off, and the specimens were allowed to cool gradually within the furnace. The cooling process was controlled to prevent any rapid temperature changes that could induce cracking or other forms of thermal damage to the mortar samples. The specimens were left to cool to ambient temperature naturally, without forced air circulation, to allow for a more uniform cooling rate and to observe any potential changes in the material properties as it returned to room temperature (Figure 5).

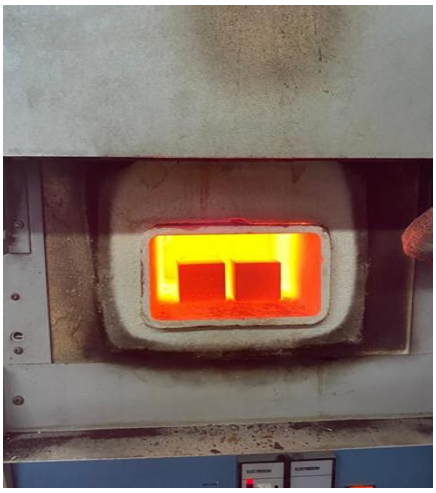

Figure 4. High temperature furnace.

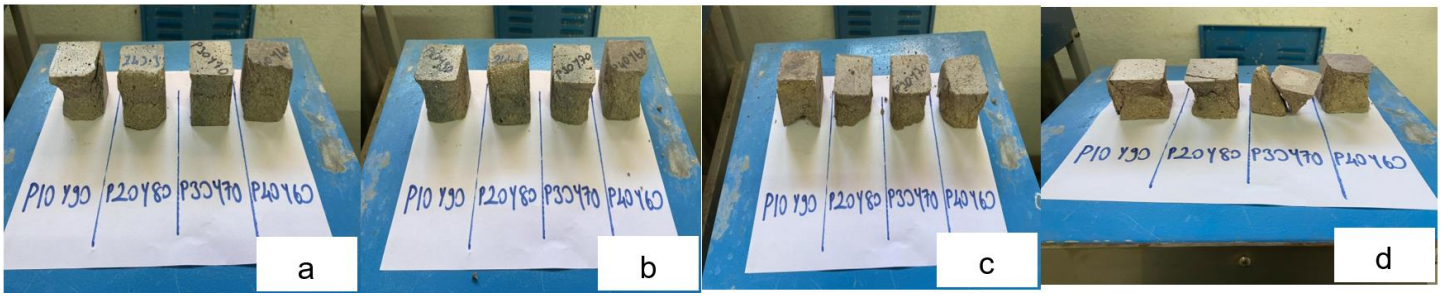

Figure 5. a) Room temperature b) 200°C c) 400°C d) 600°C compressive strength after sample image.

The condition of the specimens subjected to compressive testing at room temperature is shown in Figure 5. These specimens were examined through compressive tests conducted after exposure to temperatures of 200°C, 400°C, and 600°C. Beyond 800°C, it was observed that the specimens completely disintegrated at this stage. This highlights the significant impact of high temperatures on the specimens, particularly the pronounced loss of structural integrity at temperatures reaching 800°C.

3. Results and Discussion

This study aimed to evaluate the fire resistance of mixtures containing rice husk ash and BFS under different molarities and curing temperatures. The results obtained are as follows.

3.1. Molarity and Fire Resistance

Figure 6 presents the data showing the compressive strength values at varying molarities and temperatures. The study explores five molarity levels (8M, 10M, 12M, 14M) across three different temperatures (70°C, 90°C, 110°C). The findings

highlight a consistent trend: an increase in molarity results in higher compressive strength. Additionally, elevated temperatures generally contribute to improved compressive strength, with the most notable enhancement seen at 110°C. The maximum compressive strength is achieved at a molarity of 12M and a temperature of 110°C. All tests were performed using a 12M sodium hydroxide solution, with curing carried out at 110°C.

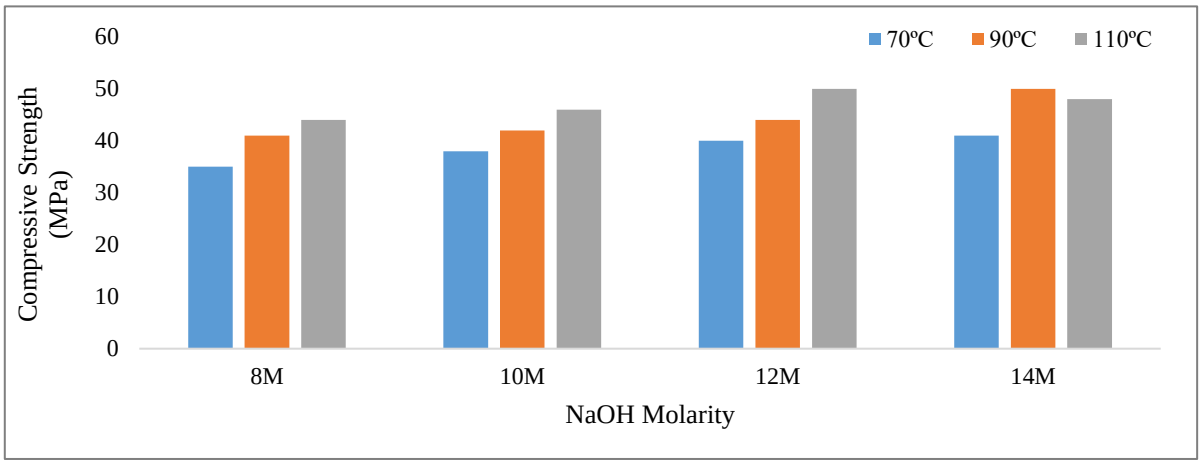

Figure 6. Compressive strength at different molarities and temperatures.

Similar findings are observed in the literature. Memon et al. (2013) reported that increasing the sodium hydroxide molarity from 8M to 14M enhanced compressive strength, with the highest strength achieved at 12M molarity and 70°C curing temperature. Mathew and Isaac (2020) demonstrated a 63% increase in compressive strength for laterized geopolymer concrete as NaOH molarity was increased. Moreover, Adam and Horianto (2014) found that curing at 120°C yielded the highest compressive strength compared to lower temperatures.

At specific temperatures, compressive strength generally increases with molarity. This finding confirms that sodium hydroxide molarity is a critical factor affecting fire resistance. Additionally, high compressive strength values observed at 110°C highlight the positive impact of elevated curing temperatures.

Curing with 12M molarity and 110°C provides the highest compressive strength. This suggests that a specific combination of molarity and temperature is most effective. All experiments were conducted using 12M sodium hydroxide molarity and cured at 110°C, emphasizing that the results are valid under these conditions. These findings clearly demonstrate how sodium hydroxide molarity and curing temperature influence compressive strength.

3.2. Compressive Strength

The results of 3, 7, 28 and 90-day compressive strength tests of AAS composite mortars are shown in Figure 7.

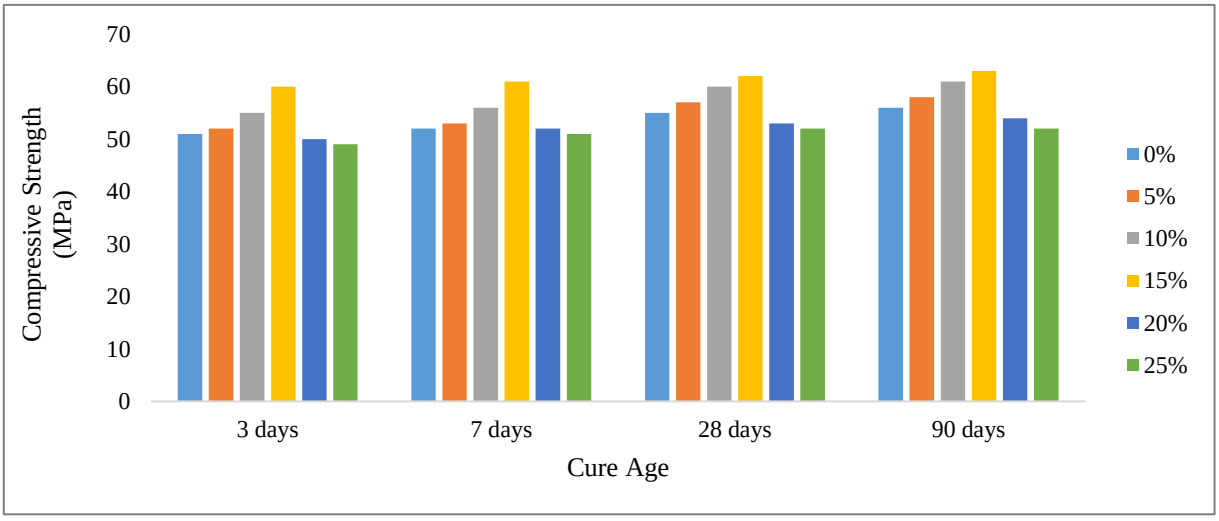

Figure 7. Compressive strength of rice husk ash substituted AAS specimens.

When analyzing the 3-day compressive strength data for Rice Husk Ash (RHA) blended concrete, it was observed that incorporating 5% RHA resulted in a 2% increase compared to the reference mix with 100% Ordinary Portland Cement (OPC). At 10% RHA, the increase rose to 7%, while 15% RHA achieved the highest gain at 17%. However, further increases in RHA content led to decreases in strength, with reductions of 2%, 4%, and 6% observed for 20%, 25%, and 30% RHA, respectively. Similarly, the 7-day strength data showed an optimal RHA content of 15%, which delivered an 18% improvement in strength compared to the reference. Lower proportions such as 5% and 10% RHA provided increases of 3% and 8%, respectively, while higher levels (20%, 25%, and 30%) exhibited diminishing returns, with the latter even showing a 3% reduction. These results consistently highlight that 15% RHA offers the best performance across both short and medium-term curing durations.

In line with these findings, long-term performance analysis over 90 days reaffirmed the superiority of the 15% RHA mix, maintaining the highest compressive strength over time. This underscores the potential of RHA to sustainably enhance the mechanical properties of concrete, particularly at an optimal replacement level of 15%. Supporting literature corroborates these outcomes. For instance, residual rice husk ash (RHA) from Uruguay and RHA produced by controlled burning in the USA were compared for their effects on concrete properties, including compressive strength up to 91 days, splitting tensile strength, and air permeability, using cement replacement levels of 10% and 20% and water/cement ratios of 0.50, 0.40, and 0.32 (De Sensale, 2006). Similarly, partially replacing cement with rice husk ash (RHA) improves concrete's compressive strength, reduces water permeability, and enhances workability, with optimal results achieved at 10% replacement using ultra-fine RHA particles. However, finer RHA positively affects hardened concrete's properties but negatively impacts the workability of fresh concrete (Givi et al., 2010). Lastly, Huang et al. (2017) emphasized the ability of RHA to refine the pore structure and enhance both compressive strength and impermeability in high-performance concrete.

This comprehensive evaluation concludes that using 15% RHA in concrete mixtures is a highly effective strategy for improving compressive strength across varied curing durations, offering significant sustainability benefits and long-term performance advantages.

3.3. Flexural Strength

The flexural strength test results of AAS composite mortars are presented in Figure 8.

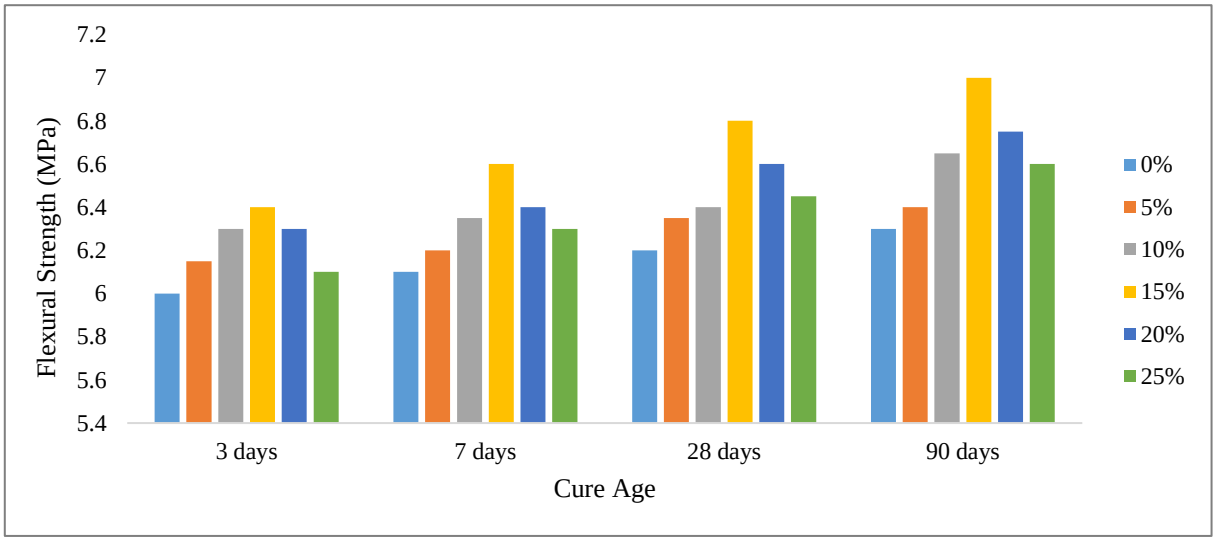

Figure 8. 7 and 28 day flexural strength results of AAS mortars.

The analysis of flexural strength for AAS mortars across curing periods of 3, 7, 28, and 90 days highlights the consistent performance of a 15% rice husk ash (RHA) mix. At 3 days, the 15% RHA mix achieved the highest strength (6.4 MPa), showcasing its short-term effectiveness. This trend continued over 7 and 28 days, with flexural strengths of 6.6 MPa and 6.8 MPa, respectively, affirming its medium- and long-term durability. By 90 days, the mix reached a peak flexural strength of 7.0 MPa, demonstrating sustained mechanical performance. These findings emphasize the efficiency of 15% RHA in enhancing the mechanical properties of mortars. Supporting studies, such as Jamil et al. (2016), Ali et al. (2021), and Huang et al. (2017), confirm that RHA improves flexural strength by leveraging pozzolanic activity and refining pore structure. In conclusion, incorporating 15% RHA is a sustainable and optimal strategy for boosting the flexural performance of AAS mortars.

3.4. Compressive Strength of Glass Fiber-Reinforced AAS Composites

Figure 9 illustrates the effects of glass fiber reinforcement on the compressive strength of AAS composites. The study evaluated combinations of different glass fiber ratios (0%, 0.50%, 1%, 2%, 4%) and samples containing 0% and 15% rice husk ash (RHA) replacements.

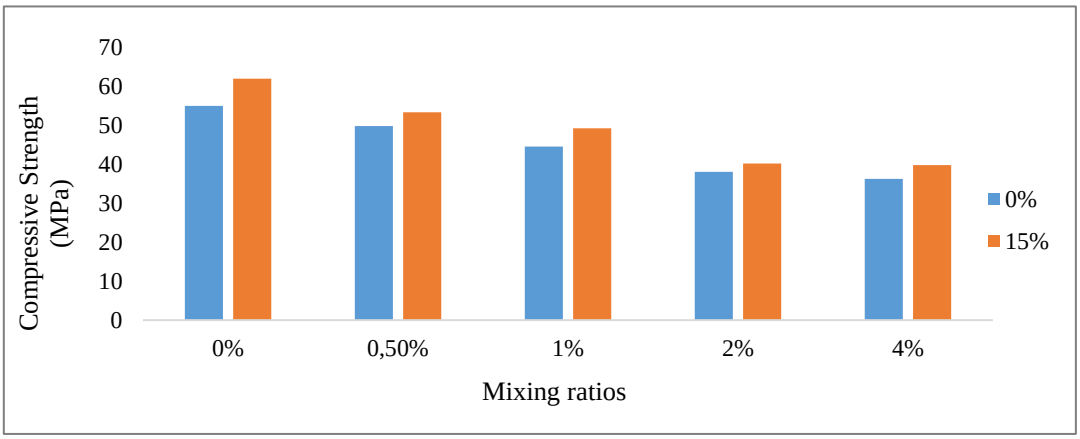

Figure 9. Compressive strength of glass fiber reinforced AAS samples.

The results indicate that increasing the glass fiber ratio generally improves compressive strength. For instance, in the absence of RHA (0%), higher glass fiber content significantly enhances compressive performance. Similarly, the inclusion of 15% RHA shows a synergistic effect with glass fibers, particularly at 2% fiber content, where the highest compressive strength was observed.

These findings align with existing research on fiber-reinforced composites. For example, Zheng et al. (2004) demonstrated that glass fiber reinforcement markedly improves compressive strength due to enhanced matrix-fiber interaction. Similarly, Kim and Crasto (1994) highlighted that unidirectional glass fiber composites exhibit superior compressive performance compared to random fiber arrangements.

In summary, the combination of glass fiber reinforcement and RHA optimizes the compressive strength of AAS composites, with 2% glass fiber and 15% RHA providing the best results. This demonstrates the importance of tailoring fiber and matrix proportions for enhanced mechanical performance.

3.5. Flexural Strength of Glass Fiber-Reinforced AAS Composites

Figure 10 illustrates the changes in flexural strength of AAS composites with varying glass fiber ratios. The results show that increasing the glass fiber content generally enhances flexural strength, with the highest strength observed at 1% glass fiber. However, a decline in flexural strength was noted at 2%, suggesting that excessive glass fiber content may negatively impact performance. This highlights the importance of identifying an optimal glass fiber ratio to avoid overuse, which can compromise structural integrity.

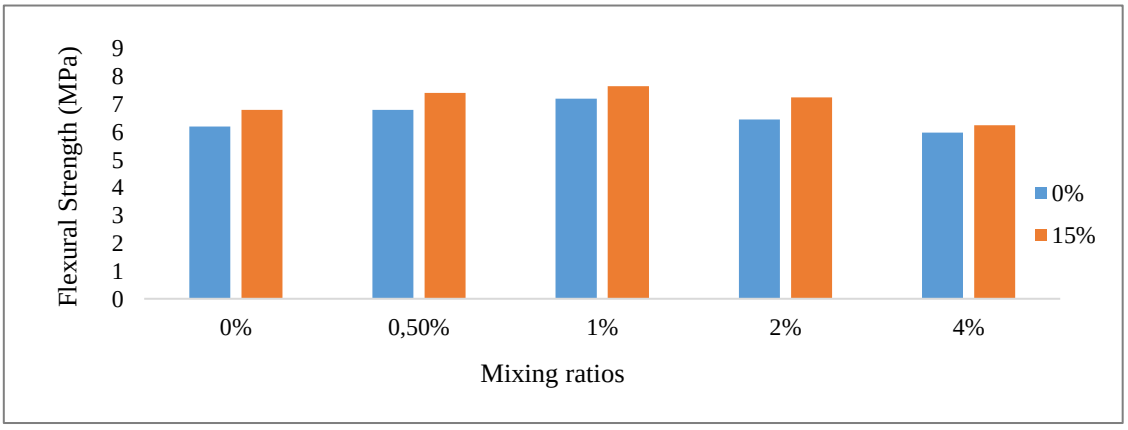

Figure 10. Flexural strength graph of glass fiber reinforced AAS samples.

Supporting studies align with these findings. Caixeta et al. (2015) demonstrated that incorporating glass fibers significantly improves the flexural strength of resin composites, emphasizing the reinforcement benefits provided by glass fibers. Similarly, Oberholzer et al. (2007) reported a 30% increase in flexural strength when glass fibers were added to composites, supporting the role of reinforcement in enhancing mechanical properties.

In conclusion, the addition of glass fibers positively impacts the flexural strength of AAS composites, with 1% being the optimal content. Proper calibration of fiber proportions is crucial for maximizing performance while preventing strength reductions due to overloading.

3.6. Water Absorption Variation

Figure 11 illustrates the water absorption change of AAS samples. The water absorption percentage of the samples increases relative to the "control sample" as the rice husk ash (RHA) content rises. This trend highlights the increasing impact of RHA on water absorption, which becomes more pronounced with higher RHA proportions. This behavior can be attributed to the unique properties of RHA, including its mineral composition, particle size, and reactivity, which influence water absorption characteristics.

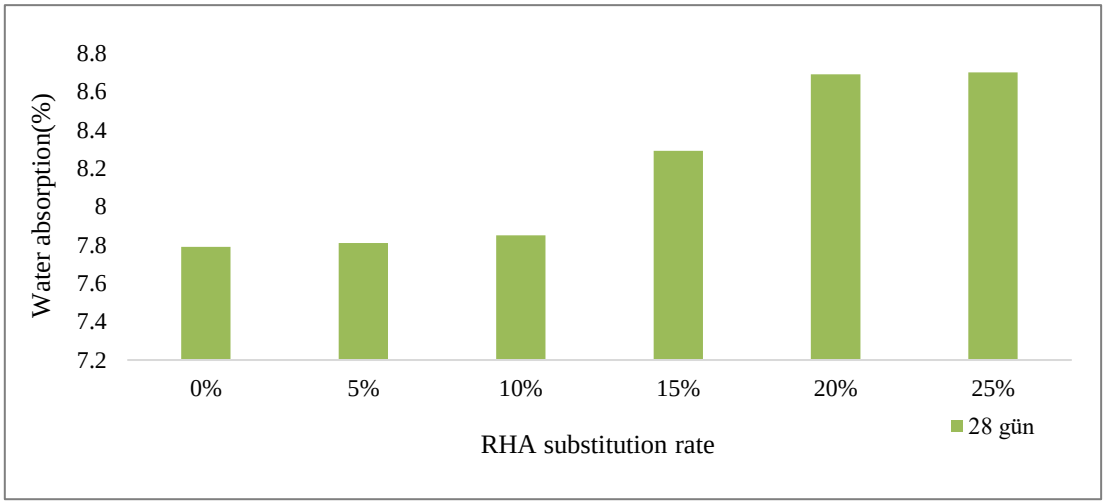

Figure 11. Water absorption change of AAS samples.

Supporting research confirms these observations. Huang et al. (2017) found that incorporating RHA into ultra-high-performance concrete reduced permeability due to the refined pore structure, enhancing impermeability at certain RHA levels. Similarly, Najigivi et al. (2012) demonstrated that ternary blends with RHA and nano-SiO_2 improved resistance to water absorption by forming a continuous, dense cement matrix, particularly at optimized replacement levels.

In summary, increasing RHA content significantly affects water absorption in concrete, with its mineral and structural characteristics playing a critical role. Optimizing the RHA content is essential to balancing enhanced durability with water absorption control.

3.7. Rapid Chloride Ion Permeability Test

The Rapid Chloride Ion Permeability Test (RCPT), conducted according to ASTM C1202 standards, is a critical method for evaluating the chloride ion permeability and durability of construction materials. In this study, the effects of rice husk ash (RHA) content on the durability properties of alkali-activated cement (AAC) composites were investigated. Samples with RHA at 0%, 5%, 10%, 15%, 20%, 25%, and 30% were tested for chloride ion permeability at 28 and 90 days (Figure 12).

The 28-day results showed significant impacts of RHA on the permeability and resistance properties of AAC composites. Samples without RHA (0% RHA) exhibited high permeability and low resistance. Adding 5% RHA significantly reduced permeability and increased resistance. Samples with 10% RHA showed moderate permeability and resistance, while 15% RHA provided the lowest permeability and highest resistance values. Samples with 20% and 25% RHA displayed moderate permeability and resistance, while 30% RHA increased permeability and reduced resistance (Huang et al., 2017).

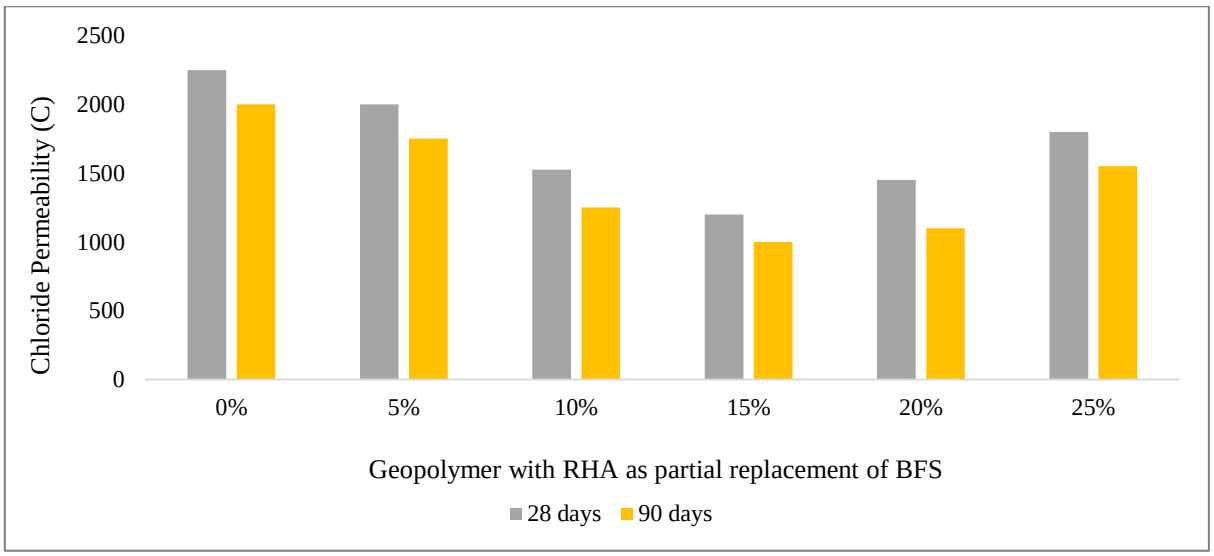

Figure 12. 28 and 90 day fast chloride ion permeability test results.

The 90-day results indicated that RHA reduces permeability and improves durability over time. AAC composites with 15% RHA achieved the lowest permeability and highest durability at 90 days, demonstrating excellent resistance to environmental effects (Prasittisopin & Trejo, 2017). As the water/cement ratio decreases in concrete, the reduction in chloride penetration is most effectively achieved with a 15% replacement of calcined rice husk ash (CRHA) or raw rice husk ash (RRHA) (De Sensale, 2010). Rice husk ash (RHA) has been shown to significantly enhance the durability and reduce the chloride ion permeability of AAC composites. De Sensale (2010) demonstrated that RHA, when used as a partial replacement for Portland cement, effectively improved the durability of cementitious materials by decreasing air permeability and chloride penetration, highlighting its suitability as a supplementary cementitious material. Similarly, Ramezanianpour et al. (2018) found that nano RHA enhanced the long-term durability of mortars by improving chloride resistance, compressive strength, and electrical resistivity, confirming its role in improving concrete properties in aggressive environments. These studies collectively highlight the effectiveness of RHA in improving the performance and longevity of concrete structures. In conclusion, the incorporation of RHA, a sustainable agricultural byproduct, optimizes the durability and chloride resistance of AAC composites while contributing to environmentally friendly construction practices.

Figure 13 presents the compressive strength of alkali-activated slag (AAS) composites under high-temperature effects.

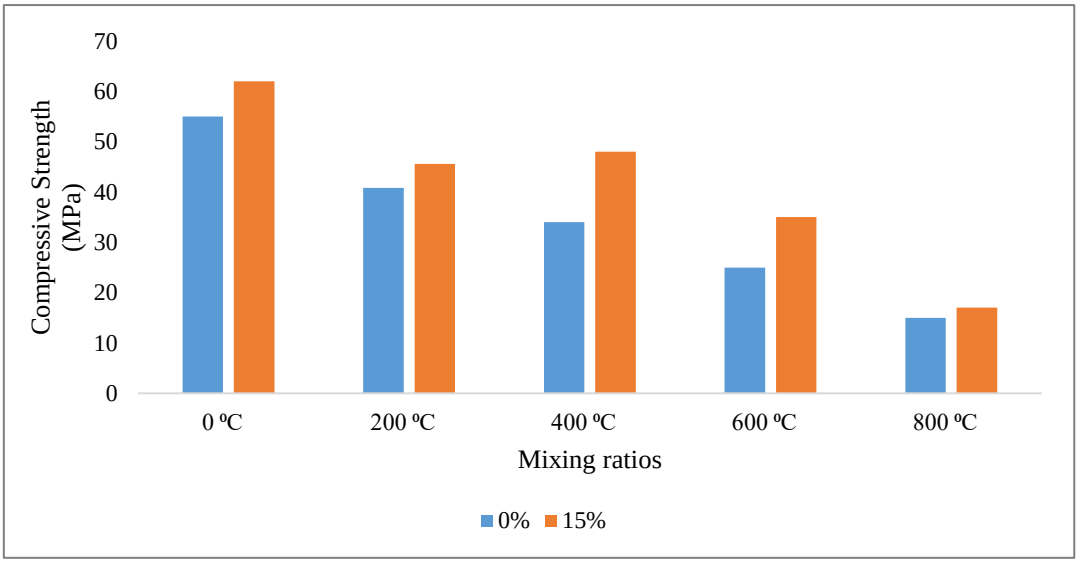

Figure 13. Compressive strength under high temperature effect.

The evaluation focuses on the effects of a 15% rice husk ash (RHA) addition on the 28-day compressive strength of the composites, subjected to varying temperature conditions of 200°C, 400°C, 600°C, and 800°C. The results indicated that RHA addition significantly enhanced compressive strength at 400°C and 600°C, demonstrating improved thermal resistance and mechanical performance. However, at 200°C and 800°C, the influence of RHA was more limited, with no significant differences observed at the higher temperature. Based on recent studies, Rice Husk Ash (RHA) is an effective alternative material for producing alkali-activated concrete (AAC), showing significant environmental benefits and durability. RHA, which is rich in silica, plays a key role in enhancing geopolymerization, improving mechanical properties such as compressive strength, and reducing permeability. Research indicates that when used in combination with other materials like fly ash or steel slag, RHA can significantly enhance concrete's ability to resist chemical attacks, such as from chloride or sulfuric acid exposure, making it highly suitable for harsh environments like marine settings Incorporating RHA into construction materials not only supports sustainable practices by reducing agricultural waste but also helps in addressing the growing demand for durable, high-performance concrete. Studies have shown that AAC made with RHA has comparable or even superior performance to traditional Portland Cement in terms of both durability and environmental impact (Alahmari et al., 2023; Barragán-Ramírez et al., 2024).

4. Conclusion

This study investigated the effects of sodium hydroxide molarity, curing temperature, rice husk ash (RHA) addition, and glass fiber reinforcement on the mechanical properties and durability of alkali-activated slag (AAS) composites. The findings demonstrate that increasing the molarity of sodium hydroxide solutions enhances compressive strength, with the most effective conditions observed at 12M molarity and 110°C curing temperature. These parameters promoted optimal geopolymerization, resulting in superior mechanical performance.

The incorporation of RHA significantly improved the flexural strength of AAS composites, with the highest strength achieved at a 15% RHA addition. This optimal mix also maintained its high strength over long-term use while effectively reducing chloride ion permeability, highlighting its suitability for applications requiring enhanced durability. Furthermore, under elevated temperatures, particularly at 400°C and 600°C, the addition of RHA further increased compressive strength, underscoring its thermal stability benefits.

Glass fiber reinforcement also contributed positively to both flexural and compressive strength. However, a decline in performance was observed at 2% glass fiber content, emphasizing the necessity of carefully selecting the optimal fiber dosage for maximizing mechanical benefits.

In summary, the synergistic effects of RHA and glass fiber additions were found to be effective strategies for enhancing the mechanical properties and durability of AAS composites. These findings underline the potential of incorporating RHA and glass fibers in concrete designs to improve environmental sustainability and long-term structural performance, offering valuable insights for future construction material innovations.

Acknowledgment

This research was supported under the scope of the Scientific and Technological Research Council of Turkey (TÜBİTAK) 2209-A University Students Research Projects Support Program, 2nd term of 2022, with project number 1919B012213936.

Conflict of Interest

The authors declare that they have no conflict of interest.

References

Adam, A. A., & Horianto, X. X. X. (2014). The effect of temperature and duration of curing on the strength of fly ash based geopolymer mortar. *Procedia Engineering*, *95*, 410-414. https://doi.org/10.1016/j.proeng.2014.12.199

Alahmari, T. S., Abdalla, T. A., & Rihan, M. A. M. (2023). Review of recent developments regarding the durability performance of eco-friendly geopolymer concrete. *Buildings*, *13*(12), 3033. https://doi.org/10.3390/buildings13123033

Ali, T., Saand, A., Bangwar, D. K., Buller, A. S., & Ahmed, Z. (2021). Mechanical and durability properties of aerated concrete incorporating rice husk ash (RHA) as partial replacement of cement. *Crystals*, *11*(6), 604. https://doi.org/10.3390/cryst11060604

Amran, M., Al-Fakih, A., Chu, S. H., Fediuk, R., Haruna, S., Azevedo, A., & Vatin, N. (2021). Long-term durability properties of geopolymer concrete: An in-depth review. *Case Studies in Construction Materials*, *15*, e00661. https://doi.org/10.1016/J.CSCM.2021.E00661

Arularasi, V., Thamilselvi, P., Avudaiappan, S., Saavedra Flores, E. I., Amran, M., Fediuk, R., Vatin, N., & Karelina, M. (2021). Rheological behavior and strength characteristics of cement paste and mortar with fly ash and GGBS admixtures. *Sustainability*, *13*(17), 9600. https://doi.org/10.3390/su13179600

ASTM International. (2002). *ASTM C109/C109M-02: Standard test method for compressive strength of*

hydraulic cement mortars (using 2-in. or [50-mm] cube specimens). https://cdn.standards.iteh.ai/samples/18736/1886184914c84503a7c2e10762f27381/ASTM-C109-C109M-02.pdf

ASTM International. (2003). *ASTM C597-16: Standard test method for pulse velocity through concrete*. https://cdn.standards.iteh.ai/samples/94392/666ac7ceb8354eefaab00c9ca74b2b1f/ASTM-C597-16.pdf

ASTM International. (2006). *ASTM C642-06: Standard test method for density, absorption, and voids in hardened concrete*. https://cdn.standards.iteh.ai/samples/48531/2dda55d49db741ebad1d409bacd4f0f8/ASTM-C642-06.pdf

ASTM International. (2012). *ASTM C1202: Standard test method for electrical indication of concrete's ability to resist chloride ion penetration*. https://cdn.standards.iteh.ai/samples/79981/7d0c052c7f4c4e9f9d037138c568a532/ASTM-C1202-12.pdf

Barragán-Ramírez, R., González-Hernández, A., Bautista-Ruiz, J., Ospina, M., & Aperador Chaparro, W. (2024). Enhancing concrete durability and strength with fly ash, steel slag, and rice husk ash for marine environments. *Materials*, *17*(12), 3001. https://doi.org/10.3390/ma17123001

Caixeta, R. V., Guiraldo, R. D., Berger, S. B., Kaneshima, E. N., Júnior, É. M. F., Drumond, A. C., Júnior, A. G., & Lopes, M. B. (2015). Influence of glass-fiber reinforcement on the flexural strength of different resin composites. *Applied Adhesion Science*, *3*, 24. https://doi.org/10.1186/s40563-015-0053-1

Colangelo, F., Farina, I., Travaglioni, M., Salzano, C., Cioffi, R., & Petrillo, A. (2021). Eco-efficient industrial waste recycling for the manufacturing of fibre reinforced innovative geopolymer mortars: Integrated waste management and green product development through LCA. *Journal of Cleaner Production*, *312*, 127777. https://doi.org/10.1016/J.JCLEPRO.2021.127777

De Sensale, G. R. (2006). Strength development of concrete with rice-husk ash. *Cement and Concrete Composites*, *28*(2), 158-160. https://doi.org/10.1016/j.cemconcomp.2005.09.005

De Sensale, G. R. (2010). Effect of rice-husk ash on durability of cementitious materials. *Cement and Concrete Composites*, *32*(9), 718-725. https://doi.org/10.1016/j.cemconcomp.2010.07.008

Givi, A. N., Rashid, S. A., Aziz, F. N. A., & Salleh, M. A. M. (2010). Assessment of the effects of rice husk ash particle size on strength, water permeability and workability of binary blended concrete. *Construction and Building Materials*, *24*(11), 2145-2150. https://doi.org/10.1016/j.conbuildmat.2010.04.045

Habert, G., D'Espino De Lacaillerie, J. B., & Roussel, N. (2011). An environmental evaluation of geopolymer-based concrete production: Reviewing current research trends. *Journal of Cleaner Production*, *19*(11), 1229-1238. https://doi.org/10.1016/J.JCLEPRO.2011.03.012

Hardjito, D., & Rangan, B. V. (2005). *Development and properties of low-calcium fly ash-based geopolymer concrete*. https://espace.curtin.edu.au/bitstream/handle/20.500.11937/5594/19327_downloaded_stream_419.pdf?sequence=2

Hossain, S. S., Roy, P. K., & Bae, C. J. (2021). Utilization of waste rice husk ash for sustainable geopolymer: A review. *Construction and Building Materials*, *310*, 125218. https://doi.org/10.1016/J.CONBUILDMAT.2021.125218

Huang, H., Gao, X., Wang, H., & Ye, H. (2017). Influence of rice husk ash on strength and permeability of ultra-high performance concrete. *Construction and Building Materials*, *149*, 621-628. https://doi.org/10.1016/j.conbuildmat.2017.05.155

Hwang, C. L., & Huynh, T. P. (2015). Effect of alkali-activator and rice husk ash content on strength development of fly ash and residual rice husk ash-based geopolymers. *Construction and Building Materials*, *101*(Part 1), 1-9. https://doi.org/10.1016/J.CONBUILDMAT.2015.10.025

Jamil, M., Khan, M. N. N., Karim, M. R., Kaish, A. B. M. A., & Zain, M. F. M. (2016). Physical and chemical contributions of Rice Husk Ash on the properties of mortar. *Construction and Building Materials*, *128*, 185-198. https://doi.org/10.1016/j.conbuildmat.2016.10.029

Kim, R. Y., & Crasto, A. S. (1994). Longitudinal compression strength of glass fiber-reinforced composites. *Journal of Reinforced Plastics and Composites*, *13*(4), 326-338. https://doi.org/10.1177/073168449401300404

Kim, Y. Y., Lee, B. J., Saraswathy, V., & Kwon, S. J. (2014). Strength and durability performance of alkali-activated rice husk ash geopolymer mortar. *Scientific World Journal*, *2014*(1), 209584. https://doi.org/10.1155/2014/209584

Manzoor, T., Bhat, J. A., & Shah, A. H. (2024). Performance of geopolymer concrete at elevated temperature− A critical review. *Construction and Building*

Materials, *420*, 135578. https://doi.org/10.1016/j.conbuildmat.2024.135578

Mathew, G., & Issac, B. M. (2020). Effect of molarity of sodium hydroxide on the aluminosilicate content in laterite aggregate of laterised geopolymer concrete. *Journal of Building Engineering*, *32*, 101486. https://doi.org/10.1016/j.jobe.2020.101486

Mathew, G., & Joseph, B. (2018). Flexural behaviour of geopolymer concrete beams exposed to elevated temperatures. *Journal of Building Engineering*, *15*, 311-317. https://doi.org/10.1016/J.JOBE.2017.09.009

Mehta, A., & Siddique, R. (2018). Sustainable geopolymer concrete using ground granulated blast furnace slag and rice husk ash: Strength and permeability properties. *Journal of Cleaner Production*, *205*, 49-57. https://doi.org/10.1016/J.JCLEPRO.2018.08.313

Memon, F. A., Nuruddin, M. F., Khan, S., Shafiq, N., & Ayub, T. (2013). Effect of sodium hydroxide concentration on fresh properties and compressive strength of self-compacting geopolymer concrete. *Journal of Engineering Science and Technology*, *8*(1), 44-56.

Najigivi, A., Abdul Rashid, S., Nora A. Aziz, F., & Mohd Salleh, M. A. (2012). Water absorption control of ternary blended concrete with nano-SiO 2 in presence of rice husk ash. *Materials and Structures*, *45*, 1007-1017. https://doi.org/10.1617/s11527-011-9813-y

Oberholzer, T. G., Du Preez, I. C., Lombard, R., & Pitout, E. (2007). Effect of woven glass fibre reinforcement on the flexural strength of composites: Scientific. *South African Dental Journal*, *62*(9), 386-389.

Prasittisopin, L., & Trejo, D. (2017). Performance characteristics of blended cementitious systems incorporating chemically transformed rice husk Ash. *Advances in Civil Engineering Materials*, *6*(1), 17-35. https://doi.org/10.1520/ACEM20160001

Ramezanianpour, A., Balapour, M., & Hajibandeh, E. (2018). Effect of nano rice husk ash against penetration of chloride ions in mortars. *AUT Journal of Civil Engineering*, *2*(1), 97-102. https://doi.org/10.22060/ajce.2017.12387.5203

Sarker, P. K., Haque, R., & Ramgolam, K. V. (2013). Fracture behaviour of heat cured fly ash based geopolymer concrete. *Materials & Design*, *44*, 580-586. https://doi.org/10.1016/j.matdes.2012.08.005

Singh, N. B., & Middendorf, B. (2020). Geopolymers as an alternative to Portland cement: An overview. *Construction and Building Materials*, *237*, 117455. https://doi.org/10.1016/j.conbuildmat.2019.117455

Sturm, P., Gluth, G. J. G., Brouwers, H. J. H., & Kühne, H. C. (2016). Synthesizing one-part geopolymers from rice husk ash. *Construction and Building Materials*, *124*, 961-966. https://doi.org/10.1016/j.conbuildmat.2016.08.017

Zhan, J., Liu, W., Wu, F., Li, Z., & Wang, C. (2018). Life cycle energy consumption and greenhouse gas emissions of urban residential buildings in Guangzhou city. *Journal of Cleaner Production*, *194*, 318-326. https://doi.org/10.1016/j.jclepro.2018.05.124

Zheng, Y., Ning, R., & Zheng, Y. (2004). Glass fiber-reinforced polymer composites of high compressive strength. *Journal of Reinforced Plastics and Composites*, *23*(16), 1729-1740. https://doi.org/10.1177/0731684404040127

http://jaasci.com
JOURNAL OF ADVANCED APPLIED SCIENCES
e-ISSN: 2979-9759
https://prensip.gen.tr

RESEARCH ARTICLE

X-Ray Radiation Responses of 4H-SiC MOS with Eu_2O_3/SiO_2 Dual Dielectric

Harem Saleh[1] • Şenol Kaya[2,4] • Yalçın Kalkan[2,4] • Rıfkı Terzioğlu[3,4] • Cabir Terzioğlu[1,4]✉

[1]Bolu Abant İzzet Baysal University, Department of Physics, Bolu/Türkiye
[2]Bolu Abant İzzet Baysal University, Vocational School of Health Services, Bolu/Türkiye
[3]Bolu Abant İzzet Baysal University, Department of Electrical and Electronics Engineering, Bolu/Türkiye
[4]Bolu Abant İzzet Baysal University, Center of Nuclear Radiation Detectors Research and Applications, Bolu/Türkiye

ARTICLE INFO

Article History
Received: 22.11.2024
Accepted: 23.12.2024
First Published: 30.12.2024

Keywords
Eu_2O_3
High-k materials
MOS irradiation
SiC substrates
X-ray diffraction

ABSTRACT

This study examines the effects of X-ray irradiation on the structural and electrical properties of Eu_2O_3 dielectric thin films deposited on SiC substrates. The films were exposed to varying radiation durations, and their structural changes were analyzed using X-ray diffraction (XRD), while electrical properties were evaluated through capacitance-voltage (C-V) and conductance-voltage (G/ω-V) measurements. The results revealed that increased radiation exposure led to an increase in crystalline size and lattice strain, attributed to local heating and atomic rearrangements caused by radiation. Electrical analysis showed slight shifts in flat band and mid-gap voltages due to radiation-induced defects, which influenced charge trapping behavior. Despite the observed defects, the dielectric material exhibited stable electrical performance under the tested radiation conditions, indicating its potential for radiation-tolerant electronic devices. These findings highlight the applicability of Eu_2O_3 as a high-k dielectric material for advanced electronic devices operating in radiation-harsh environments.

Please cite this paper as follows:

Saleh, H., Kaya, Ş., Kalkan, Y., Terzioğlu, R., & Terzioğlu, C. (2024). X-ray radiation responses of 4H-SiC MOS with Eu_2O_3/SiO_2 dual dielectric. *Journal of Advanced Applied Sciences, 3*(2), 79-84. https://doi.org/10.61326/jaasci.v3i2.313

1. Introduction

Rare earth materials with a high dielectric constant, withstand high temperatures and radiation damage, and with an oxide thickness equivalent to SiO_2, which greatly reduces the leakage current, are excellent for replacing SiO_2 in the structure of devices based on the metal-oxide-semiconductor (MOS) structure (Bera & Maiti, 2007; Kahraman & Yilmaz, 2018; Manikanthababu et al., 2015). Radiation in general affects well or leads to the failure or deterioration of devices based on SiO_2 without a second insulator (Manikanthababu et al., 2015). Knowing that MOS structures are present in the basics of many of the electronic devices that currently exist and are based on semiconductors such as solar cells, transistors and circuits. Integrated and due to the technological importance of these devices, it is necessary to study their electrical, optical and chemical properties (Kaya et al., 2015a).

✉ Correspondence
E-mail address: terzioglu_c@ibu.edu.tr

Radiation particles can deteriorate the performance of electronic devices, and oxides are highly susceptible to radiation damage. The two main types of radiation-induced charges are the charge trapped in the oxide and the charge trapped at the Si/SiO_2 interface (Karataş et al., 2009; Kaya et al., 2015b; Yilmaz et al., 2008). The presence of the interfacial layer in the MOS device strengthens the structure of the device and is more sensitive to radiation (Kaya et al., 2015b; Wilk et al., 2001). The main components of many electronic devices are insulators and oxides, and radiation (at high doses) can lead to a significant accumulation of charges in these components and thus lead to the failure of the devices. The interface states are considered as one of the most important parameters, in addition to the role of the insulating layer formed between the oxide and the semiconductor of the manufactured structures. Therefore, the interface layer and interface states cannot be ignored, which could lead to errors in the characteristics of the MOS device, knowing that the interface layer has an important role in determining the density of interface states. It is possible to control the electrical properties by the interface states and interlayer (Karadeniz et al., 2007; Laha et al., 2011).

Radiation causes defects such as phase transformation, displacement of atoms or vacancies and voids in the MOS structure (Jiang, 2015). The field generated by the action of radiation leads to the breaking of chemical bonds and produces defects as well (Shi et al., 2019). These defects caused by radiation may affect the response MOS to radiation (Zhou et al., 2005). It has high electrons and a high breakdown electric field (Li et al., 2023). The use of a high-k material is to improve the performance of device.

Here, we present the influence of irradiation exposure time (X- radiation) on the structural and electrical properties of Eu_2O_3 films deposited on SiC substrates. To perform the purpose of this study, $Al/(Eu_2O_3/SiO_2/n\text{-}SiC)/Ag$ MOS capacitors were fabricated via e-beam deposition method. To analyze structural properties of the irradiated and non-irradiated capacitors, XRD measurements were performed. Finally, to investigate the effect of irradiation effect on the electrical properties of capacitors, capacitance and conductance as a function of voltage at different radiation exposer time measurements were carried out. Therefore, it is important to study the effect of radiation on these materials.

2. Materials and Methods

The n-type 4H-SiC wafer was cleaned of impurities by the Radio Corporation of America (RCA) standard cleaning process to fabricate the $Al/(Eu_2O_3/SiO_2/n\text{-}SiC)$ MOS capacitors. After the RCA cleaning process, the SiC substrate was dried with 8N purity. The dried substrate was then placed in a diffusion oven at a temperature of 900°C for growing SiO_2 layer by dry oxidation method. Pure oxygen gas was then introduced into the environment to form SiO_2 with a thickness of about 5 nm. After deposition of the interfacial transition layer, a 120 nm thick Eu_2O_3 layer was coated on the substrates using an electron beam evaporation system. They were annealed for 120 minutes at 800°C under the nitrogen atmosphere. The thin films produced after this process were divided into several parts, some without irradiation (virgin), and some of them were exposed to radiation at a fixed dose of 50 keV and a tube current of 80 μA, and the distance between the sample and the X-ray tube was 5 mm for different periods of time (2 hours, 4 hours, and 6 hours). The films were analyzed by a Rigaku X-ray diffraction (XRD) instrument with a CuKα characteristic X-ray wavelength of 1.5406 Å, and the range 2θ was between 10° and 70°. Aluminum (Al) metal (99.99% purity) was then deposited on the front surface of all the samples using a sputtering system with a 1 mm diameter circular shadow mask. The whole back side coated with silver to collect signals. Electrical measurements of C–V and G/ω–V were performed for different time periods of 300 s, 600 s, 900 s, 2100 s, 2700 s, 3100 s using a Keithley 4200-SCS parameter analyzer with a frequency of 100 kHz at room temperature. The effect of radiation exposure time on the electrical and structural properties were investigated.

3. Results and Discussion

Figure 1 shows the XRD patterns of Eu_2O_3 thin films before and after x-rays exposure to the film. The effects of x-irradiation on the crystalline structure of Eu_2O_3 films were studied by analyzing the XRD patterns. The peaks were indexed via the International Centre for Diffraction Data (ICDD) database, demonstrating a strong correlation with 65-3182 ICDD card number which is the cubic phase of Eu_2O_3 with (222) preferred orientation. It was observed that the (222) peak of intensity increased with increasing exposure time while the peak shifted to the higher angles. In a perfect crystal, when there is no internal strain associated with d-spacing, the atoms have a regular structure, and this structure is consistent with the theoretically predicted d_0 plane spacing. However, when homogeneous strain occurs in the crystal structure, the distances between atoms expand, and the distance between the reflecting planes becomes larger than d_0. In this case, the diffraction lines in the XRD pattern shift to lower angles because the larger d-spacing is associated with a lower diffraction angle. In case of non-uniform strain, the atoms in the crystal may compress at different rates. This leads to a broadening of the XRD peaks, as different regions of the crystal exhibit varying levels of strain. On the other hand, an increase in peak intensity was observed along with a shift to higher angles, that is, an increment in crystallite size. The lattice strain values were calculated to be 2.78, 2.72, 2.94 and 3.08×10^{-3} for the unirradiated, irradiated for 2h, irradiated for 4h and irradiated for 6h samples, respectively. The lattice strain values increased with the increase in exposure time as shown in Table 1. The radiation energy is able to displace the individual atoms

of the material from their position by transferring kinetic energy to them. Compton scattering occurs, oxygen vacancies are formed (after breaking bonds), the formation of an interstitial defect, and the development of the granular structure, all of which affect the changes occurring in the structure of the device, and the displacement of the peaks in the XRD patterns are also related to the increase and decrease in crystallite size (Baydogan et al., 2013; Doyle, 2014; Kaleji et al., 2012; Kozlovskiy et al., 2022; Liu et al., 2021; Mazzolini et al., 2016; Subramanian & Wang, 2012; Tracy et al., 2014; Zhang et al., 2021).

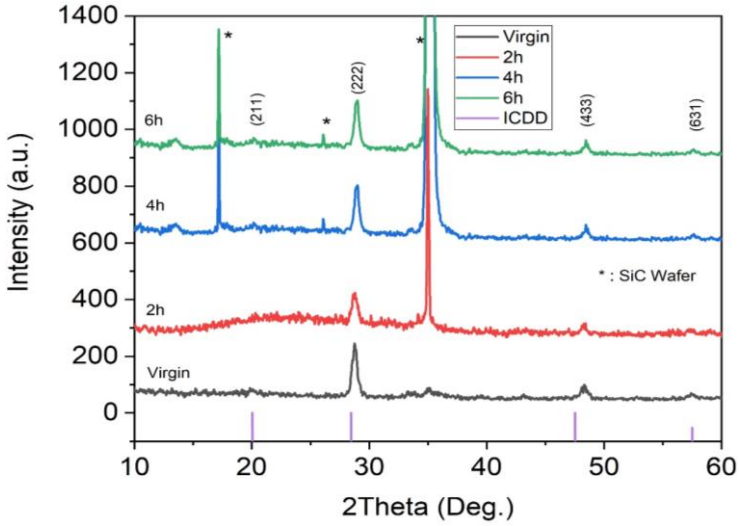

Figure 1. X-ray diffraction patterns of irradiated and unirradiated Eu_2O_3 dielectric thin films.

Table 1. Some structure parameters of Eu_2O_3 MOS at different exposure time of dose radiation.

Exposure time	2θ (degrees)	Crystallite size (Å)	Lattice strain x 10^{-3}
Virgin	29.376	159.62	2.778
2 hours	29.320	163.61	2.720
4 hours	29.530	205.43	2.942
6 hours	29.550	195.62	3.080

In addition, the crystallite sizes were calculated via the Scherer relationship using the (222) peak and tabulated in Table 1. The crystallite size was found to be 159.62, 163.61, 205.43 and 195.62 Å for the unirradiated, irradiated for 2h, irradiated for 4h and irradiated for 6h samples, respectively (Mozia, 2008; Mozia et al., 2009). In addition to ionization and atomic displacement that occur after radiation, radiation also causes a lattice vibration during the transfer of kinetic energy to the points of the lattice and thus leads to local heating. This heating leads to the displacement of atoms and their gathering into a larger mass. The reason for the increase in crystallite size is due to the presence of local heating of the atoms (Kaya et al., 2019; Laha et al., 2012). As a conclusion, both the crystallite size and lattice strain increased with increasing the exposure time, which is expected result.

To study the influence of radiation on the electrical properties of Eu_2O_3 films, the C-V, G-V measurements were carried out on the unirradiated and irradiated samples using an x-ray radiation source with a 50 kV energy for different exposure time periods of 300 s, 600 s, 900 s, 2100 s, 2700 s, 3100 s. The measured C-V characteristics are shown in Figure 2. Upon examining the overall C-V curve, it was observed that no abnormal degradation occurred in the structure. Ionizing radiations, such as gamma and x-rays, produce defects, interface trap- and oxide trap-charges in MOS capacitors (Ma & Dressendorfer, 1989). The interface states may act like an additional capacitance depending on whether they can follow applied voltages or not (Kaya & Yilmaz, 2015). The interface states generated by irradiation may contribute to the measured capacitance and thus, the total capacitance values increased. Capacitance changes may be a result of the voltage signal tracking these trap sites. Furthermore, when the curves were enlarged, it was observed that the flat band (V_{fb}) and midgap (V_{mg}) voltage values shifted in bi-directions due to radiation exposure. The additional exposure time periods also lead to breaking the bonds in the structure, and thus, new defects or trap centers appear and leads to confine a larger number of charges to these centers and thus lead to an increase in the flat band voltage shift (Kaya & Yilmaz, 2018). However, in some cases the broken or non-stoichiometric bonds can be neutralized by irradiation exposes (Kaya et al., 2018). Shifts towards zero volts in V_{fb} and V_{mg} indicate that positive charges are predominantly trapped within the structure (Kaya & Yilmaz,

2015, 2018; Kaya et al., 2018). Shifts towards high voltage values at certain dose levels may suggest that the trapped positive charges have been neutralized or that some trap regions created by radiation are trapping negative charges.

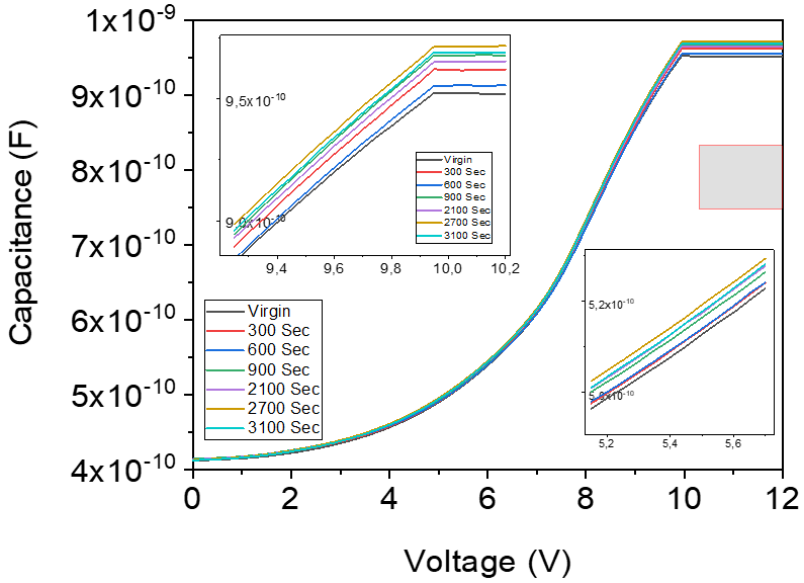

Figure 2. C-V curves showing the radiation response of a Eu_2O_3 dielectric thin film.

To determine the behavior of the interfacial states under radiation, conductivity measurements were performed, and after correcting for series resistance, the results are shown in Figure 3. As seen from this, the peak of the conductivity value increased and decreased based on the radiation dose. Since the conductivity measurement is influenced by the interaction of interface traps, it can be concluded that the trap densities change with radiation exposure. The density of interface states D_{it} was calculated using well-kwon Hill-Coleman method (Hill & Coleman, 1980). Based on the calculations, the interface trap density before and after radiation was determined to be 1.506 $x10^{12}$, 1.490 $x10^{12}$, 1.481 $x10^{12}$, 1.486 $x10^{12}$, 1.501 $x10^{12}$, 1.558 $x10^{12}$, 1.507$x10^{12}$ $(eV.cm^2)^{-1}$ for virgin, 300 sec, 600 sec, 900 sec, 2100 sec, 2700 sec, and 3100 sec exposure times, respectively. Similar to the radiation-induced oxide trapped charge density in capacitance, the interface trap densities are either neutralized or generated depending on the exposure doses. For dielectric materials to be usable in radiation detection, it is expected that one-way voltage shift behavior will emerge with increasing radiation dose. The observed behavior during the applied radiation dose suggests that the material has low dosimetric properties. However, it is important to note that this behavior may develop at higher dose ranges. The measurements indicated that the structure under investigation exhibited electrically stable characteristics under the applied radiation field. This feature highlights its potential for producing stable electronic devices in challenging radiation environments.

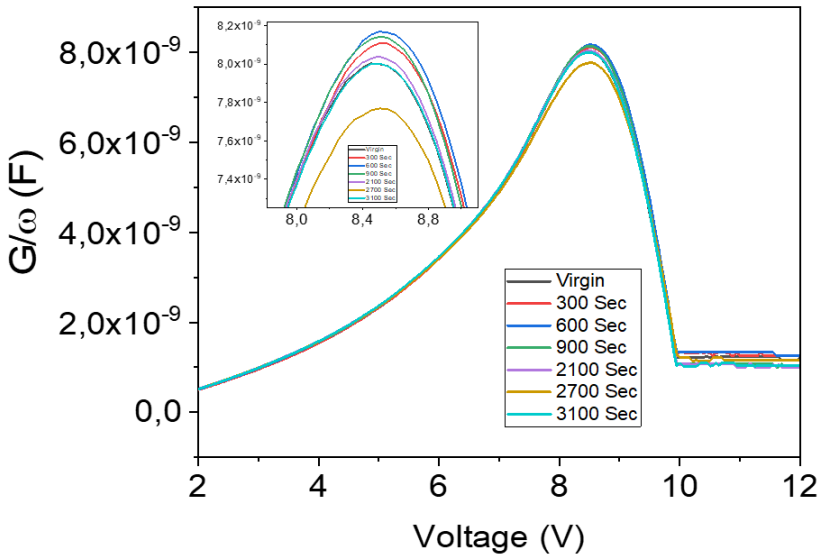

Figure 3. G/ω-V curves showing the radiation response of a Eu_2O_3 dielectric thin film.

4. Conclusion

The study investigated the effects of X-ray irradiation on the structural and electrical properties of Eu_2O_3 dielectric thin films deposited on SiC substrates. The findings demonstrated some modifications in crystallite size, lattice strain, and electrical behavior as a function of radiation exposure time. Structural analysis through X-ray diffraction revealed that increasing radiation exposure resulted in an increase in the crystallite size and lattice strain. These changes were attributed to local heating and structural rearrangements induced by radiation, confirming the impact of radiation on the structural integrity of Eu_2O_3 films. Electrical characterization via capacitance-voltage (C-V) and conductance-voltage (G/ω-V) measurements demonstrated that radiation-induced defects caused a slight alteration in the interface states and charge trapping behavior. Shifts in flat band and mid-gap voltages were observed, correlating with the formation of traps and the redistribution of charges under radiation. Despite the introduction of defects, the Eu_2O_3 dielectric exhibited stable electrical characteristics, demonstrating its resilience under the exposed radiation conditions. Furthermore, the material's response suggested limited dosimetric potential within the tested dose range. However, its structural and electrical stability under radiation highlights its viability for applications in radiation-tolerant devices. These findings underscore the importance of Eu_2O_3 as a high-k dielectric material for advanced electronic applications. Further research at higher radiation doses could provide deeper insights into its potential for radiation detection and its broader applicability in challenging environments.

Acknowledgment

This work was partially supported BAİBÜ Scientific Research Office with 2022.03.02.1535 and 2021.09.01.1521 projects. This study forms a part of the PhD thesis of Harem Saleh. Authors also would like to thank to Presidency of the Republic of Turkey Presidency of Strategy and Budget (Contract Number: 2016K12-2834).

Conflict of Interest

The authors declare that they have no conflict of interest.

References

Baydogan, N., Ozdemir, O., & Cimenoglu, H. (2013). The improvement in the electrical properties of nanospherical ZnO: Al thin film exposed to irradiation using a Co-60 radioisotope. *Radiation Physics and Chemistry*, *89*, 20-27. https://doi.org/10.1016/j.radphyschem.2013.02.042

Bera, M. K., & Maiti, C. K. (2007). Charge trapping properties of ultra-thin TiO_2 films on strained-Si. *Semiconductor Science and Technology*, *22*(7), 774-783. https://doi.org/10.1088/0268-1242/22/7/017

Doyle, B. L. (2014). *Displacement damage caused by gamma-rays and neutrons on Au and Se*. Sandia National Laboratories.

Hill, W. A., & Coleman, C. C. (1980). A single-frequency approximation for interface-state density determination. *Solid-State Electronics*, *23*(9), 987-993. https://doi.org/10.1016/0038-1101(80)90064-7

Jiang, N. (2015). Electron beam damage in oxides: A review. *Reports on Progress in Physics*, *79*(1), 016501. https://doi.org/10.1088/0034-4885/79/1/016501

Kahraman, A., & Yilmaz, E. (2018). A comprehensive study on usage of Gd_2O_3 dielectric in MOS based radiation sensors considering frequency dependent radiation response. *Radiation Physics and Chemistry*, *152*, 36-42. https://doi.org/10.1016/j.radphyschem.2018.07.017

Kaleji, B. K., Sarraf-Mamoory, R., & Fujishima, A. (2012). Influence of Nb dopant on the structural and optical properties of nanocrystalline TiO_2 thin films. *Materials Chemistry and Physics*, *132*(1), 210-215. https://doi.org/10.1016/j.matchemphys.2011.11.034

Karadeniz, S., Selcuk, A. B., Tuğluoğlu, N., & Ocak, S. B. (2007). On the interface trap density and series resistance of tin oxide film prepared on n-type Si (1 1 1) substrate: Frequency dependent effects before and after ^{60}Co γ-ray irradiation. *Nuclear Instruments and Methods in Physics Research Section B: Beam Interactions with Materials and Atoms*, *259*(2), 889-894. https://doi.org/10.1016/j.nimb.2007.02.085

Karataş, Ş., Türüt, A., & Altındal, Ş. (2009). Irradiation effects on the C–V and G/ω–V characteristics of Sn/p-Si (MS) structures. *Radiation Physics and Chemistry*, *78*(2), 130-134. https://doi.org/10.1016/j.radphyschem.2008.09.006

Kaya, S., & Yilmaz, E. (2015). A comprehensive study on the frequency-dependent electrical characteristics of Sm_2O_3 MOS capacitors. *IEEE Transactions on Electron Devices*, *62*(3), 980-987. https://doi.org/10.1109/TED.2015.2389953

Kaya, Ş., Yılmaz, E., & Çetinkaya, A. (2015a). Influences of irradiation on the C–V and G/ω–V characteristics of Si_3N_4 MIS capacitors. *Journal of Nuclear Sciences*, *2*(2), 48-52. https://doi.org/10.1501/nuclear_0000000012

Kaya, S., Yilmaz, E., Kahraman, A., & Karacali, H. (2015b). Frequency dependent gamma-ray irradiation response of Sm_2O_3 MOS capacitors. *Nuclear Instruments and Methods in Physics Research Section B: Beam Interactions with Materials and Atoms*, *358*, 188-193. https://doi.org/10.1016/j.nimb.2015.06.037

Kaya, S., & Yilmaz, E. (2018). Modifications of structural, chemical, and electrical characteristics of Er_2O_3/Si interface under Co-60 gamma irradiation. *Nuclear Instruments and Methods in Physics Research Section B: Beam Interactions with Materials and Atoms*, *418*, 74-79. https://doi.org/10.1016/j.nimb.2018.01.010

Kaya, S., Yıldız, I., Lok, R., & Yılmaz, E. (2018). Co-60 gamma irradiation influences on physical, chemical and electrical characteristics of HfO_2/Si thin films. *Radiation Physics and Chemistry*, *150*, 64-70. https://doi.org/10.1016/j.radphyschem.2018.04.023

Kaya, S., Abubakar, S., & Yilmaz, E. (2019). Co-60 gamma irradiation influences on device characteristics of n-SnO_2/p-Si heterojunction diodes. *Nuclear Instruments and Methods in Physics Research Section B: Beam Interactions with Materials and Atoms*, *445*, 63-68. https://doi.org/10.1016/j.nimb.2019.03.013

Kozlovskiy, A. L., Abyshev, B., Shlimas, D. I., & Zdorovets, M. V. (2022). Study of structural, strength, and thermophysical properties of $Li_{2+4x}Zr_{4-x}O_3$ ceramics. *Technologies*, *10*(3), 58. https://doi.org/10.3390/technologies10030058

Laha, P., Dahiwale, S. S., Banerjee, I., Pabi, S. K., Kimd, D., Barhai, P. K., Bhoraskar, V. N., & Mahapatra, S. K. (2011). 6 MeV electron irradiation effects on electrical properties of Al/TiO_2/n-Si MOS capacitors. *Nuclear Instruments and Methods in Physics Research Section B: Beam Interactions with Materials and Atoms*, *269*(23), 2740-2744. https://doi.org/10.1016/j.nimb.2011.08.024

Laha, P., Banerjee, I., Barhai, P. K., Das, A. K., Bhoraskar, V. N., & Mahapatra, S. K. (2012). Effects of 6 MeV electron irradiation on the electrical properties and device parameters of Al/Al_2O_3/TiO_2/n-Si MOS capacitors. *Nuclear Instruments and Methods in Physics Research Section B: Beam Interactions with Materials and Atoms*, *283*, 9-14. https://doi.org/10.1016/j.nimb.2012.04.014

Li, S., Luo, J., & Ye, T. (2023). Investigation of reducing interface state density in 4H-SiC by increasing oxidation rate. *Nanomaterials*, *13*(9), 1568. https://doi.org/10.3390/nano13091568

Liu, Y., Zhu, Y., Shen, T., Chai, J., Niu, L., Li, S., Jin, P., Zheng, H., & Wang, Z. (2021). Irradiation response of Al_2O_3-ZrO_2 ceramic composite under He ion irradiation. *Journal of the European Ceramic Society*, *41*(4), 2883-2891. https://doi.org/10.1016/j.jeurceramsoc.2020.11.042

Ma, T. P., & Dressendorfer, P. V. (1989). *Ionizing radiation effects in MOS devices and circuits*. John Willey & Sons.

Manikanthababu, N., Arun, N., Dhanunjaya, M., Saikiran, V., Nageswara Rao, S. V. S., & Pathak, A. P. (2015). Synthesis characterization and radiation damage studies of high-k dielectric (HfO_2) films for MOS device applications. *Radiation Effects & Defects in Solids*, *170*(3), 207-217. https://doi.org/10.1080/10420150.2014.980259

Mazzolini, P., Russo, V., Casari, C. S., Hitosugi, T., Nakao, S., Hasegawa, T., & Li Bassi, A. (2016). Vibrational–electrical properties relationship in donor-doped TiO_2 by Raman spectroscopy. *The Journal of Physical Chemistry C*, *120*(33), 18878-18886. https://doi.org/10.1021/acs.jpcc.6b05282

Mozia, S. (2008). Effect of calcination temperature on photocatalytic activity of TiO_2. Photodecomposition of mono-and polyazo dyes in water. *Polish Journal of Chemical Technology*, *10*(3), 42-49. https://doi.org/10.2478/v10026-008-0035-1

Mozia, S., Morawski, A. W., Toyoda, M., & Inagaki, M. (2009). Application of anatase-phase TiO_2 for decomposition of azo dye in a photocatalytic membrane reactor. *Desalination*, *241*(1-3), 97-105. https://doi.org/10.1016/j.desal.2007.12.048

Shi, H. L., Zou, B., Li, Z. A., Luo, M. T., & Wang, W. Z. (2019). Direct observation of oxygen-vacancy formation and structural changes in Bi_2WO_6 nanoflakes induced by electron irradiation. *Beilstein Journal of Nanotechnology*, *10*(1), 1434-1442. https://doi.org/10.3762/bjnano.10.141

Subramanian, A., & Wang, H. W. (2012). Effect of hydroxyl group attachment on TiO_2 films for dye-sensitized solar cells. *Applied Surface Science*, *258*(20), 7833-7838. https://doi.org/10.1016/j.apsusc.2012.04.069

Tracy, C. L., Pray, J. M., Lang, M., Popov, D., Park, C., Trautmann, C., & Ewing, R. C. (2014). Defect accumulation in ThO_2 irradiated with swift heavy ions. *Nuclear Instruments and Methods in Physics Research Section B: Beam Interactions with Materials and Atoms*, *326*, 169-173. https://doi.org/10.1016/j.nimb.2013.08.070

Wilk, G. D., Wallace, R. M., & Anthony, J. (2001). High-κ gate dielectrics: Current status and materials properties considerations. *Journal of Applied Physics*, *89*(10), 5243-5275. https://doi.org/10.1063/1.1361065

Yilmaz, E., Doğan, İ., & Turan, R. (2008). Use of Al_2O_3 layer as a dielectric in MOS based radiation sensors fabricated on a Si substrate. *Nuclear Instruments and Methods in Physics Research Section B: Beam Interactions with Materials and Atoms*, *266*(22), 4896-4898. https://doi.org/10.1016/j.nimb.2008.07.028

Zhang, H., Su, R., Szlufarska, I., Shi, L., & Wen, H. (2021). Helium effects and bubbles formation in irradiated Ti_3SiC_2. *Journal of the European Ceramic Society*, *41*(1), 252-258. https://doi.org/10.1016/j.jeurceramsoc.2020.08.015

Zhou, X. J., Fleetwood, D. M., Felix, J. A., Gusev, E. P., & D'Emic, C. (2005). Bias-temperature instabilities and radiation effects in MOS devices. *IEEE Transactions on Nuclear Science*, *52*(6), 2231-2238. https://doi.org/10.1109/TNS.2005.860667

http://jaasci.com
JOURNAL OF ADVANCED APPLIED SCIENCES
e-ISSN: 2979-9759
https://prensip.gen.tr

SHORT COMMUNICATION

Behaviour of 32 CrMoV12-10 Steel Towards Boronizing Variables

Sadettin Sahin

Kırıkkale University, Faculty of Engineering and Natural Sciences, Department of Metallurgical and Materials Engineering, Kırıkkale/Türkiye

ARTICLE INFO

Article History
Received: 29.11.2024
Accepted: 17.12.2024
First Published: 30.12.2024

Keywords
32 CrMoV12-10
Barrel steel
Boriding agent
Boriding
Boron compounds
Gun tube

ABSTRACT

During the shooting in gun barrels; there are many forces that affect each other such as external swelling caused by the explosion, excessive wear caused by the bullet core rubbing inside the barrel, high temperature caused by friction and gunpowder temperature, thermal expansion caused by temperature, chemical corrosion caused by gunpowder gases. It is expected that the barrel steel will show optimum resistance against all these effects. The most harmful of these is the wear force. The barrel, whose inner diameter expands due to wear, becomes unusable after a certain number of shots. In order to increase the effective number of shots, different hardening applications are made to the inner surfaces of the barrels of very different steel qualities. One of the commonly used barrel steels is 32CrMoV12-10 steel and hard chrome plating of the inner surface of the barrel. In this study, the boronizing behavior of 32CrMoV12-10 steel was investigated as an alternative coating technique. The changes in the type, layer thickness and hardness values of boron compounds formed on the surface as a function of temperature and time were investigated. Boriding processes were carried out with a holding time of 2, 4 and 6 hours by setting the boriding temperature to 900°C. Typical columnar structures were observed at depths of 73, 100 and 133 µm in SEM microscope images. XRD (X-Ray Diffraction) analysis revealed that these were FeB, Fe_2B, MnB and CrB compounds and that boride depth and hardness increased as the holding time increased. In microhardness tests conducted in this area, hardness values up to 2500 HV were obtained.

Please cite this paper as follows:

Sahin, S. (2024). Behaviour of 32 CrMoV12-10 steel towards boronizing variables. *Journal of Advanced Applied Sciences*, *3*(2), 85-90. https://doi.org/10.61326/jaasci.v3i2.316

1. Introduction

32CrMoV12-10, a type of alloyed carbon steel is used to manufacture automotive parts and gun tubes that require a high level of toughness and strength. Its original hardness value is not very high. High wear resistance is essential to extend ballistic gun barrel life. It was aimed to form hard boron compounds on the 32CrMoV12-10 steel surface. In current industrial practice, hard chromium coating is applied to the inner surface of gun tubes with the aim of extending their life. This is a very slow process that poses risks to the environment and occupational health due to the use of toxic chemicals. The term “surface boriding treatment” refers to the process of using thermochemical processes to create hard boron compounds on the steel surface in the form of a thin layer.

There are pack boriding studies concerning different types of steel. Zong et al. (2018) have detected FeB, Fe_2B and CrB compounds at 9.3-97.2 µm thickness on the surface of AISI 440C martensitic steel as a result of pack boriding. The hardness values taken from this surface measured between 393 and 1730-2080 $HV_{0.05}$. Campos-Silva et al. (2010) investigated the formation and kinetics of the FeB/Fe_2B layers on the surface of AISI 316 borided steel. Experiments were carried out at a temperature of 1000°C and holding times of 3 and 5 hours. An optimum 50-250 µm thick borided layer is formed in low-

Correspondence
E-mail address: ssahin@kku.edu.tr

carbon and low-alloy steels, while the boride layer thickness range in high-alloyed steels was measured between 25-76 μm.

Kayali (2013) treated AISI 420, AISI 304 and AISI 304L stainless steel surfaces with Ekabor-II powder at temperatures of 850, 900 and 1000ºC for 2, 4 and 6 hours. 4.6-64 μm thick FeB, Fe_2B, CrB and NiB formations were detected on the surface. In their study titled "Low temperature boriding of high carbon steel", He et al. (2015) stated that two boride phases (FeB and Fe_2B) coexist in the borided layer at 780ºC. In his study, Taktak (2006) detected FeB, Fe_2B and CrB in the boronized layer as a result of the boronizing process applied to AISI H13 (X40CrMoV 5-1) steel at temperatures of 1073-1223 K for 5 hours and measured the hardness value as 1860 HV. Keddam et al. (2018) detected FeB, Fe_2B, CrB and Cr_2B in the boronized layer as a result of the boronizing process performed on AISI 440 C (X105CrMo17) steel at different temperatures and waiting times. Zuno-Silva et al. (2018) detected FeB-Fe_2B-CrB-Cr_2B-Ni_3B on the surface of AISI S1 (60WCrV 8) steel on which they applied boronizing process at 800-1050ºC.

Literatures reveal that after the boriding process, Fe-B compounds are formed on the steel surface and Cr, Ni, Mn-B compounds are formed on the boride layer depending on the alloying elements contained in the steel.

It is a common method to extend the wear and corrosion life of machine parts by coating the surface of a cheap material with an effective surface coating technique instead of using expensive materials. The process of boriding is a type of thermochemical diffusion process in which very high hardness values are able to be obtained (Keddam et al., 2017). It can be applied to steel, superalloys, non-ferrous metals and alloys (Anthymidis et al., 2002; Gencer, 2011; Litoria et al., 2020; Sista et al., 2015).

In order to obtain iron boron compounds, the boriding temperature applied to steel alloys ranges between 800 and 1000ºC. Although there are solid, liquid and gas boriding techniques, the most preferred method is pack boriding (Kulka, 2019).

It is a process that is similar in technique to pack carburizing. As a boron source, B_4C and its activator are usually found together in a box. B_4C and an activator are placed together with the part in a sealed box and kept in a furnace at a specified temperature and time. The box is removed from the oven and is left to cool.

2. Materials and Methods

In this study, 32CrMoV12-10 steel was used as the material to be coated. The chemical composition of the steel, and its mechanical properties are given in Table 1 and Table 2 respectively. It is widely preferred in the manufacture of gun barrels due to its high toughness along with its high strength value.

It has also a high carburizing and nitriding ability due to the alloying elements. The test pieces were machined on a cylindrical lathe with a diameter of 10 mm and a length of 20 mm. Prior to boronizing, the original hardness value of the steel measured at 300 HV.

Table 1. Chemical composition of 32CrMoV 12 10 steel.

	C	Cr	Mo	V	Si	Mn	Ni	P	S
Min	0.29	2.80	0.7	0.15	0.10	0.40	--	--	--
Max	0.36	3.30	1.2	0.35	0.40	0.70	0.30	0.001	0.001

Table 2. Mechanical properties of 32CrMoV 12 10 steel.

Yield Strength (MPa)	Tensile Strenght (MPa)	Hardness (HV)
800	940	300

2.1. Boronizing Method

Baybora-1 (Bayça, 2018) was used as a new boronizing agent in this study. Baybora-1 a new patented boronizing agent was used instead of EKABOR which is widely used as a boronizing agent. It contains boron compounds, activator and deoxidizer. The boriding process was carried out in a stainless-steel box fitted with a lid. To begin, the box was half-filled with Baybora-1 powder before placing samples in this powder. The other half of the box was then filled with deoxidant material and the lid of the box was securely closed. The box was placed in an electric chamber furnace and heated at 900ºC for 2, 4, and 6 hours. The samples were named as N2, N4 and N6 according to their waiting times in hour.

At the end of this period, the furnace was turned off and the sample was left in the furnace to cool. Cylindrical specimens, both original and boronized, were cut vertically and starting from 600 mesh, it was gradually ground with 1200 μm sandpaper. Nital solution was prepared using 4% nitric acid and 96% ethyl alcohol. The ground samples were immersed in the 4% nital solution and etched. The ethyl alcohol and nitric acid used were of analytical grade. SEM images of the etched samples were obtained. Vicker hardness was measured inward from the sample surface using a 100 g load and 20 μm spacing. After surface cleaning, XRD analysis was performed on the non-boronized and boronized samples.

The 2608 HV value obtained in the hardness measurements was evaluated as the success of the boronizing agent used, as it is the highest value seen in the literature.

3. Results and Discussion

As shown in Figure 1, the XRD diffraction peaks of N2, N4, and N6 were evaluated to determine the phase types. The formation of different phases on the boride layer can be used to define the hardness and mechanical properties of that layer. It was observed that the dual phase i.e., FeB and Fe_2B were formed on the boride layer rather than a single phase at $2\theta = 82^o$. In addition, the chromium boride (CrB) phase was observed with FeB and Fe_2B at $2\theta = 45^o$. Other elements of 32CrMoV12-10 steel, such as V and Mo, are generally known for forming solid solution phases with carbon. The diffraction peak that appeared at $2\theta = 65^o$ is imputed to the $Cr_{23}C_6$ phase.

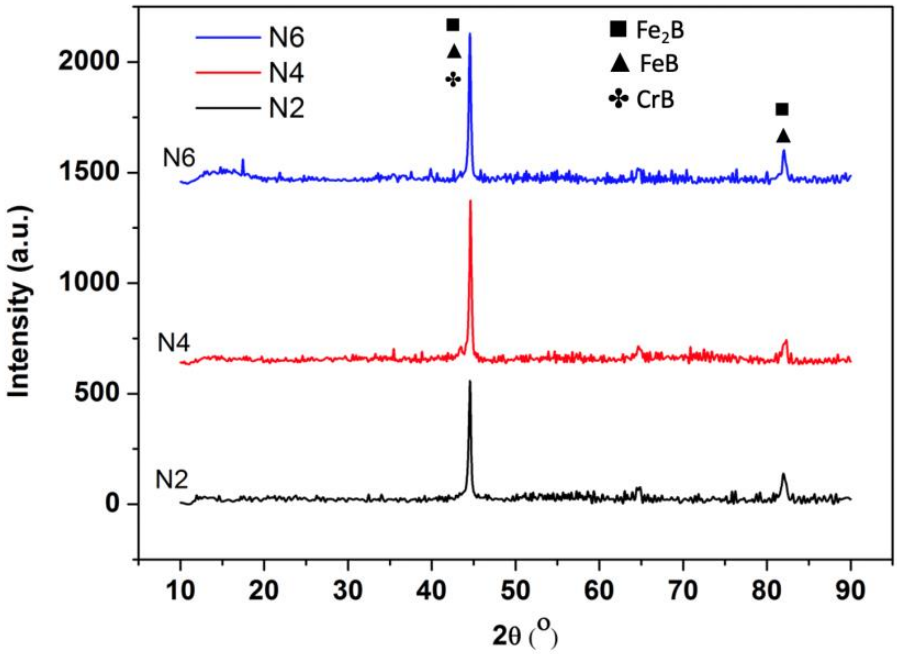

Figure 1. XRD result of N2, N4, and N6.

The microstructures of the boride layers on the surface of 32CrMoV12-10 steels were given for different times denoted as N2, N4, and N6. It was observed that the Cr monolayer formed on the surface of the boronized layers at a thickness of approximately 5 μm for N2, N4, and N6. The morphology of B_4C was observed as a columnar structure with 100 μm, 74 μm, and 133 μm thicknesses for N2, N4, and N6, respectively. The N6 sample that was boronized at 900°C for 6 hours demonstrated greater effectiveness on increasing the thicknesses of the boride layer. The types of formation phase i.e a single phase (Fe_2B) or dual phase (FeB and Fe_2B) is dependent on the temperature, time and chemical composition of the samples (Han et al., 2019; Salloom et al., 2020). Raghs et al. (2020) obtained both FeB and Fe_2B phases at temperatures 800°C and 900°C. Different types of boride phases such as Cr, Ni, V-B can be formed during the boriding process depending on the chemical composition of the 32CrMoV12-10 steel. The transition zone that which consists of the Fe_2B phase was clearly observed in each of the processing times. Figure 2 illustrates a typical borided structure on steel surface.

The EDX analysis of N6 is illustrated in Figure 3. Area 1 represents the boron-coated side and is selected by the base metal point 2. While no B signal is observed in Area 2, it can be seen that the composition of Area 1 contains B element at a concentration of 3.3% by weight. This result also established the presence of B in the coated area. EDX analyses of the areas are given on Table 3.

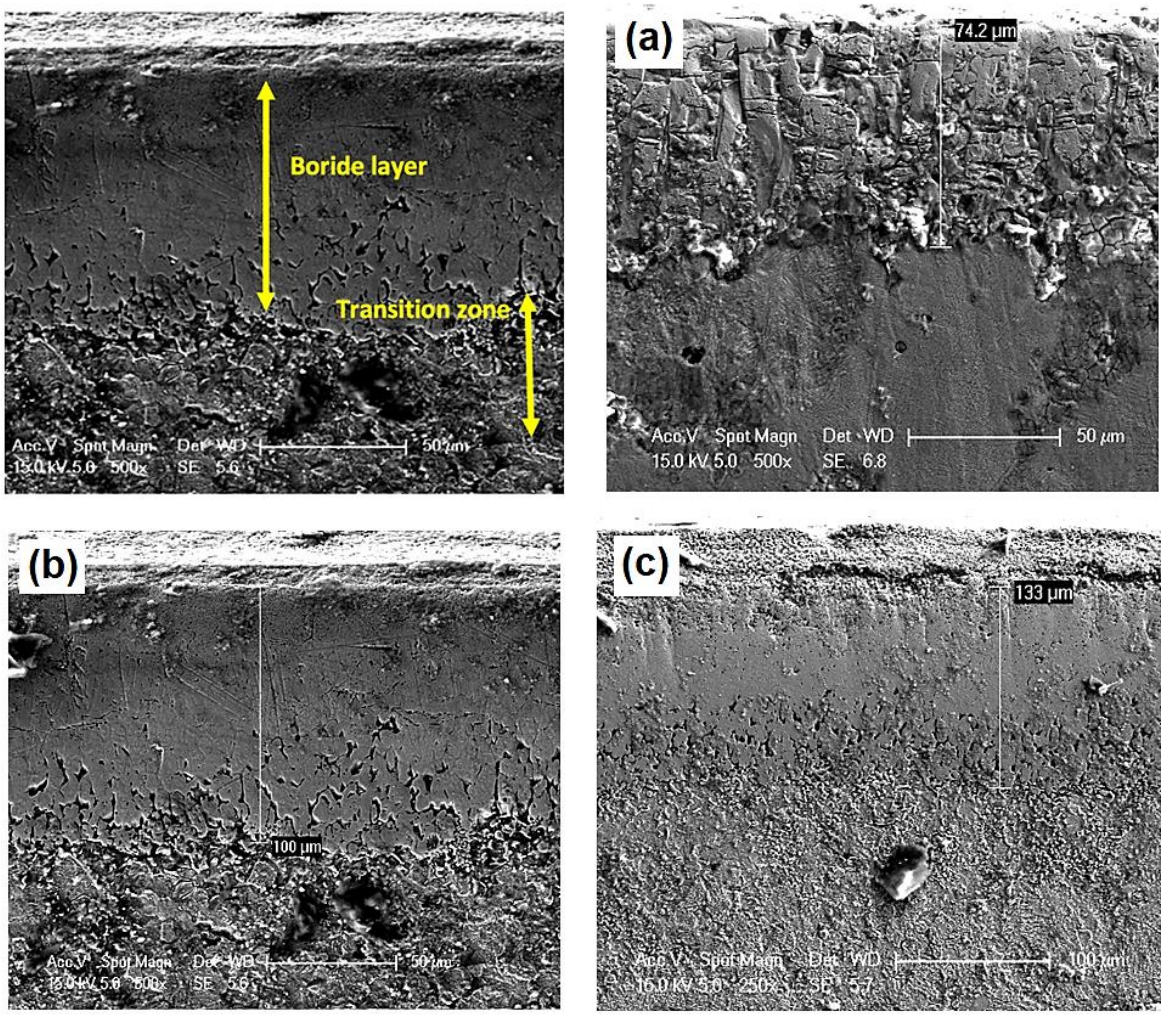

Figure 2. The SEM images of typical boride layers and (a) N2, (b) N4, and (c) N6.

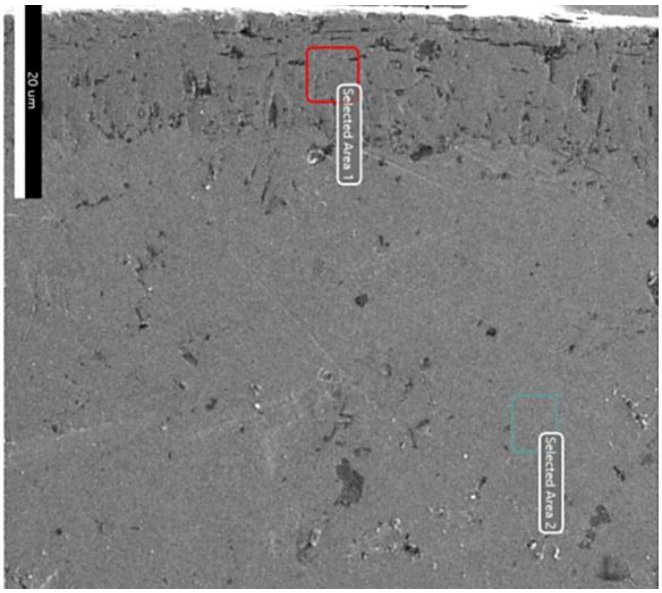

Figure 3. EDX analysis of N6 sample.

Table 3. EDX analyses of areas.

Elements	Area 1	Area 2
B	3.3	0
C	0.8	0.739
Al	0.85	1.02
Si	0.42	0.47
Mn	3.35	4.45
Mo	0.7	1.02
Fe	Remain	Remain

The surface hardness values of N2, N4, and N6 are displayed in Figure 4. The surface hardness values of the boronized layer were measured as 2200 HV, 2608 HV, and 1743 HV for N2, N4 and N6, respectively. The formation of hard FeB and Fe_2B phases resulted in a significant increase in hardness from bulk to boronized layer. N4 provided the layer with the highest hardness value. Due to the formation of the FeB phase in the boronized layer, the measured surface hardness of N4 increased by approximately 88% percent when compared to the bulk hardness. According to previous research, increasing the boronizing process time results in the increase in

the formation of the Fe_2B phase, which has a lower hardness than the FeB phase (Campos-Silva et al., 2010; He et al., 2015; Zong et al., 2018). The decrease in N6's surface hardness can be attributed to the formation of the Fe_2B phase.

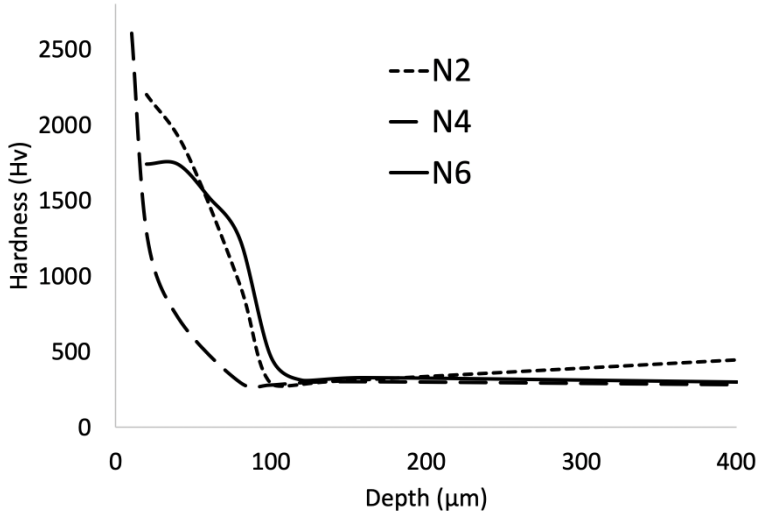

Figure 4. The surface hardness values of N2, N4, and N6.

4. Conclusion

In this study, the 32CrMoV12-10 steel was boronized and its coated layer morphology and hardness properties were investigated. The boronized layer was observed clearly in the SEM image and the presence of boron compounds were established through EDX characterization. The results indicate that as excess holding time increased, thickness of the borided layer increased but the hardness values of samples decreased because of Fe_2B formation on the surface. Baybora 1, a new and different boronizing agent, gave very good boronizing results.

Conflict of Interest

The author has no conflict of interest to declare.

References

Anthymidis, K. G., Stergioudis, G., Roussos, D., Zinoviadis, P., & Tsipas, D. N. (2002). Boriding of ferrous and non-ferrous metals and alloys in fluidised bed reactor. *Surface Engineering*, *18*(4), 255-259. https://doi.org/10.1179/026708401225005296

Bayça, S. U. (2018). *A solid boriding agent* (Patent no: PCT/TR2018/050643). Turkish Patent and Trademark Office.

Campos-Silva, I., Ortiz-Domínguez, M., Bravo-Bárcenas, O., Doñu-Ruiz, M. A., Bravo-Bárcenas, D., Tapia-Quintero, C., & Jiménez-Reyes, M. Y. (2010). Formation and kinetics of FeB/Fe2B layers and diffusion zone at the surface of AISI 316 borided steels. *Surface & Coatings Tehnology*, *205*(2), 403-412. https://doi.org/10.1016/j.surfcoat.2010.06.068

Gencer, Y. (2011). Influence of manganese on pack boriding behaviour of pure iron. *Surface Engineering*, *27*(8), 634-638. https://doi.org/10.1179/1743294411Y.0000000010

Han, T., Xiao, M., Zhang, Y., & Shen, Y. (2019). Laser cladding composite coatings by Ni–Cr–Ti–B4C with different process parameters. *Materials and Manufacturing Processes*, *34*(8), 898-906. https://doi.org/10.1080/10426914.2019.1605172

He, X., Xiao, H., Ozaydin, M. F., Balzuweit, K., & Liang, H. (2015). Low temperature boriding of high carbon steel. *Surface &Coatings Technology*, *263*, 21-26. https://doi.org/10.1016/j.surfcoat.2014.12.071

Kayali, Y. (2013). Investigation of the diffusion kinetics of borided stainless steels. *The Physics of Metals and Metallography*, *114*, 1061-1068. https://doi.org/10.1134/S0031918X1322002X

Keddam, M., Chegroune, R., Kulka, M., Panfil, D., Ulker, S., & Taktak, S. (2017). Characterization and diffusion kinetics of the plasma paste borided AISI 440C steel. *Transactions of the Indian Institute of Metals*, *70*, 1377-1385. https://doi.org/10.1007/s12666-016-0934-4

Keddam, M., Ortiz-Dominguez, M., Elias-Espinosa, M., Arenas-Flores, A., Zuno-Silva, J., Zamarripa-Zepeda, D., & Gomez-Vargas, O. A. (2018). Kinetic investigation and wear properties of Fe_2B layers on AISI 12L14 steel. *Metallurgical and Materials Transactions A*, *49*, 1895-1907. https://doi.org/10.1007/s11661-018-4535-1

Kulka, M. (2019). *Current trends in boriding: Techniques*. Springer. https://doi.org/10.1007/978-3-030-06782-3

Litoria, A. K., Figueroa, C. A., Bim, L. T., Pruncu, C. I., Joshi, A. A., & Hosmani, S. S. (2020). Pack-boriding of low alloy steel: Microstructure evolution and migration

behaviour of alloying elements. *Philosophical Magazine Part A: Materials Science*, *100*(3), 353-378. https://doi.org/10.1080/14786435.2019.1680890

Raghs, H. A., Kondul, B., & Cetin, M. H. (2020). Investigation of wear behavior of boronized H13 steel under environment of nano-silver-added lubricants coated with different ligands. *Surface Topography: Metrology and Properties*, *8*, 015007. https://doi.org/10.1088/2051-672X/ab6ece

Salloom, R., Joshi, S. S., Dahotre, N. B., & Srinivasan, S. G. (2020). Laser surface engineering of B4C/Fe nano composite coating on low carbon steel: Experimental coupled with computational approach. *Materials & Design*, *190*, 108576. https://doi.org/10.1016/j.matdes.2020.108576

Sista, V., Kahvecioglu, O., Kartal, G., Zeng, Q. Z., Kim, J. H., Eryilmaz, O. L., & Erdemir, A. (2015). Evaluation of electrochemical boriding of Inconel 600. *Surface and Coatings Technology*, *215*, 452-459. https://doi.org/10.1016/j.surfcoat.2012.08.083

Taktak, S. (2006). A study on the diffusion kinetics of borides on boronized Cr- based steels. *Journal of Materials Science*, *41*, 7590-7596. https://doi.org/10.1007/s10853-006-0847-4

Zong, X., Jiang, W., & Fan, Z. (2018). Characteristis and wear performance of borided AISI 440C martensitic steel. *Materials Express*, *8*(6), 500-510. https://doi.org/10.1166/mex.2018.1463

Zuno-Silva, J., Keddam, M., Ortiz-Domínguez, M., Carlos Elias-Espinosac, M., Cervantes-Sodi, F., Oseguera-Peña, J., Fernández De- Dios, L. D., & Gomez-Vargas, O. A. (2018). Kinetics of formation of Fe_2B layers on AISI S1 steel. *Materials Research*, *21*(5), e20180173. https://doi.org/10.1590/1980-5373-MR-2018-0173

AIMS & SCOPE

Journal of Advanced Applied Sciences aims to publish relevant articles that focus on modern applications of Physics, Electrical and Electronics Engineering, Computer Science and Information Engineering and Material Science. We are particularly interested in applied research that makes significant scientific contributions across the broad spectrum of applied sciences.

The **Physics and Materials section** of the *Journal of Advanced Applied Sciences* targets the latest development in the Applied Physics area and its intersection with the Material Science. Some keywords that we are considering are: Electronic, Optical, Mechanical Magnetic and Structural properties of materials. Especially, Structure-Property relationship and characterization, Superconductivity, Cryogenics, Semiconductivity, Spintronics, Organic electronics, Perovskite/Silicon solar cells, Biomaterials and health applications, Bioelectronics and sensors, Photonic materials, Thermoelectric materials, Nanomaterials/nanoparticles, Energy transfer storage and conversion, Organic materials doping, Batteries, Alloys and ceramics, Applied biophysics and other topics related to applied sciences are of our interest.

The **Engineering section** deals with studies in various sub-disciplines of electrical and electronics and computer engineering technology such as Applied Engineering, Robotics and Control, Signal Processing, Data Analysis, Computational Systems, Communication Systems, Machine Learning, Artificial Intelligence and Deep Learning, Image Processing and Signal Processing, Big Data, Energy, Power and Industrial Applications, Systems security and data encryption, Microwaves and optics.

AUTHOR GUIDELINES

Manuscripts must be submitted to the journal in electronic version through online submission system at https://prensipjournals.com/ojs/index.php/jaasci/author-guidelines following the Author Guidelines of the journal.

Types of Paper

Research articles, review articles, short communications, and letters to the Editor.

- Research articles: original full-length research papers which have not been published previously and should not exceed 7500 words or 25 manuscript pages (including tables and figures).
- Review articles: on topical subjects and up to 10000 words or 25 manuscript pages (including tables and figures).
- Short communications: describing work that may be of a preliminary nature or a case report; preferably no more than 3000 words or 10 manuscript pages (including tables and figures).
- Letters to the Editor: should be included on matters of topical interest and not exceeding 2000 words or 10 manuscript pages (including tables and figures).

Page Charges

This journal has no page charges.

Preparation of Manuscripts

Papers must be written in English. Prepare your text using a word-processing software and save in ".doc" or ".docx" formats. Manuscripts must be structured in the following order:

- ***Title Page File***
  - Title (Concise and informative. Avoid abbreviations and formulae)
  - Author names and affiliation addresses (Full names should be given, no abbreviations. The corresponding author should be identified with an asterisk. Each affiliation address should include institution, faculty/school, department, city, and country)
  - ORCID numbers for all authors.
  - Corresponding author's e-mail, telephone number, and address
  - Acknowledgements (if applicable. Keep these to the absolute minimum)
  - Compliance with Ethical Standards
    - Conflict of Interest Statement
    - Statement on the Welfare of Animals (if applicable)
    - Statement of Human Rights (if applicable)
- ***Main File***
  - Title
  - Abstract (Should be between 100 and 350 words. References and abbreviations should be avoided)
  - Keywords (Minimum 3, Maximum 6 keywords)
  - Introduction
  - Materials and Methods
  - Results
  - Discussion (Can be combined with Results section if appropriate)
  - Conclusion
  - References
  - Table(s) with caption(s) (on appropriate location in the text)
  - Figure(s) with caption(s) (on appropriate location in the text)
  - and appendices (if any)

Manuscript Formatting

Use a 12-point Times New Roman font, including the references, table headings and figure captions, double-spaced and with 25 mm margins on all sides of A4 size paper throughout the manuscript. The text should be in single-column format.

- Each page must be numbered with Arabic numerals, and lines must be continuously numbered from the start to the end of the manuscript.
- Use italics for emphasis.
- Use only SI (international system) units.

• Use "dot" for decimal points.

References

Journal of Advanced Applied Sciences uses APA style (7th edition). Accordingly, authors must format their references as per the guidelines below. Please ensure that each reference cited in the text is also presented in the reference list. Authors should always supply DOI or URL of the work cited if available.

In-text citation (Narrative):

…The results of Bliss (2022) support…
…Sönmez and Taştan (2020) indicated that…
…According to the method of Öztürk et al. (2021)…

In-text citation (In parenthesis):

…It was found to be isometric (Öztürk, 2018)…
…is highly susceptible to friction (Doma & Craig, 2019)…
…have been studied (Kale et al., 2020)…

Two or more works in the same parenthesis:

…crushes under high pressure (Sönmez, 2018, 2019; Öztürk et al., 2020a; Kadak & Taştan, 2021)…

Citation in the reference list:

References should be listed first alphabetically and then further sorted chronologically at the end of the article. The citation of all references should conform to the following examples:

Article:

Lastname, N., Lastname, M., & Lastname, O. (Year). Title of the work. *Title of the Journal*, *Volume*(Issue), Page numbers. DOI

Tort, S. (1998). Stress and immune modulation in fish. *Developmental & Comparative Immunology*, *35*(12), 1366-1375. https://doi.org/10.1016/j.dci.2011.07.002

Kasumyan, A. O., & Døving, K. B. (2003). Taste preferences in fishes. *Fish and Fisheries*, *4*(4), 289-347. https://doi.org/10.1046/j.1467-2979.2003.00121.x

Özçelik, H., Taştan, Y., Terzi, E., & Sönmez, A. Y. (2020). Use of onion (*Allium cepa*) and garlic (*Allium sativum*) wastes for the prevention of fungal disease (*Saprolegnia parasitica*) on eggs of rainbow trout (*Oncorhynchus mykiss*). *Journal of Fish Diseases*, *43*(10), 1325-1330. https://doi.org/10.1111/jfd.13229

Article by DOI (early access):

Salem, M. O. A., Salem, T. A., Yürüten Özdemir, K., Sönmez, A. Y., Bilen, S., & Güney, K. (2021). Antioxidant enzyme activities and immune responses in rainbow trout (*Onchorhynchus mykiss*) juveniles fed diets supplemented with dandelion (*Taraxacum officinalis*) and lichen (*Usnea barbata*) extracts. *Fish Physiology and Biochemistry*. https://doi.org/10.1007/s10695-021-00962-5

Book:

Lastname, N., Lastname, M., & Lastname, O. (Year). *Title of the work*. Publisher.

Oidtmann, K., Xao, Q., & Lloyd, A. S. (2018). *The food need by the year 2050*. Elsevier.

Book Chapter:

Lastname, N., Lastname, M., & Lastname, O. (Year). Title of the chapter. In N. N. Lastname, A. Lastname & B. Lastname (Eds.), *Title of the book* (pp. Page numbers). Publisher.

Pickering, A. D. (1993). Growth and stress in fish production. In G. A. E. Gall & H. Chen (Eds.), *Genetics in Aquaculture* (pp. 51-63). Elsevier. https://doi.org/10.1016/b978-0-444-81527-9.50010-5

Dissertation or Thesis:

Lastname, N. (Year). *Title of dissertation/thesis* (Doctoral dissertation/Master's thesis, Name of Institution).

Sönmez, A. Y. (2011). *Karasu ırmağında ağır metal kirliliğinin belirlenmesi ve bulanık mantıkla değerlendirilmesi* (Doctoral dissertation, Atatürk University).

Taştan, Y. (2018). *Tatlısu kerevitindeki (Astacus leptodactylus) siyah solungaç hastalığı etkeni mantar Fusarium oxysporum'un PCR yöntemi ile teşhisi* (Master's thesis, Akdeniz University).

Conference Proceedings:

Lastname, N., Lastname, M., & Lastname, O. (Year). *Title of the work*. Title of the Conference. City.

Ken, A., & Kumar, S. (2020). *A new statistical model for fuzzy logic evaluation*. 3rd International Congress on Statistics. İstanbul.

Institution Publication:

Institution name. (Year). *Title of the work*. URL

FAO. (2020). *Fishery and aquaculture statistics 2018*. http://www.fao.org/3/cb1213t/CB1213T.pdf

Internet Source:

Lastname, N. (Year). *Title of the work*. Retrieved May 15, 2020, from URL

Perreault, L. (2019). *The future of agriculture: Polyculture*. Retrieved January 12, 2020, from https://www.agriculture.com

Table(s)

Tables, numbered in Arabic, should be in separate pages with a short descriptive title at the top. Place footnotes to tables below the table body and indicate them with superscript lowercase letters (or asterisks for significance values and other statistical data).

Figure(s)

All illustrations should be labelled as 'Figure' and numbered in consecutive Arabic numbers, Figure 1, Figure 2 etc. in the text. If panels of a figure are labelled (a, b, etc.) use the same case when referring to these panels in the text. Figures are recommended to be in electronic formats such as PNG, JPEG, TIFF (min.

300 dpi). All figures or tables should be presented in the body of the text.

Online Manuscript Submission
Authors are requested to submit manuscripts via the journal's online submission system at https://prensipjournals.com/ojs/index.php/jaasci/index

Submission Checklist
- Author Guidelines of the journal has been read and adhered

- **Title Page File**
  - Title
  - Full names, e-mails, and affiliation addresses of all authors
  - ORCID numbers of all authors
  - Corresponding author's e-mail, telephone number, and address
  - Ethical statements

- **Main File**
  - Continuous page numbers
  - Continuous line numbers
  - Blinded document (no personal information is present)
  - Title
  - Abstract (100-350 words)
  - Keywords (3-6 keywords)
  - All figures and tables are numbered and cited in order in text
  - Completeness and accuracy of the references have been checked
  - References have been edited as per the Journal guidelines

Publication Frequency
The journal includes original scientific articles on a variety of different subjects in English and is being published twice a year in June and December.

Publication Fees
Journal of Advanced Applied Sciences is an open access journal. No submission or publication charges are collected. All authors and readers have free access to all papers.

PUBLICATION ETHICS
Details about Publication Ethics can be found at https://prensipjournals.com/ojs/index.php/jaasci/policy

OPEN ACCESS POLICY
Details can be found at https://prensipjournals.com/ojs/index.php/jaasci/open-access

REVIEW PROCESS
Double-Blind Review and Evaluation Process
Double-Blind Review is a method applied for publishing scientific publications with the highest quality. This method forms the basis of an objective evaluation of scientific studies and is preferred by many scientific journals.

The views of referees have a decisive place in the publication quality of a Journal. *Journal of Advanced Applied Sciences* uses the double-blind review method, which means that both the reviewer and author identities are concealed from the reviewers, and vice versa, throughout the review process, in the evaluation process of all studies. For this reason, the authors are asked to blind their manuscripts before submitting. All the studies submitted to *Journal of Advanced Applied Sciences* are evaluated by double-blind review method according to the following steps.

1. Initial Evaluation Process
The studies submitted to *Journal of Advanced Applied Sciences* are first evaluated by the editor. At this stage, studies that are not in line with the aim and scope of the journal, are weak in terms of language and narrative rules in English, contain scientifically critical mistakes, are not original worthy, and cannot meet publication policies are rejected. Authors of rejected studies will be notified within one month at the latest from the date of submission. Eligible studies are sent to the field editor to which the study is relevant for pre-evaluation.

2. Pre-Evaluation Process
In the pre-evaluation process, the field editors examine the studies, introduction and literature, methods, findings, results, evaluation and discussion sections in detail in terms of journal publication policies, scope and authenticity of study. Study which is not suitable as a result of this examination is returned to the author with the field editor's evaluation report within four weeks at the latest. The studies which are suitable for the journal are passed to the referee process.

3. Referee Process
The studies are sent to the referees according to their content and the expertise of the referees. The field editor examining the study may propose at least two referees from the pool of *Journal of Advanced Applied Sciences* Advisory Board or referee pool according to their field of expertise or may propose a new referee appropriate to the field of study. The editors evaluate the referee's suggestions coming from the field editor and the studies are submitted to the referees. Referees are obliged to guarantee that they will not share any process or document about the study they are evaluating.

4. Referee Evaluation Process
The period given to the referee for the evaluation process is 15 days. Proposals for corrections from referees or editors must be completed by the authors within 1 month according to the "correction instruction". Referees can decide on the suitability of the study by reviewing the corrections and may also request multiple corrections if necessary.

Referee Reports

Referee evaluations are based in general on the originality of the studies, the method used, and the conformity with the ethical rules, the consistent presentation of the findings and results, and the examination of the literature.

This review is based on the following elements:

1. Introduction and Literature: The evaluation report contains the presentation and purpose of the problem addressed in the study, the importance of the topic, the scope of the relevant literature, the timeliness and the originality of the study.

2. Methodology: The evaluation report includes information on the suitability of the method used, the choice and characteristics of the research group, validity and reliability, as well as on the data collection and analysis process.

3. Findings: The evaluation report includes opinions on the presentation of the findings obtained in the frame of the method, the correctness of the analysis methods, the aims of the research and the consistency of the findings, the presentation of the required tables, figures and images and the conceptual evaluation of the tests used.

4. Evaluation and discussion: The evaluation report includes the opinion on the subject based on findings, relevance to research questions and hypotheses, generalizability and applicability.

5. Conclusion and suggestions: The evaluation report contains the opinion on the contributions to the literature, future studies and recommendations for the applications in the area.

6. Style and narration: The evaluation report includes compatibility of the title with the content, appropriate use of English in the study, refers and references in accordance with the language of the study and APA rules.

7. Overall evaluation: The evaluation report contains opinion on the authenticity of the study as a whole, its contribution to the educational literature and the applications in the area. The journal considers that scientists should avoid research which kills or damages any species of animal which, using IUCN criteria, is regarded as threatened or is listed as such in a Red Data Book appropriate for the geographic area concerned. In accordance with this view, papers based on such research will not be accepted by the Journal, unless the work had clear conservation objectives.

Plagiarism Detection

In agreement with publishing policies of *Journal of Advanced Applied Sciences*, plagiarism check is required for each study that has undergone the "Review Process". The Turnitin plagiarism checker software is used for plagiarism detection.

Proofs

Proof documents will be sent to the corresponding authors via e-mail. Proofs should be checked immediately and responses should be returned back within 15 working days. It is the responsibility of the authors to check carefully the proofs. No changes will be allowed after this stage.

DISCLAIMER

The Publisher and Editors cannot be held responsible for errors or any consequences arising from the use of information contained in this journal; the views and opinions expressed do not necessarily reflect those of the Publisher and Editors.

Editor or members of the editorial board are not responsible for the author's opinions and manuscript contents. Authors are responsible for the ethical originality of and possible errors in their manuscripts.

This journal is available online at http://jaasci.com/

Kindly visit website to search the articles and register for table of contents e-mail alerts.

LICENCE

INDEXING

Journal of Advanced Applied Sciences is currently indexed by

- Crossref
- Scilit
- Index Copernicus
- EuroPub
- Road
- Google Scholar

PUBLISHER

Prensip Publishing and Consultancy Ind. Trade. Co. Ltd.
Kuzeykent mah., Orgeneral Atilla Ateş Paşa Cad., No: 15CD,
İç Kapı No:31, Merkez/Kastamonu, 37150, TÜRKİYE
https://prensip.gen.tr
info@prensip.gen.tr

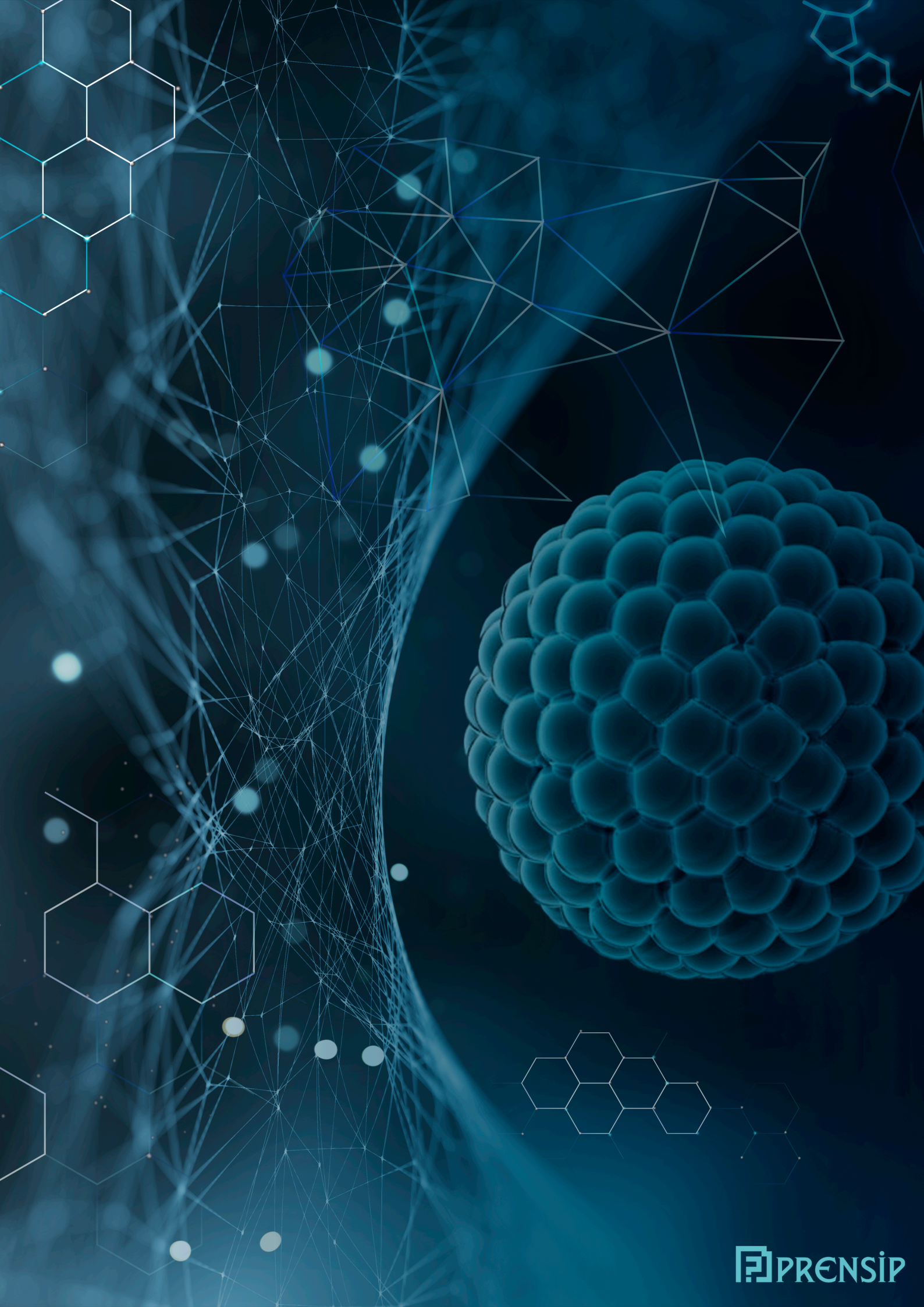
PRENSİP